Interplay between mineral reaction and deformation via structural defects

Kumulative Dissertation zur Erlangung des akademischen Grades eines „Doctor rerum naturalium“ (Dr. rer. nat.) in der Wissenschaftsdisziplin Geologie

Eingereicht an der Mathematisch-Naturwissenschaftlichen Fakultät der Universität Potsdam

von

Vanessa Helpa

Potsdam, den 28.10.2015

Gutachter:

Prof. Dr. Georg Dresen (GFZ Potsdam, Universität Potsdam)
Dr. Thomas Müller (Universität Leeds)
Prof. Dr. Timm John (Freie Universität Berlin)

Published online at the
Institutional Repository of the University of Potsdam:
URN urn:nbn:de:kobv:517-opus4-90332
http://nbn-resolving.de/urn:nbn:de:kobv:517-opus4-90332

Abstract

This thesis contains three experimental studies addressing the interplay between deformation and the mineral reaction between natural calcite and magnesite. The solid-solid mineral reaction between the two carbonates causes the formation of a magnesio-calcite precursor layer and a dolomite reaction rim in every experiment at isostatic annealing and deformation conditions.

CHAPTER 1 briefly introduces general aspects concerning mineral reactions in nature and diffusion pathways for mass transport. Moreover, results of previous laboratory studies on the influence of deformation on mineral reactions are summarized. In addition, the main goals of this study are pointed out.

In CHAPTER 2, the reaction between calcite and magnesite single crystals is examined at isostatic annealing conditions. Time series performed at a fixed temperature revealed a diffusion-controlled dolomite rim growth. Two microstructural domains could be identified characterized by palisade-shaped dolomite grains growing into the magnesite and granular dolomite growing towards calcite. A model was provided for the dolomite rim growth based on the counter-diffusion of CaO and MgO. All reaction products exhibited a characteristic crystallographic relationship with respect to the calcite reactant. Moreover, kinetic parameters of the mineral reaction were determined out of a temperature series at a fixed time. The main goal of the isostatic test series was to gain information about the microstructure evolution, kinetic parameters, chemical composition and texture development of the reaction products. The results were used as a reference to quantify the influence of deformation on the mineral reaction.

CHAPTER 3 deals with the influence of non-isostatic deformation on dolomite and magnesio-calcite layer production between calcite and magnesite single crystals. Deformation was achieved by triaxial compression and by torsion. Triaxial compression up to 38 MPa axial stress at a fixed time showed no significant influence of stress and strain on dolomite formation. Time series conducted at a fixed stress yield no change in growth rates for dolomite and magnesio-calcite at low strains. Slightly larger magnesio-calcite growth rates were observed at strains above >0.1. High strains at similar stresses were caused by the activation of additional glide systems in the calcite single crystal and more mobile dislocations in the magnesio-calcite grains, providing fast diffusion pathways. In torsion experiments a gradual de-

crease in dolomite and magnesio-calcite layer thickness was observed at a critical shear strain. During deformation, crystallographic orientations of reaction products rearranged with respect to the external framework. A direct effect of the mineral reaction on deformation could not be recognized due to the relatively small reaction product widths.

In CHAPTER 4, the influence of starting material microfabrics and the presence of water on the reaction kinetics was evaluated. In these experimental series polycrystalline material was in contact with single crystals or two polycrystalline materials were used as reactants. Isostatic annealing resulted in different dolomite and magnesio-calcite layer thicknesses, depending on starting material microfabrics. The reaction progress at the magnesite interface was faster with smaller magnesite grain size, because grain boundaries provided fast pathways for diffusion and multiple nucleation sites for dolomite formation. Deformation by triaxial compression and torsion yield lower dolomite rim thicknesses compared to annealed samples for the same time. This was caused by grain coarsening of polycrystalline magnesite during deformation. In contrast, magnesio-calcite layers tended to be larger during deformation, which triggered enhanced diffusion along grain boundaries. The presence of excess water had no significant influence on the reaction kinetics, at least if the reactants were single crystals.

In CHAPTER 5 general conclusions about the interplay between deformation and the mineral reaction in the carbonate system are presented.

Finally, CHAPTER 6 highlights possible future work in the carbonate system based on the results of this study.

Zusammenfassung

Die vorliegende Arbeit umfasst drei experimentelle Studien die sich mit der Wechselwirkung von Mineralreaktion und Deformation zwischen natürlichem Kalzit und Magnesit befassen. Die fest-fest Mineralreaktion zwischen den Karbonaten führt zur Entstehung einer Magnesio-Kalzit Vorläuferphase und zur Entstehung eines Dolomit Reaktionssaumes in allen durchgeführten Experimenten sowohl unter isostatischen Bedingungen als auch während der Deformation.

Im ersten Kapitel werden die grundlegenden Aspekte hinsichtlich Mineralreaktionen in der Natur und Diffusion angeführt. Weiterhin werden Resultate von vorherigen Studien bezüglich des Einflusses von Deformation auf Mineralreaktionen zusammengefasst. Außerdem werden die Hauptziele dieser Studie aufgezeigt.

Im zweiten Kapitel wird die Mineralreaktion zwischen Kalzit und Magnesit Einkristallen unter isostatischen Bedingungen untersucht. Zeitserien bei einer festgelegten Temperatur zeigten ein diffusionskontrolliertes Dolomitsaumwachstum. Die Mikrostruktur des Dolomitsaums ist durch zwei unterschiedliche Bereiche charakterisiert. Palisadenartige Dolomitkörner wachsen in den Magnesit und granulare Dolomitkörner wachsen in Richtung des Kalzits. Ein Model für das Dolomitsaumwachstum wurde angewandt, basierend auf der Gegendiffusion von CaO und MgO. Alle Reaktionsprodukte zeigten eine bestimmte kristallographische Beziehung in Hinblick auf den Kalzitreaktanten. Des Weiteren wurden die kinetischen Parameter für die Mineralreaktion durch Temperaturserien bei einer festen Versuchslaufzeit bestimmt. Das Hauptziel der isostatischen Testserie bestand darin Informationen über die mikrostrukturelle Entwicklung, die kinetischen Parameter, die chemische Zusammensetzung und die texturelle Entwicklung der Reaktionsprodukte zu gewinnen. Die Resultate dienten als Referenz um den Einfluss der Deformation auf die Mineralreaktion zu quantifizieren.

Kapitel drei befasst sich mit dem Effekt von nicht-isostatischer Deformation auf die Bildungen von Dolomit und Magnesio-Kalzit zwischen Kalzit und Magnesit Einkristallen. Deformation wurde entweder durch triaxiale Kompression oder durch Torsion erreicht. Triaxiale Kompression bis zu 38 MPa axialer Spannung bei festgelegter Zeit zeigte keinen signifikanten Einfluss von Spannung und Verformung auf die Dolomitproduktion. Eine Zeitserie bei ähnlichen axialen Spannungen und geringen Verformungen resultierten in vergleichbaren Wachstumsraten für Dolomit und Magnesio-Kalzit wie unter isostatischen Bedingungen. Geringfügig schnellere Wachstumsraten für den Magnesio-Kalzit traten in Experimenten auf bei denen die Verformung größer als 0.1 war. Hohe Verformungen bei ähnlichen Spannungen

wurde durch die Aktivierung zusätzlicher Gleitsysteme im Kalzit Einkristall und mobile Versetzungen im Magnesio-Kalzit erreicht, welche schnelle Wege für Diffusion bereitstellen. In Torsionsexperimenten wurde eine graduelle Abnahme der Dolomitsaumdicke und des Magnesio-Kalzits beim Überschreiten einer kritischen Scherverformung festgestellt. Während der Deformation kam es zu einer Umorientierung der kristallographischen Achsen von Dolomit und Magnesio-Kalzit hinsichtlich des externen Bezugsystems. Ein direkter Effekt der Mineralreaktion auf die Deformation konnte auf Grund der relative geringen Reaktionsproduktdicke nicht gesehen werden.

Im vierten Kapitel wurden der Korngrößeneinfluss des Ausgangsmaterials sowie die Anwesenheit von Wasser auf die Reaktionskinetik getestet. In dieser Testserie wurde polykristallines Material in Kontakt zu Einkristallen gebracht oder zwei polykristalline Materialien wurden als Reaktanten benutzt. Isostatisches Ausheizen resultierte in verschiedenen Dolomitsaum- und Magnesio-Kalzitdicken in Abhängigkeit der Korngröße der Reaktanten. Bei kleinen Korngrößen des Magnesits war der Reaktionsfortschritt erhöht, da Korngrenzen Wege für schelle Diffusion boten und viele Nukleationskeime erlaubten. Im Gegensatz zu isostatischen Bedingungen führten triaxiale Kompression und Torsion zu geringen Dolomitsaumdicken. Die Ursache hierfür war auftretendes Kornwachstum im polykristallinen Magnesit während der Deformation. Für den Magnesio-Kalzit wurde ein beschleunigtes Wachstum während der Deformation festgestellt, da der Massentransport entlang von Korngrenzen begünstigt wurde. Die Reaktionskinetik zwischen zwei Einkristallen wurde durch die Anwesenheit von zusätzlichem Wasser nicht signifikant beeinflusst.

Das fünfte Kapitel enthält die generellen Schlussfolgerungen die für die Wechselwirkung von Mineralreaktion und Deformation im Karbonatsystem getroffen werden konnten.

Basierend auf den Resultaten dieser Studie zeigt Kapitel sechs abschließend auf, welche Möglichkeiten es für zukünftige Arbeiten im Karbonatsystem gibt.

Statement of the contributions

The cumulative thesis "Interplay between mineral reaction and deformation via structural defects" is comprised of two published papers and one submitted manuscript under peer-review. In all papers and the manuscript the Ph.D. candidate is the first author. The articles and the manuscript made up single chapters (CHAPTERS 2, 3, 4) including their own abstract, introduction, methodology, discussion, conclusion and acknowledgement. In addition, a general introduction, conclusion and outlook were written for this thesis exclusively. References of all citations are summed up in the chapter "References". Articles used in this thesis are:

CHAPTER 2: Helpa, V., E. Rybacki, R. Abart, L. F. G. Morales, D. Rhede, P. Jeřábek, and G. Dresen. 2014. "Reaction Kinetics of Dolomite Rim Growth." *Contributions to Mineralogy and Petrology* 167 (4): 1001. doi:10.1007/s00410-014-1001-y. (©Springer-Verlag Berlin Heidelberg 2014; with permission of Springer).

CHAPTER 3: Helpa, V., E. Rybacki, L. F. G. Morales, and G. Dresen. 2015. "Influence of Stress and Strain on Dolomite Rim Growth: A Comparative Study." *Contributions to Mineralogy and Petrology* 170 (2): 16. doi:10.1007/s00410-015-1172-1. (©Springer-Verlag Berlin Heidelberg 2015; with permission of Springer).

CHAPTER 4: Helpa, V., E. Rybacki, L. F. G. Morales, and G. Dresen. 2015. "Influence of grain size, water and deformation on dolomite reaction rim formation." *American Mineralogist, Special Collection: Mechanisms, rates, and timescales of geochemical transport processes in the Crust and Mantle,* submitted (under peer-review). (with permission of the Mineralogical Society of America).

Declaration

This work was funded by the Deutsche Forschungsgemeinschaft within the framework of FOR 741, project RY 103/1-1, which is gratefully acknowledged. Investigations and analyses presented in this thesis were mainly done by the Ph.D. candidate (Vanessa Helpa). Work performed by others is clearly indicated and quoted as references. Collaborative researchers are listed as co-authors in each article. Help with the experimental equipment and scientific discussions with other scientists are kindly acknowledged.

All experiments and analytical investigations were conducted at the GeoForschungsZentrum (GFZ) Potsdam, Germany. Handling of the Paterson gas-deformation apparatus was supervised by Michael Naumann. The Ph.D. candidate and Stefan Gehrmann (GFZ) prepared the thin sections and other samples used in this thesis. Analytical equipment like the Transmission electron microscope (TEM) and the electron microprobe (EMP) was used in collaboration with the responsible technicians Richard Wirth and Dieter Rhede. X-ray diffraction and water content analyses were conducted by Hans-Peter Nabein and Rudolf Naumann. Electron Backscattered Diffraction (EBSD) data was produced by Luiz Morales. Erik Rybacki (GFZ) helped with the numerical analyses of the experimental data, good mentoring and discussions. The work performed for this study was mainly done by the Ph.D. candidate under the supervision of Georg Dresen (GFZ).

Danksagung

Zunächst einmal möchte ich mich bei meinem Betreuer Georg Dresen bedanken, der es mir ermöglicht hat an diesem Projekt zu arbeiten und all die Erfahrungen zu sammeln die damit einhergehen. Des Weiteren möchte ich mich bei der gesamten Forschergruppe FOR 741, insbesondere bei Wilhelm Heinrich und Rainer Abart bedanken. Die Gruppe war ein sehr gutes Forum für Diskussionen und konstruktive Ideen.

Mein größter Dank gilt Erik Rybacki der sich in den vergangenen Jahren stets Zeit für mich genommen hat. Sei es für die Hilfe bei Versuchsauswertungen, Diskussionen oder diversen Auseinandersetzungen mit einer gewissen Software. Neben den wissenschaftlichen Aspekten danke ich ihm vor allem für seine „Ruhrpott-Art“. Michael Naumann und „Jerry“ danke ich für die unzähligen, zeitintensiven Versuche. Außerdem danke ich Michael für das Vertrauen selbst an „Jerry“ arbeiten zu dürfen und für die Beantwortung sämtlicher technischen Fragen. Es hat wirklich Spaß gemacht und ich habe ständig neue Sachen dazu gelernt.

Danken möchte ich selbstverständlich auch allen ehemaligen und jetzigen Sektionsmitgliedern deren gesamte Aufzählung die Kapazität der Danksagung überschreiten würde. Deswegen beschränke ich mich auf meine direkten Bürokollegen: Tobias, Masline, Zita, Jessica, Maike und Oliver. Besonders hervorgehoben sei die Unterstützung von Olli, der durch seine Snickers-Versorgung nicht nur mir durch so manchen nachmittäglichen Tiefpunkt geholfen hat.

Bei allen anderen Kollegen, bedanke ich mich recht herzlich für jegliche Bespaßung und Ermutigung während der Mittagspause und etlichen „after work beerclubs“. Vor allem bei Luiz Morales aka „Prince charming“ für seinen großartigen Sarkasmus. Neben den vielen Kollegen möchte ich mich noch explizit bei Rita Hamlischer dafür bedanken, dass sie stets versucht alle Doktoranden bestmöglich zu unterstützen.

Zu guter Letzt aber sicher nicht weniger Wichtig danke ich meiner gesamten Familie und meinen Freunden, die mich zu jeder Zeit bedingungslos unterstützt haben. Ich freue mich euch eure Lieblingsfrage „Wann bist du mit deiner Dokotorarbeit fertig?“ bald beantworten zu können.

Auch danke ich den Erfindern von Ph.D. comics, die es vermögen das Leben jedes Doktoranden detailgetreu wieder zu geben. Prof. Smith lehrte mich eine wichtige Lektion:

„In academia we don’t use the word problem, we call them challanges or issues.“

Table of contents

1 General introduction

1.1 Mineral reactions in nature

Mineral reactions are a prominent feature within the Earth caused by a disequilibrium of adjacent minerals and mineral composition with thermodynamic boundary conditions (ASHWORTH AND SHEPLEV 1997; ABART AND SPERB 2001; KELLER ET AL. 2006; KELLER, WUNDER, ET AL. 2008; KELLER, WIRTH, ET AL. 2008). Replacement of metastable phases usually occurs along grain boundaries forming polycrystalline reaction rims or coronas (KELLER, WIRTH, ET AL. 2008; JOACHIM ET AL. 2010). Such mineral assemblages may evolve during prograde or retrograde metamorphism due to changes in *P-T-x* (pressure-temperature-chemical composition) conditions. To derive the metamorphic conditions from the microstructure of reaction products, knowledge of the component mobility and the transport mechanisms are required. Multiple investigations have been done with focus on coronas and component mobility for different geological systems (JOESTEN 1977; BRADY 1983; ASHWORTH AND BIRDI 1990; ASHWORTH AND SHEPLEV 1997; ASHWORTH ET AL. 1998; KELLER, WUNDER, ET AL. 2008; JOACHIM ET AL. 2009). Up to now, isostatic equilibrium stability fields of mineral phases are used to reconstruct the *P-T* conditions because knowledge about the influence of non-isostatic deformation conditions on phase transformation is still scarce. It may be possible that phase boundaries shift or reactions are faster/slower at non-isostatic conditions.

In nature, shear zones provide a good opportunity to study the influence of deformation on mineral reactions directly. Adjacent rocks of the similar chemical composition are highly deformed in the central shear zone, whereas wall rocks are undeformed. There, enhanced reaction rates are linked to the highly deformed shear zones, mostly accompanied with fluid infiltration (KERRICH ET AL. 1980; NEWMAN ET AL. 1999; KELLER ET AL. 2004; GONCALVES ET AL. 2012). Water supports fast mass transport and effectively facilitates phase transformation (RUBIE 1986). During deformation, the reaction progress may be influenced by generation and movement of dislocations, changes in the chemical potentials or modification of the microstructure and texture (BRODIE AND RUTTER 1985; KELLER ET AL. 2010). As a consequence diffusive mass transfer necessary for mineral reactions is directly affected by imposed deformation. In addition, deformation-induced elastic and plastic strain energy can add to the driving force of the reaction (HOBBS, ORD, AND REGENAUER-LIEB 2011). In nature it is often not possible to unambiguously separate the contributions of deformation and fluid infil-

tration to the reaction progress. With respect to deformation, phase transformations may be most important if reaction products have considerably different rheological properties compared to reactants. Fine-grained neominerals may induce localized deformation and encourage shear zone formation by a change in deformation mechanism from grain size insensitive to grain size sensitive creep (e.g., KERRICH ET AL. 1980; RUBIE 1983; BRODIE AND RUTTER 1985; NEWMAN AND DRURY 2010).

1.2 Element transport

Element transport occurs on varying spatial scales ranging from the regional scale to the microscopic scale. On the regional scale, whole rock formations can be involved while on the microscopic scale chemical compositions of individual grains change. In general, the element transport is forced by disequilibrium in chemical compositions/potentials of adjacent reactants. To attain chemical equilibrium an exchange of mass is required, which can lead to the formation of new phases or mineral assemblages.

In many geological settings, the presence of fluids may have an important impact on the mass transport and the emerging metamorphic reactions. Existing fluids can change stability fields of certain minerals, interact with the rock and supply or extract heat (FERRY 1983). The transport mechanism may be controlled by fluid-infiltration requiring a flowing fluid or diffusion through a pore fluid (FLETCHER AND HOFMANN 1973). In the absent of fluids or in materials with low permeability, mineral reactions are commonly diffusion-controlled (ASHWORTH AND BIRDI 1990). Diffusional mass transport is highly effective on the centimeter scale and can lead to large chemical variations within a small volume (BRADY 1977). Newly formed reaction products are commonly characterized by a spatial organized microstructure and strong chemical variations, e.g. reaction layers for a one-dimensional mass transport (FISHER 1978).

For metals diffusion mechanisms and –rates are well known, which is contrarily to geomaterials. Complex mineral structures and relatively sluggish diffusion rates complicate the examination (PUTNIS AND MCCONNOLL 1980). Therefore, laboratory studies are essentially to gain information about element transport rates under constrained conditions. Thermodynamic models for a diffusion-controlled element exchange then allow extracting diffusion coefficients of the mobile components (e.g. FISHER 1973; FISHER 1978; JOESTEN 1977;

JOACHIM ET AL. 2009). Element exchange rates as determined from experiments can then be extrapolated to temperature and times, which are relevant to the geological conditions.

1.3 Diffusion pathways

Mass transfer of components is essential for mineral reactions to proceed. In rocks, several possible diffusion pathways are available, strongly depending on the microfabric of the rock. WATSON AND BAXTER (2007) categorized diffusion in geological media into the following 4 main types (**Figure 1.1**).

a) Volume diffusion
b) Defect diffusion
c) Grain-boundary diffusion
d) Surface diffusion

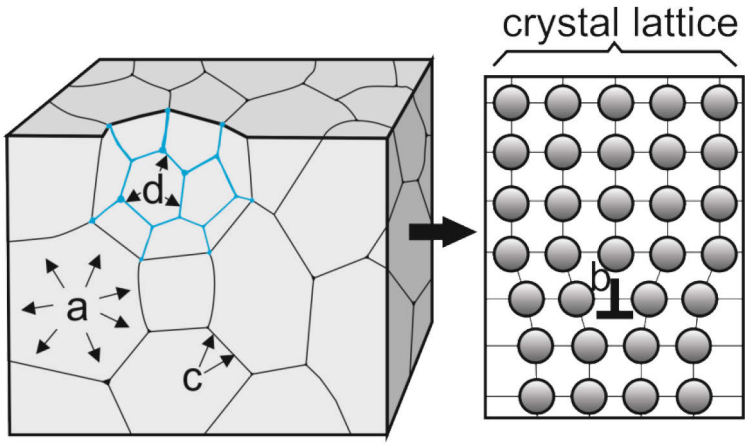

Figure 1.1 Schematic sketch of diffusion pathways available in rocks. Mass transfer can either occur in the grain interiors by volume diffusion and/or along defects or along grain boundaries (modified after WATSON AND BAXTER 2007).

Volume and defect diffusion are most important pathways in single crystals or coarse-grained materials. Here, the transport of matter is restricted to the crystal lattice by volume diffusion or along dislocations. Defects distort the crystal lattice and may provide fast diffusion pathways enhancing reaction kinetics. In response to an applied stress and/or reaction-induced volume changes multiple types of structural defects may be generated. In particular, 0-D point defects (vacancies, interstitials), 1-D line defects (screw/edge dislocations), and 2-D planar structures (twin boundaries, grain boundaries, interphase boundaries etc.). Generally, diffusion of matter by volume diffusion is slow compared to diffusion along line- and planar defects. The density of defect types may vary with strain (e.g., dynamic recrystallization) or mineral reaction.

In fine-grained polycrystalline material it is likely that grain boundary diffusion predominates, which is faster and operative at larger spatial scale (DOHMEN AND MILKE 2010).

Grain boundary diffusion refers to the migration of matter between adjacent grains of a different crystallographic orientation or along plate boundaries. In the presence of a fluid, mass transport might be even accelerated (MILKE ET AL. 2009; GARDÉS ET AL. 2012; MILKE ET AL. 2013). All of the listed diffusion pathways have distinct diffusion coefficients in a specific mineral phase. Generally, a mix of these diffusion types occur in natural materials, depending on for instance temperature, grain size, lattice defects, phase boundaries and the presence of fluids. Consequently only the effective diffusion can be determined, which is controlled by the slowest species along its fastest pathway.

Reaction rim growth can either be interface- or diffusion-controlled. For an interface-controlled reaction, the rim thickness increases linear with time (e.g., SIEBER, WERNER, AND HESSE 1997; GÖTZE 2015). In contrast, reaction rims grow linear with the square root of time if growth is diffusion-controlled (e.g., ASHWORTH ET AL. 1998; MILKE AND HEINRICH 2002; JOACHIM ET AL. 2009).

1.4 Previous experimental work on the influence of deformation on mineral reactions

Laboratory tests on the influence of deformation on mineral reactions are still scarce, but got into the focus of research recently. Previous experimental studies reported on deformation–enhanced mineral reactions in the systems feldspar-olivine (DE RONDE ET AL. 2004; DE RONDE AND STÜNITZ 2007), biotite-plagioclase-quartz (HOLYOKE AND TULLIS 2006), periclase-ferropericlase (HEIDELBACH ET AL. 2009) and dolomite decomposition (DELLE PIANE, BURLINI, AND GROBETY 2007) in accordance with observations in nature. The enhanced reaction rates are mostly associated with grain size reduction and/or grain boundary migration. In addition, strain weakening occurred by a reduction in grain size and supporting deformation by diffusion creep partly accompanied by grain-boundary sliding. Nevertheless, quantitative investigations on the influence of stress and strain are still rare.

In the first funding period of the research group FOR 741, the influence of uniaxial stress on spinel rim formation at ambient pressure was investigated (GÖTZE ET AL. 2010; KELLER ET AL. 2010). As starting materials either oriented single crystals of periclase and sapphire or periclase in contact to polycrystalline corundum were used to observe spinel reaction rim production at the initial contact interface by applying uniaxial stresses between 1.2

and 29 MPa (**Figure 1.2 a**). It turned out that the microfabric of starting materials, polycrystalline or single crystal, has a substantial influence on the growth behavior with applied uniaxial stress (**Figure 1.2 b**).

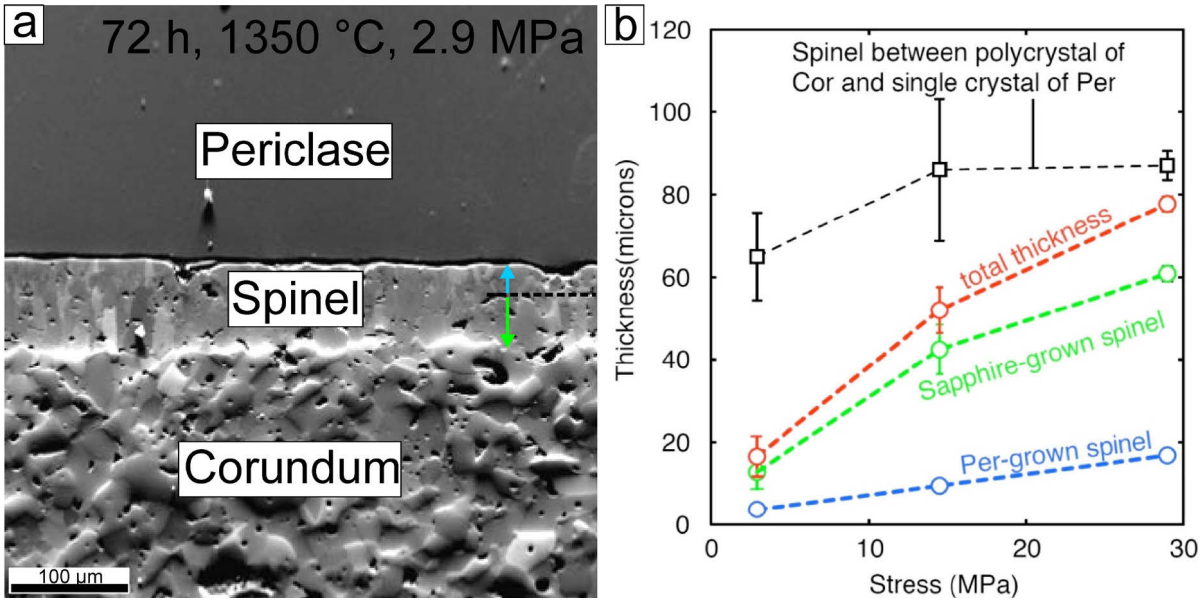

Figure 1.2 (**a**) Spinel rim formed in between a periclase single crystal and polycrystalline corundum at 1350 °C temperature under a uniaxial stress of 2.9 MPa for 72 h. The initial interface is indicated by the *black dashed line* and growing directions are represented by *colored arrows* (modified after GÖTZE ET AL. 2010). (**b**) Influence of uniaxial stress on spinel rim layer thickness annealed at 1350°C for 157 h (KELLER ET AL. 2010). Measured total spinel rim width formed between periclase single crystals and corundum (*black broken line*) is hardly influenced by an applied stress up to 29 MPa. Spinel rim growth between two single crystals is continuously enhanced by increasing applied uniaxial stress (*red broken line*). Within the spinel rim, growth rates in the two domains are differently influenced depending on whether spinel growth with sapphire (*green broken line*) or with periclase (*blue broken line*).

Experiments performed at T = 1350 °C, t = 157 h and increasing uniaxial stresses from 2.9 to 29 MPa resulted in enlarged spinel rims thicknesses at higher applied stresses (**Figure 1.2 b**). In between corundum and periclase, spinel rim thickness is increased by a factor of 1/3 only, while the spinel rim produced between two single crystals has a 3 times larger thickness at 29 MPa compared to 2.9 MPa. This observation is explained by the textural evolution of spinel with increasing stress.

If polycrystalline corundum is used, spinel grains have a random crystallographic orientation with no relations to the reactants. In contrast, spinel rims formed between single crystals have either a strong epitactic relation with respect to periclase (small palisade domain) or sapphire (large palisade domain) at low stresses. With increasing applied uniaxial stress, the periclase-grown spinel inherits this strong relation, while grain boundaries of sapphire-grown spinel rearrange and rotate out of epitaxy (KELLER ET AL. 2010). Estimations of the plastic and

elastic strain energy reveal only minor contributions to the Gibbs free energy of the reaction, with fractions of $2 \cdot 10^{-6}$ and $2 \cdot 10^{-4}$, which cannot explain the enhanced growth rates observed in tests with uniaxial stress. Moreover, an added amount of high angle grain boundaries providing fast diffusion pathways can be ruled out, because grain coarsening occurs under stress. Consequently, the authors claimed the observed textural and microstructural changes within spinel rims to be responsible for the accelerated reaction kinetics.

This example does not only point at the importance of textural changes within the reaction product, but also shows the dependence of the reaction rate on the microfabric of reactant phases.

1.5 Goal of this study

The main goal of this study is to gain a better understanding about the interplay between deformation and mineral reactions. Generally, the influence of non-isostatic stress/strain conditions on the mineral reactions is disregarded, due to the limitation of data and complex interplays of deformation and fluid infiltration in nature (SEE CHAPTER 1.1). Thereby, the effect of stress and strain could be diverse, like changing the stability field of reactant phases or accelerating/hindering the diffusion kinetics of the reaction. As described in CHAPTER 1.2 deformation can induce multiple defects, providing fast diffusion pathways and consequently affect mass transport. Also, stress-induced textural changes may influence growth rates considerably (CHAPTER 1.3).

To attain information about the influence of deformation on the mineral reaction, laboratory experiments under controlled conditions are the method of choice. Using single crystals as reactants simplifies the starting orientation relationship and facilitates texture analyses of the reaction products. The first part of this thesis addresses the reaction kinetics of dolomite rim growth under isostatic conditions and serves as a reference frame for a quantitative analysis of deformation experiments. Tests under isostatic conditions answer the following questions:

- How do the evolved microstructures look like and what is the chemical composition of the reaction products?
- What controls the reaction between calcite and magnesite single crystals?
- Is there a temperature and/or time dependence?

- What are the kinetic parameters for the reaction?
- Is there any crystallographic relationship between reactants and reaction products?

In the second part, deformation experiments were performed either by applying a constant triaxial load or by twisting the sample. Starting materials and temperature-pressure conditions were similar to the previous study, allowing a direct comparison. Besides answering the questions above, some additional questions were asked:

- What is the influence of triaxial stress/strain on the mineral reaction?
- Is there a significant change in the driving force due to stored strain energy?
- What is the effect of torsion?
- Do we see a change growth rate?
- What is the strength of the materials and what is the deformation mechanism?
- Do we see strain partioning?

In the last part of this thesis, the focus is on the influence of starting materials' grain sizes and the presence of water. Therefore single crystals and polycrystalline starting materials were used to check for the grain size sensitivity of the reaction rate. Tests were performed under isostatic annealing, triaxial deformation and torsion at similar conditions as in the tests before. The main task of these experiments was to answers these questions:

- What is the influence of polycrystalline starting material on the reaction product thickness, microstructure and chemical composition?
- Is there any recognizable crystallographic preferred orientation?
- Are the reaction kinetics accelerated by the presence of water?

2 Reaction kinetics of dolomite rim growth

2.1 Abstract

Reaction rims of dolomite ($CaMg[CO_3]_2$) were produced by solid-state reactions at the contacts of oriented calcite ($CaCO_3$) and magnesite ($MgCO_3$) single crystals at 400 MPa pressure, 750-850 °C temperature and 3-146 h annealing time to determine the reaction kinetics. The dolomite reaction rims show two different microstructural domains. Elongated palisades of dolomite grew perpendicular into the magnesite interface with length ranging from about 6 µm to 41 µm. At the same time, a 5-71 µm wide rim of equiaxed granular dolomite grew at the contact with calcite. Platinum markers showed that the original interface is located at the boundary between the granular and palisade-forming dolomite. In addition to dolomite, a 12 to 80 µm thick magnesio-calcite layer formed between the dolomite reaction rims and the calcite single crystals. All reaction products show at least an axiotactic crystallographic relationship with respect to calcite reactant, while full topotaxy to calcite prevails within the granular dolomite and magnesio-calcite. Dolomite grains frequently exhibit growth twins characterized by a rotation of 180° around one of the $[11\bar{2}0]$ equivalent axis. From mass balance considerations it is inferred that the reaction rim of dolomite grew by counter diffusion of MgO and CaO. Assuming an Arrhenius type temperature dependence, activation energies for diffusion of CaO and MgO are E_a(CaO) = 192 ± 54 kJ/mol and E_a(MgO) = 198 ± 44 kJ/mol, respectively.

2.2 Introduction

Mineral reactions in the solid-state are ubiquitous in the Earth's crust and mantle. Unless deformed or overprinted, the product phases of such solid-state reactions are commonly located along former phase boundaries between reactants, forming polycrystalline or polyphase reaction rims or coronas (ASHWORTH ET AL. 1998; KELLER ET AL. 2006; KELLER, WIRTH, ET AL. 2008; KELLER, WUNDER, ET AL. 2008). They may contain information about the pressure, temperature and time conditions of their formation and therefore provide a useful indication on the geological history (KELLER, WIRTH, ET AL. 2008; JOACHIM ET AL. 2010). For a solid-state reaction under "dry" conditions, the necessary transfer of matter between the reactants

occurs by diffusion leading to reaction rim growth with kinetics that depends on *P*-*T*-*t* conditions (LASAGA 1983). To constrain the diffusion kinetics using microstructure analysis, knowledge of the component mobility and the transport mechanisms are required. In a polyphase aggregate, the transfer of chemical components may occur via a combination of grain boundary- and volume diffusion, with grain boundary (GB) diffusion typically being several orders of magnitude faster than diffusion through the volume of the grains. GB diffusion thus is effective over larger spatial scales (DOHMEN AND MILKE 2010). However, at elevated temperatures the contribution of volume diffusion to the bulk mass transfer may increase considerably owing to higher activation energy than for grain boundary diffusion (MROWEC 1980). In general, the growth behavior of solid-solid reaction rims can be described by the relation: $\Delta x^n = kt$, where Δx is the thickness of the reaction layer, k is a rate constant, t is time and n is a parameter depending on the reaction controlling mechanism (SCHMALZRIED 1978; KELLER ET AL. 2010). For interface-reaction controlled growth $n = 1$ and for diffusion controlled growth $n = 2$. It has been demonstrated by ABART AND PETRISHCHEVA (2011) that, after an incipient nucleation phase, reaction rim growth is initially interface reaction-controlled, replaced by diffusion-controlled growth as the rim thickness increases. From the rate of reaction rim growth in the diffusion controlled kinetic regime the mobility of the respective components can be inferred. This motivated a series of rim growth experiments that aimed to determine component mobility. Dedicated studies exist for several systems such as $CaCO_3$-SiO_2, where wollastonite is formed between calcite and quartz (MILKE AND HEINRICH 2002), MgO-SiO_2, where enstatite is formed between forsterite and quartz, or enstatite-forsterite double layers are formed between periclase and quartz (e.g., MILKE, WIEDENBECK,& HEINRICH, 2001; GÖTZE ET AL., 2009; GARDÉS & HEINRICH, 2011), and MgO-Al_2O_3 where spinel is formed between periclase and corundum (e.g., WATSON & PRICE, 2002; GÖTZE ET AL., 2009; KELLER ET AL., 2010). For grain boundary diffusion-controlled growth, the reaction kinetics may be influenced by grain size (GARDÉS ET AL. 2011; GARDÉS AND HEINRICH 2011), water content (MILKE ET AL. 2009; GARDÉS ET AL. 2012; MILKE ET AL. 2013), and non-hydrostatic stress (GÖTZE ET AL. 2010; KELLER ET AL. 2010). In contrast, little is known about diffusion-controlled reactions in the system $CaCO_3$-$MgCO_3$, i.e. the formation of dolomite [$(CaMg(CO_3)_2$] between calcite ($CaCO_3$) and magnesite ($MgCO_3$). So far, few cation diffusion data are available for diffusion in dolomite. ANDERSON (1972) determined self-diffusion of C and O in dolomite at T = 645 to 785 °C and P = 12 to 93.5 MPa and MÜLLER, CHERNIAK, & WATSON (2012) investigated cation exchange between dolomite and siderite or rhodochro-

site to determine volume diffusion of (Mn, Fe) – Mg – Ca at T = 400-625 °C, P = 0.1 MPa.

In this study reaction rims of dolomite were produced at contacts between oriented natural calcite and magnesite single crystals following the reaction:

$$MgCO_{3,solid} + CaCO_{3,solid} = CaMg(CO_3)_{2,solid} \quad \textbf{(2.1)}$$

The experiments were performed at T = 750–850 °C and P_c = 400 MPa to determine the reaction kinetics of dolomite rim growth in the carbonate system under static annealing conditions.

2.3 Experimental and analytical details

2.3.1 Starting material

The starting materials were prepared from natural calcite single crystals from Mina Prieta Linda, Naica (Chihuahua, Mexico) and Minais Gerais (Brasil) and from magnesite single crystals from Bahia (Brumado, Brasil). The chemical composition was analyzed by field emission gun electron microprobe (JEOL JXA-8500 F HYPERPROBE), using 15 keV accelerating voltage, 5 nA beam current and 1 μm beam diameter. The results are given in **Table 2.1**, revealing trace amounts of Fe and Mg in calcite. Magnesite contained impurities of Ca, Fe and traces of Mn, Ba, and Sr. The water content estimated from Vario EL III element analyzer (Elementar Analysesysteme GmbH) is about 0.15 wt.% and 0.25 wt.% in calcite and magnesite, respectively.

	Calcite ± 1σ	Magnesite ± 1σ
MgO	0.03 ± 0.04	46.08 ± 1.65
FeO	0.04 ± 0.05	0.18 ± 0.05
CaO	53.37 ± 0.76	0.26 ± 0.04
SrO	0.02 ± 0.03	0.02 ± 0.01
MnO	0.01 ± 0.03	0.04 ± 0.03
TiO_2	0.01 ± 0.02	0.01 ± 0.01
SiO_2	0.00 ± 0.01	0.01 ± 0.02
BaO	0.00 ± 0.01	0.04 ± 0.03
CO_2	46.51± 0.74	53.36 ± 1.66

Table 2.1 Composition of starting materials in wt.%. Values represent mean data based on 5 point analyses. CO_2 contents were calculated assuming an oxide total of 100%.

2.3.2 Annealing experiments

Cylindrical samples of 3-5 mm length and 7 mm diameter were drilled out of the single crystals, oriented with the cylinder axis perpendicular to the cleavage planes of the rhombohedra [$(10\bar{1}4)$, $(\bar{1}104)$, $(0\bar{1}14)$]. Subsequently samples were polished with diamond powder to a surface roughness of ~1 µm. In three experiments (CaMg-13, CaMg-14, CaMg-15; **Table 2.2**), both contact surfaces of calcite and magnesite were polished to 0.25 µm finish and sputtered with a thin platinum layer (<2nm), which served as a marker to locate the initial calcite-magnesite interface after formation of the rims. The assembly for each run consisted of a calcite-magnesite sandwich, located between alumina spacers and adjacent alumina pistons **Figure 2.1**.

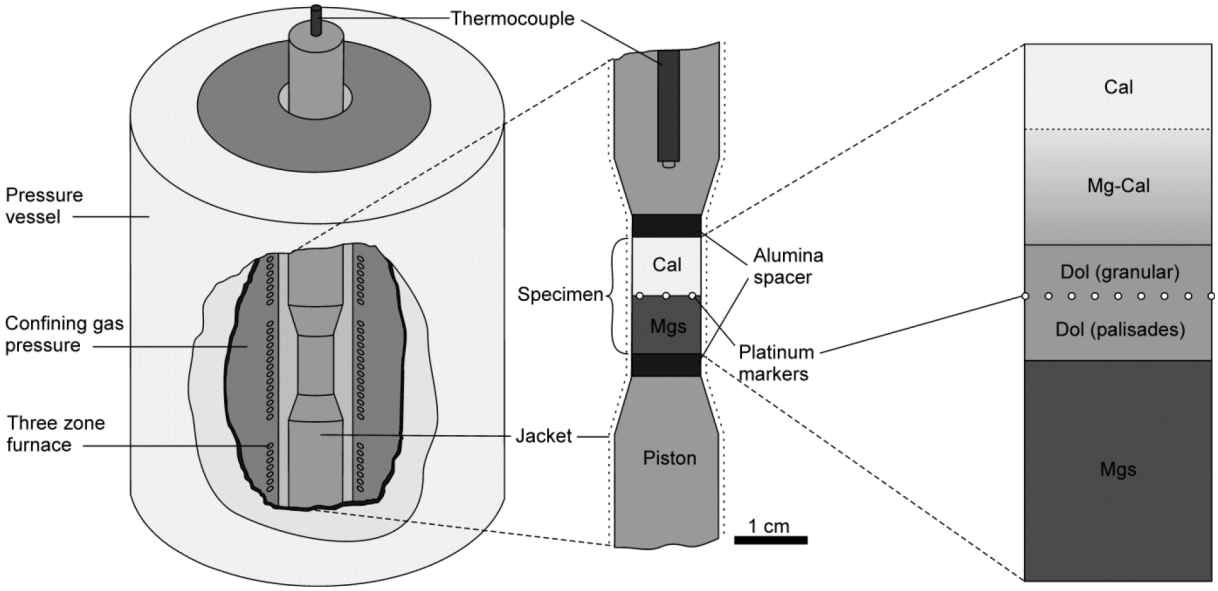

Figure 2.1 Experimental seup. The sample assembly consists of polished cylinders of calcite and magnesite single crystals. The dolomite reaction rim grows from the initial calcite-magnesite contact into both directions. The initial calcite-magnesite contact is marked by platinum markers (*white dots*) in some experiments. Adjacent magnesio-calcite evolved next to calcite reactant.

The whole assembly was jacketed by a copper-sleeve to prevent intrusion of the confining pressure medium (argon-gas). Temperature was measured using a Pt/Pt-13%Rh (R-type) thermocouple 3 mm from the sample assembly. All experiments were performed in an internally heated pressure vessel using a Paterson type gas deformation apparatus (PATERSON 1970) at a confining pressure of P_c = 400 MPa. Temperatures were kept constant at 750 °C, 800 °C, 825 °C or 850 °C with a heating rate of 20 °C/min and a cooling rate of 2 °C/min (**Table 2.2**). After the experiments, the jacketed sample assembly was cut along the cylinder axis using a slow-speed diamond saw, embedded in epoxy and the surfaces were polished

down to 1 µm roughness for analysis of the reaction rim.

The run conditions and the results of 13 annealing experiments are presented in **Table 2.2**. Dolomite reaction rims were produced during static annealing tests of 13 samples with annealing times between 3 and 146 hours (**Table 2.2**). **Figure 2.2** shows the polybaric (200-850 MPa) phase diagram for $CaCO_3$-$MgCO_3$ adopted from GOLDSMITH AND HEARD (1961), revealing that both dolomite and magnesio-calcite are stable at the applied experimental conditions. Compared to the solvi shown in **Figure 2.2**, the experimental pressure of 400 MPa slightly increases the solubility of $MgCO_3$ in calcite by about 1 mol% at 750 °C and 2 mol% at 850 °C, respectively (GOTTSCHALK AND METZ 1992).

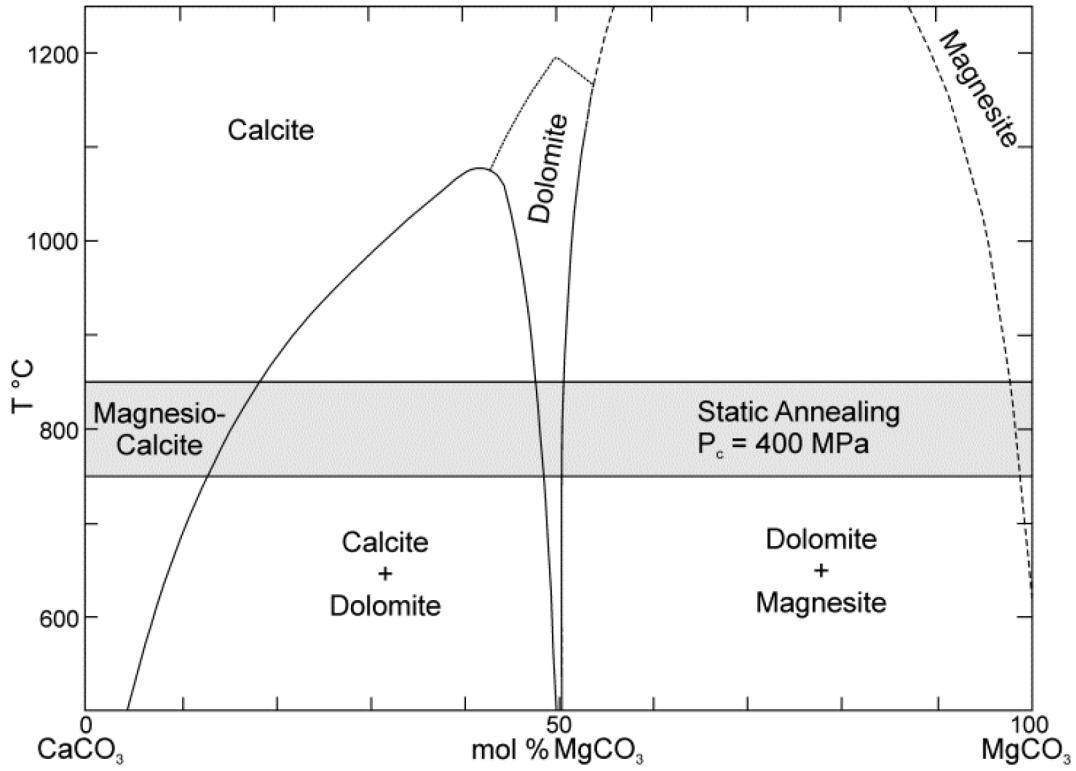

Figure 2.2 Phase relations of calcite, dolomite and magnesite in the Ca-Mg carbonate system (modified after GOLDSMITH AND HEARD 1961). The experimental temperature range for static annealing tests is indicated by the grey box.

Experiment	T (K)	t (h)	Δx_{Dol} (µm)	Δx_{Pal} (µm)	Δx_{gran} (µm)	Δx_{Mg-Cal} (µm)	Δa_{Pal} (µm)	Δa_{gran} (µm)	Δa_{Mg-Cal} (µm)	log D_{CaO} (m²/s)	log D_{MgO} (m²/s)
CaMg-02	1073	74.03	36.3 ± 5.3	16.5 ± 3.1	20.2 ± 4.3	55.0 ± 10.7	3.6 ± 0.9	5.4 ± 1.9	39.0 ± 20.1	-14.4 ± 0.3	-14.2 ± 0.3
CaMg-03	1023	73.95	14.9 ± 5.3	10.5 ± 4.0	7.5 ± 3.0	40.9 ± 10.4	3.1 ± 1.1	2.7 ± 1.1	23.3 ± 12.9	-14.6 ± 0.4	-14.6 ± 0.4
CaMg-04	1023	50.07	17.5 ± 5.7	9.0 ± 2.8	8.3 ± 3.1	27.3 ± 8.3	2.9 ± 0.9	3.2 ± 1.3	22.2 ± 16.0	-14.6 ± 0.5	-14.5 ± 0.5
CaMg-05	1023	145.77	26.0 ± 6.0	12.3 ± 3.0	13.8 ± 4.4	37.2 ± 6.1	3.9 ± 1.0	4.0 ± 1.3	37.3 ± 17.3	-14.8 ± 0.4	-14.7 ± 0.4
CaMg-06	1073	144.71	40.9 ± 7.1	16.2 ± 4.2	24.5 ± 4.9	74.2 ± 11.6	4.3 ± 1.4	4.2 ± 1.4	44.3 ± 23.9	-14.7 ± 0.3	-14.4 ± 0.3
CaMg-07	1073	84.82	30.0 ± 7.2	14.7 ± 3.3	17.1 ± 5.1	37.0 ± 7.3	4.1 ± 1.2	4.6 ± 1.4	35.7 ± 15.4	-14.4 ± 0.4	-14.3 ± 0.4
CaMg-08	1073	48.1	25.4 ± 7.1	12.1 ± 3.4	14.8 ± 4.2	48.5 ± 8.2	3.3 ± 0.8	3.9 ± 1.2	38.2 ± 23.4	-14.4 ± 0.5	-14.2 ± 0.5
CaMg-09	1023	2.44	2.9 ± 1.2	NA	NA	12.1 ± 4.2	NA	NA	12.7 ± 4.7	NA	NA
CaMg-10	1123	74.15	103.7 ± 33.5	41.3 ± 10.2	71.0 ± 18.2	80.3 ± 21.2	5.0 ± 1.2	4.3 ± 1.3	45.8 ± 32.9	-13.4 ± 0.7	-13.4 ± 0.7
CaMg-12	1073	4.03	11.3 ± 4.2	6.0 ± 2.4	5.4 ± 2.4	20.0 ± 5.5	1.7 ± 0.4	2.6 ± 0.9	18.5 ± 9.7	-13.9 ± 0.6	-13.8 ± 0.6
CaMg-13*	1098	74.92	40.1 ± 9.5	17.3 ± 5.1	17.0 ± 5.0	52.3 ± 13.3	4.3 ± 1.1	1.4 ± 0.8	42.0 ± 27.7	-14.2 ± 0.5	-14.2 ± 0.5
CaMg-14*	1073	28.94	14.2 ± 4.9	8.3 ± 3.1	5.8 ± 2.5	31.2 ± 8.3	2.4 ± 0.8	2.9 ± 1.2	26.1 ± 15.4	-14.4 ± 0.5	-14.4 ± 0.5
CaMg-15*	1023	29.13	13.0 ± 1.6	6.8 ± 2.4	5.0 ± 2.8	31.5 ± 10.2	2.6 ± 0.6	2.5 ± 0.8	26.6 ± 14.0	-14.6 ± 0.2	-14.6 ± 0.2

*Platinum marker experiment

Table 2.2 Average thickness of entire dolomite (Δx_{Dol}), dolomite palisades (Δx_{Pal}), granular dolomite layers (Δx_{gran}), and magnesio-calcite (Δx_{Mg-Cal}). a_{Pal}, a_{gran} and a_{Mg-Cal} are the mean grain diameter of dolomite palisades, granular dolomite and magnesio-calcite, respectively. D_{CaO} and D_{MgO} are the derived diffusion coefficients of CaO and MgO. Uncertainties are given as 1σ value.

2.3.3 Analytical methods

For determination of the dolomite and magnesio-calcite reaction layer thicknesses we used an optical microscope (Leica DM RX) to obtain a complete set of reflected-light micrographs across the whole sample diameter. The width of reaction rims was subsequently analyzed by digitizing the location of phase boundaries and calculation of average values owing to the relatively large thickness variation up to 41% along a single profile. The associated run durations were corrected for additional growth during heating and cooling ramps (LASAGA 1983), but the effect is negligible. Microprobe analysis of the composition profiles across selected reaction rims was performed by quantitative line scans using wavelength dispersive X-ray (WDS) measurements, counting only the major elements Ca (Kα, PETJ) and Mg (Kα, TAP). For the analysis, we applied an accelerating voltage of 15 kV and a beam current of 5 nA. Counting time was 5 s on the peak, step size 2 µm and the beam diameter was 1 µm. The crystallographic orientations of the reactant and product phases were measured using a dual-beam scanning electron microscope (FEI Quanta 3d FEG SEM-FIB), equipped with an electron backscatter diffraction detector (EBSD, TSL DigiView) and a semi-quantitative energy dispersive spectroscopy (EDS) mapping device. Since calcite, dolomite and magnesite have very close unit cell parameter a, b, c the EBSD patterns of these three phases are very similar. Therefore, we used EBSD and EDS mapping to discriminate the three minerals by measuring the Mg and Ca content. First, we mapped the reactants and the reaction rim using only the calcite reflector list, together with EDS analysis. Subsequently, we identified the three-phases based on the Mg/Ca ratios (e.g., Mg-rich – magnesite; Mg/Ca – dolomite; Ca-rich – calcite). Finally, the inspected area was remapped using the reflectors of all three phases. The magnesio-calcite was discriminated separately using microprobe analysis. For EBSD analysis, the samples were first mechanically polished to 0.25 µm roughnesses using a diamond paste and afterwards chemically-mechanically polished for one hour using an alkaline solution of colloidal silica. To avoid carbon coating, measurements were conducted in low-vacuum with a chamber pressure of 10 Pa of H_2O. Automatic mappings of selected areas were performed using an accelerating voltage of 15 keV, a step size between 0.5 and 2 µm, a working distance of 15 mm and a beam current of 8 nA. The TSL-OIM software (ADAMS, WRIGHT, AND KUNZE 1993) was used to index and analyze the EBSD patterns. Post-acquisition treatment of the raw EBSD data included the standardization of the confidence index (CI) and the CI correlation between neighbor points, assuming a value of 0.2. After processing, the points with CI<0.2 were removed from the datasets to avoid incorrect measurements. In general, the CI ranges

from 0 to 1 and quantifies the relationship between the number of votes that each phase receives during the indexation of patterns in EBSD mapping. A CI value of 0.2 indicates that the patterns are correctly indexed by about ~99%. Pole figures were plotted as one point per grain in a reference frame where the E-W plane is parallel to the reaction interface, and the pole of this plane indicates the growing direction (GD) of the reaction rim.

2.4 Results

2.4.1 Microstructure of reaction rims

All experiments resulted in polycrystalline dolomite reaction rims with two spatially separated regions of 1) elongated palisades oriented perpendicular to the interface with magnesite and 2) granular equiaxed dolomite grains in contact with calcite. In addition, the pure calcite reactant close to the dolomite rim transformed to polycrystalline magnesio-calcite. The layer width was defined petrographically by the occurrence of new formed grains using an optical microscope. Microprobe analyses confirm these new formed grains to be magnesio-calcite with decreasing magnesium content towards pure calcite (see **Figure 2.7**). The thickness of the magnesio-calcite layer is about 4 times that of the entire dolomite rim (**Table 2.2**). The size of the magnesio-calcite grains increases from the dolomite reaction rim towards the pure calcite starting material (**Figure 2.3 a**). The grains often show curved grain boundaries with equilibrium angles at triple junctions. The platinum marker experiments indicate that the original interface between the reactants is located between dolomite palisades and granular dolomite (**Figure 2.3 b**).

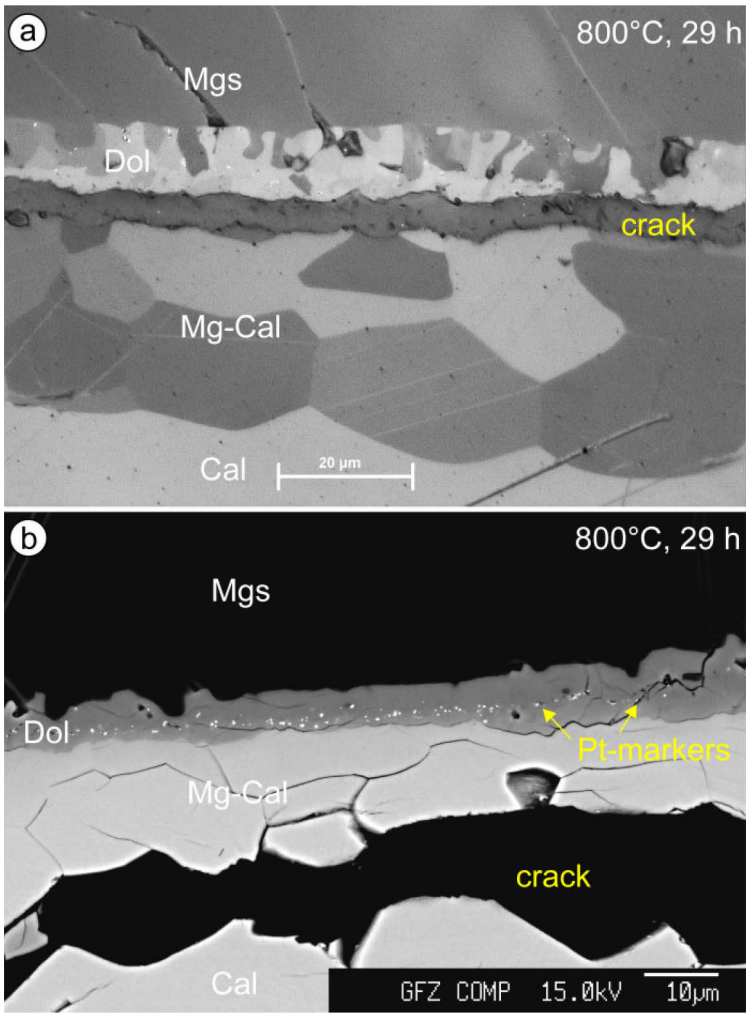

Figure 2.3 Pt-marker experiment CaMg-14, annealed at 800 °C and 29 h run duration. (**a**) Optical micrograph of polycrystalline dolomite and magnesio-calcite layers between magnesite and calcite single crystals. The dolomite rim consists of palisades oriented perpendicular to the interface with magnesite and of granular dolomite in contact to magnesio-calcite. (**b**) BSE image showing platinum markers (*white spots*), which indicate that the original calcite-magnesite interface is located at the boundary between the domains of the palisade-like and granular dolomite. Outliers are attributed to dolomite grain growth during annealing. Open cracks between interfaces are expected to evolve during cooling and sample preparation.

2.4.2 Kinetics of reaction rim growth

Time series experiments were done at temperatures of 750 and 800 °C by varying the annealing time between 3 and 146 hours. For determining the temperature dependence of the reaction kinetics, the temperature was varied between 750 and 850 °C at a fixed time of 74 hours. Generally, we find increasing rim thicknesses and grain sizes with increasing annealing time and temperature (**Table 2.2**). **Figure 2.4** shows rim thickness as a function of square root of time for all rim growth experiments. Both time series at temperatures of 750 °C and 800 °C reveal a linear increase of dolomite rim width with increasing square root of time, following a power law form of $\Delta x^2 = kt$ and consequently indicating diffusion-controlled rim growth

(JOESTEN 1977; ABART ET AL. 2009; JOACHIM ET AL. 2010). In comparison, at similar temperature and time the magnesio-calcite layer is thicker than the entire dolomite layer, whereas granular and elongated dolomite rims are approximately equal in width.

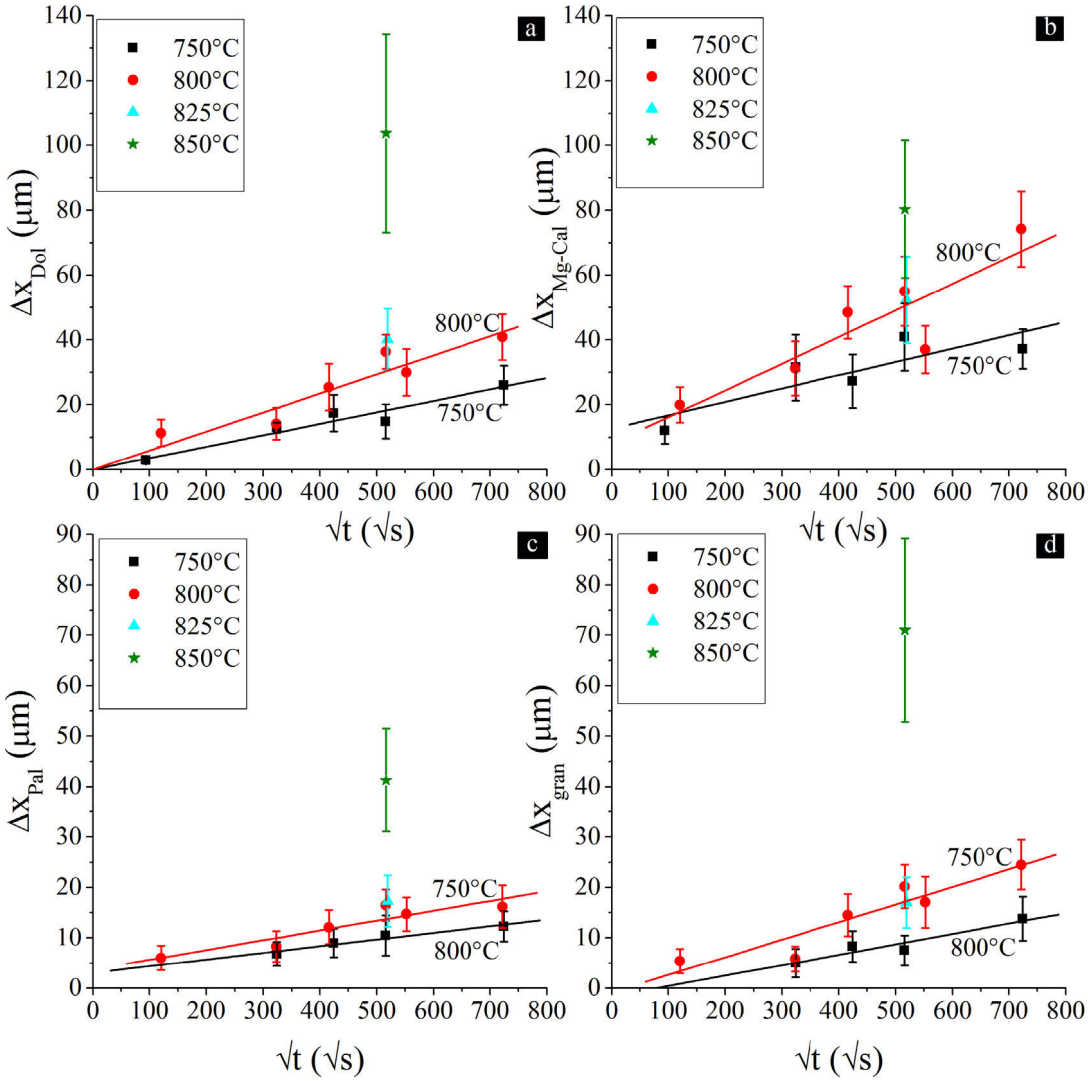

Figure 2.4 Reaction product layer width versus square root of time, linear relations are indicated for $T = 750°C$ (*black lines*) and 800 °C (*red lines*). (**a**) Total dolomite reaction rim width, (**b**) magnesio-calcite width, (**c**) dolomite palisades width, and (**d**) granular dolomite thickness. Error bars reflect the relatively large thickness variation (12-41%) along each profile of 7 mm length. Note different scales.

For example, for the time series performed at $T = 750$ °C, the average thickness of dolomite reaction rims varies between 2.9 and 26 µm and that of magnesio-calcite between 12.1 and 40.9 µm, respectively. At 800 °C the values range from 11.3 to 40.9 µm for the entire dolomite and 31.2 to 74.2 µm for the magnesio-calcite layer. The thicknesses of magnesio-calcite and dolomite palisades show a fast non-linear incipient stage (**Figure 2.4 b-c**), while granular dolomite growth is retarded (**Figure 2.4 d**). Afterwards the layer thicknesses increase linearly

with the square root of time following a parabolic growth behavior. Grain coarsening of dolomite palisades, granular dolomite and magnesio-calcite takes place during the experiments. Palisades and granular dolomite grain sizes increase by a factor of 1.5-1.8 at 750 °C and 1.5-1.6 at 800 °C during run durations between 29 and 145 hours (**Table 2.2**). In the same time span, the average magnesio-calcite grains coarsen about a factor of 1.4 and 1.7 (**Table 2.2**).

The different slopes of the regression lines for T = 750 °C and 800 °C shown in **Figure 2.4** indicate that the temperature sensitivity of rim growth is lowest for dolomite palisades and highest for magnesio-calcite. Extending the temperature range to 850 °C suggests that at a constant annealing time of 74 h the ratio of $\Delta x_{Dol}/\Delta x_{Mg-Cal}$ increases with T and exceeds 1 at about 840 °C (**Figure 2.5**). In contrast, the ratio of $\Delta x_{Pal}/\Delta x_{gran}$ decreases with temperature from 1.4 to 0.58 (**Figure 2.5 b**), suggesting a lower temperature sensitivity for growth of dolomite palisades than of granular dolomite.

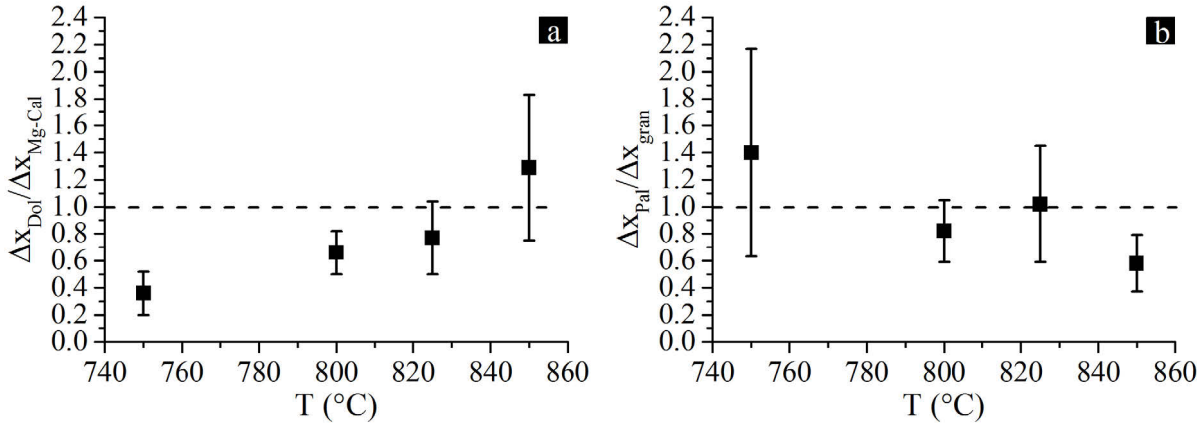

Figure 2.5 (**a**) Dolomite rim/magnesio-calcite thickness ratio versus temperature. The thickness ratio increase with increasing temperature. (**b**) Dolomite palisades/granular dolomite thickness ratio versus temperature. The thickness ratio tends to decrease with increasing temperature.

2.4.3 Texture analyses

Detailed crystallographic orientation maps were measured in 9 selected samples including the orientation of calcite and magnesite single crystals, polycrystalline dolomite (palisade and granular shapes) and polycrystalline magnesio-calcite. A typical orientation map and pole figures are presented in **Figure 2.6**, using the inverse pole figure color coding (see inset for details). The orientations of calcite and magnesite starting material single crystals are constrained by the orientation of one of the three $\{10\bar{1}4\}$ poles parallel to the growing direction (GD), since one of the three symmetric rhomb planes was parallel to the initial reaction inter-

face (**Figure 2.6 a**). The resulting bulk texture for dolomite shows [0001] axes for both palisades and granular dolomite concentrated in a position normal to the GD, with secondary concentrations (principally for the palisades) spreading all over the pole figures (**Figure 2.6 a**). The poles of $\{2\bar{1}\bar{1}0\}$ prismatic planes are distributed in a more complex form with no clear relation between maximum concentrations and external reference frame. The poles of $\{10\bar{1}0\}$ prismatic planes on the other hand form broad girdles normal to the reaction interface with weak maxima parallel to GD. The $\{10\bar{1}4\}$ rhombs are also distributed in a complex way, and the maxima of these poles tend to lie within the reaction interface plane (**Figure 2.6 a**). In contrast, magnesio-calcite forms [0001] axes subparallel or oblique to GD, poles of $\{2\bar{1}\bar{1}0\}$ and $\{10\bar{1}0\}$ form broad girdles subparallel to the reaction interface, and poles to $\{10\bar{1}4\}$ form small circles around the growing direction axis (**Figure 2.6 a**). Although the dolomite orientations show considerable scattering, the bulk texture still indicates some crystallographic orientation relationship to magnesite but primarily to calcite single crystals (see labels **1-6** in **Figure 2.6 a**). Detailed analysis of EBSD data revealed the presence of dolomite growth twins characterized by a rotation of 180° around one of the three equivalent a-axes ($[11\bar{2}0]$ twin axis). The twin grain boundaries represent between 25 and 40% of dolomite-dolomite boundaries in all the analyzed samples (see *black lines* decorating the twin boundaries in the EBSD map and histogram of misorientation in **Figure 2.6 a**). Although the twin grains occur within granular and palisades parts of the dolomite rim, the proportion of twin grains prevails in granular dolomite. Furthermore a topotactic relationship, where all crystallographic directions of dolomite are fixed with respect to the calcite single crystal, could be observed in all samples (e.g., **Figure 2.6 b**). These topotactic grains often appear equiaxed in shape and are characterized by the above-described twin relationship. Even within the magnesio-calcite layer, grains with the topotactic relationship to the calcite single crystal are present in most analyzed samples (e.g., **Figure 2.6 b**). The dolomite bulk texture diagrams (**Figure 2.6 a**) indicate axiotactic (only one crystallographic direction parallel) relationships of dolomite $\{2\bar{1}\bar{1}0\}$ and $\{10\bar{1}0\}$ axes to both calcite and magnesite single crystals (labeled **2, 5** and **6** in **Figure 2.6 a**). Furthermore, weak axiotactic relationship of rhombohedral crystallographic directions in dolomite to single crystal calcite may be suspected from the dolomite bulk texture diagrams (labeled **3** and **4** in **Figure 2.6 a**).

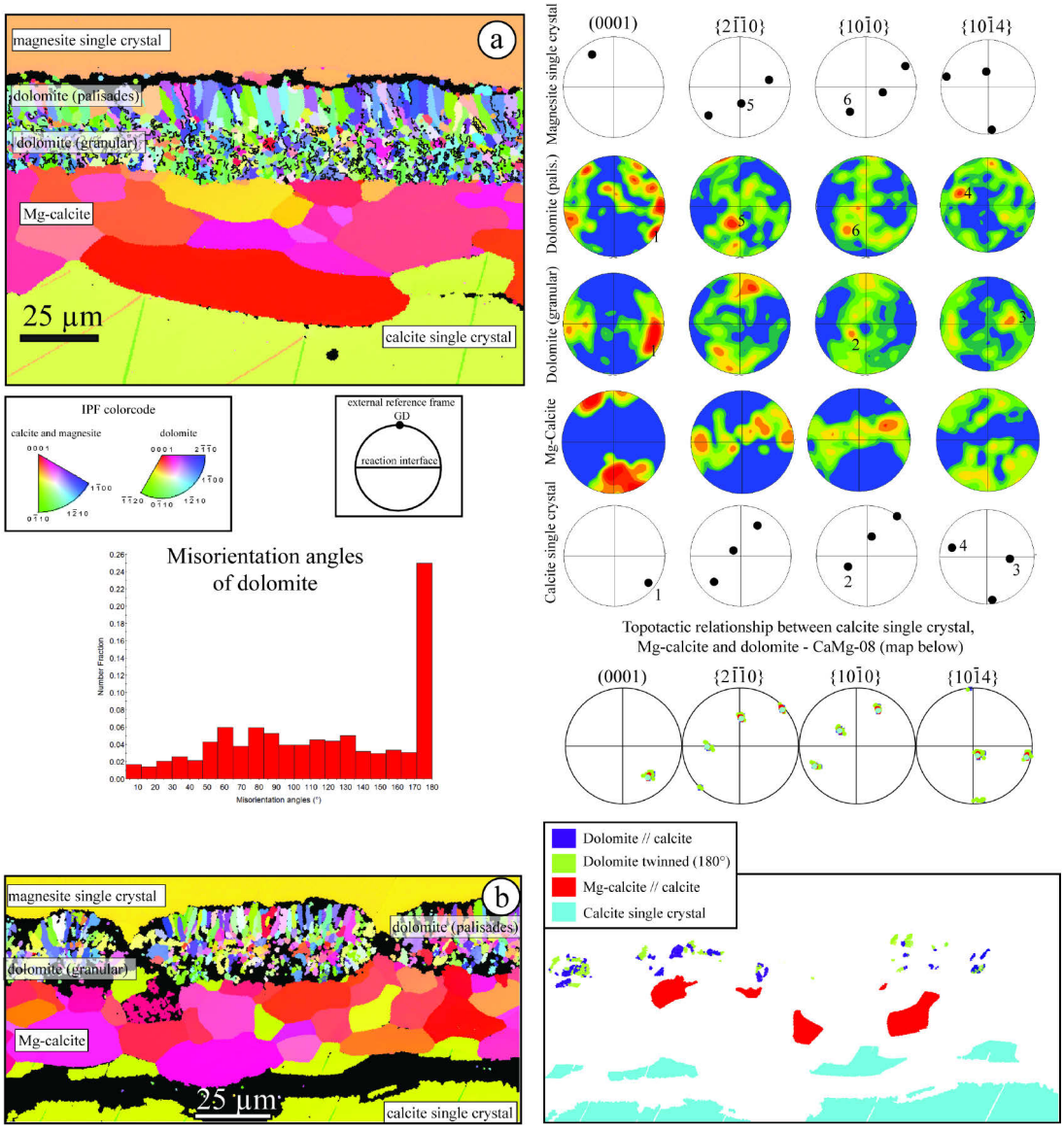

Figure 2.6 (**a**) EBSD inverse pole figure (IPF) color-coded map of sample CaMg-05 (146 h, 750 °C), showing the orientation of magnesite and calcite single crystals, polycrystalline dolomite (palisades and granular shapes) and magnesio-calcite. IPF color-code indicates the orientation of reference axes parallel to the growing direction (GD). For example, *red* or *light blue* grains have the $[1\bar{2}10]/[0001]$ or $[1\bar{2}10]$ axis pointing to the reader (note different colors for different phases). *Black lines* within dolomite rim highlight the twin relationship between neighboring dolomite grains. The histogram below shows the correlated misorientation angles of dolomite indicating that 26% of all dolomite-dolomite boundaries are represented by twin boundaries. Pole figures for $[0001]$ axes, poles to prismatic $\{2\bar{1}\bar{1}0\}/\{10\bar{1}0\}$ and rhomb $\{10\bar{1}4\}$ planes are plotted with respect to the external reference frame. The reference frame is defined by E-W plane, which represents the reaction rim interface and GD of the rim which is oriented N-S. The numbers on the pole figures indicate individual orientation relationships between calcite single crystal and dolomite (**1-4**) and magnesite and dolomite (**5-6**). All pole figures are equal-area projections (lower hemisphere) with a Gaussian half-width of 10° and a confidence index (CI) >0.2. Contour color densities are drawn based on multiples of random distribution with a factor of 9 from blue to red. (**b**) EBSD inverse pole figure color-coded map of sample CaMg-08 (48 h, 800 °C), which best documents the topotactic relations to single crystal calcite reactant. The map on the right shows grains of dolomite (*dark blue*) and magnesio-calcite (*red*) with topotactic relations to calcite (*light blue*) demonstrated in the pole figures. The *light green* grains in the topotaxy map represent the twinned dolomite grains in relation to the *dark blue* ones that show the topotactic relationships described before.

2.4.4 Microprobe analyses

Compositional line scans were performed from one reactant to the other across the dolomite rim and magnesio-calcite layer to measure chemical profiles (**Figure 2.7**). While the composition of the reactant phases is homogenous and flat also adjacent to the reaction rims, composition gradients occur within the newly evolved magnesio-calcite and dolomite rims. The dolomite is close to stoichiometric at the dolomite-magnesite interface, and it becomes successively more non-stoichiometric with increasing Mg deficiency towards the dolomite-calcite interface. According to the phase diagram in **Figure 2.2**, dolomite in equilibrium with magnesio-calcite at 800 °C should have a composition with about 47 mol% $MgCO_3$component and a dolomite in equilibrium with magnesite should have about 51 mol% $MgCO_3$ component. The composition of dolomite at the dolomite-magnesite interface thus closely corresponds to local equilibrium. In contrast, the dolomite is more calcium-rich and the magnesio-calcite is somewhat more Mg-rich than what is expected for local equilibrium at the calcite-dolomite interface. The processes underlying this deviation from local equilibrium are not known. A possible explanation could be the three dimensional character of the microstructures, which would especially influence analyses at phase boundaries, or the effect of nucleation and interface-reaction at the initial stage of rim growth, which appears to be fast for dolomite palisades (**Figure 2.4 c-d**). Alternatively, the depletion of Mg in granular dolomite due to the preceding magnesio-calcite formation may induce local disequilibrium in granular dolomite. The effect of deviations from local equilibrium element partitioning on the overall reaction kinetics are considered as minor and this complication has not been accounted for in our thermodynamic model.

Magnesio-calcite always shows a curved profile with progressively decreasing Mg content from granular dolomite towards calcite. Measurements on 10 samples at different run durations and temperatures reveal two different CaO and MgO distributions in dolomite, illustrated in **Figure 2.7**. At T = 850 °C, the dolomite palisades are nearly stoichiometric. The granular dolomite is substantially more Ca-rich and is clearly non stoichiometric with respect to its Ca/Mg ratio towards the contact with magnesio-calcite (**Figure 2.7 a**). At T = 825 °C, the molar concentrations of CaO and MgO are similar at the initial interface (dashed line in **Figure 2.7 b**). Chemical profiles of the other samples show the same two trends, but no systematic variation with annealing time or temperature.

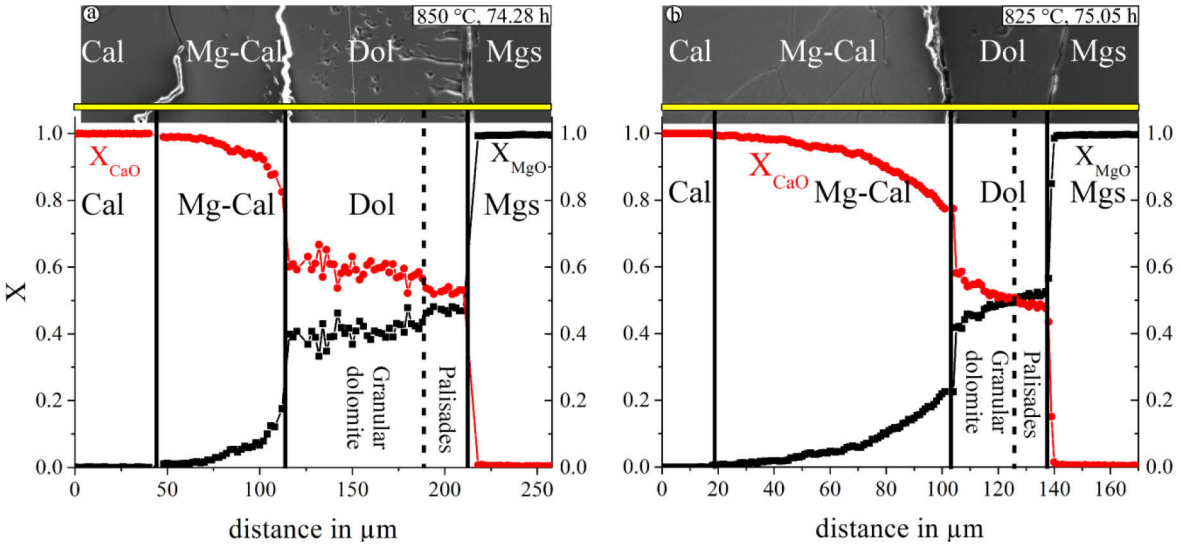

Figure 2.7 Chemical profiles in (**a**) sample CaMg-10 (t = 74.28 h, T = 850 °C) and (**b**) sample CaMg-13 (*t* = 75.05 h, *T* = 825 °C). The mole fractions of calcium (X_{CaO}) and magnesium (X_{MgO}) are shown in *red* and *black*, respectively. *Solid vertical lines* indicate locations of phase boundaries while the *dashed line* indicates the original interface.

2.5 Discussion

2.5.1 Microstructure and texture evolution

Initial reaction phase during experiments is associated with the formation of magnesio-calcite (**Figure 2.2**), which grew towards the calcite single crystal. This initial re-equilibration is assumed to affect the reaction interface, so that dolomite formed in between single crystal magnesite and polycrystalline magnesio-calcite. Such setup is probably responsible for the development of the two distinct dolomite regions. Granular dolomite encountered boundaries of already existing magnesio-calcite grains, while palisades could grow into the magnesite single crystal. The elongated shape of dolomite in contact with magnesite is suggested to be a stress-induced phenomenon resulting from a positive volume change at the dolomite-magnesite reaction interface (MILKE AND WIRTH 2003). Although, the overall reaction is more or less balanced regarding the volume change, the partial reaction at the magnesite-dolomite interface implicates a positive volume change, while the incorporation of magnesium in calcite results in a negative volume change. Since magnesio-calcite results from magnesium incorporation into calcite, it is likely that magnesio-calcite grains may inherit the crystallographic orientation of pure calcite. Indeed, some of the magnesio-calcite grains show a full crystallographic relation to calcite, which is then transferred also into dolomite (**Figure 2.6 b**). The relatively large size of the magnesio-calcite grains implies few nuclea-

tion sites, possibly because of the small composition contrast across the magnesio-calcite/calcite interface (**Figure 2.7**). The dolomite grains with topotaxy to calcite reactant occur mainly in the granular part of the rim or near the original reaction interface. They are characterized by a slightly larger grain size than the average and their spatial occurrence usually coincide with slightly thinner rim portions (**Figure 2.6 b**). This correlation may be explained by a slightly hindered grain boundary diffusion and nucleation during the initial phases of the rim growth in topotactic domains.

2.5.2 Diffusion components

The parabolic growth behavior of the dolomite reaction rim suggests that diffusion of Mg and/or Ca components was rate limiting (**Figure 2.4 a**; FISHER 1978). The term component is used here as a mere chemical entity that suffices to describe the chemical variation in the system of interest. It does not necessarily correspond to the composition of a phase or species. Within a single crystal of dolomite mass transfer may occur via interdiffusion of Mg^{2+} and Ca^{2+} ions. In this case, the cation fluxes are forced to be equal and directed in opposite directions due to the charge-balance constraint. Alternatively, Mg^{2+} and Ca^{2+} may diffuse coupled with O^{2-}, which would make Ca- and Mg-fluxes independent. Such behavior is probably enhanced through the presence of lattice imperfections such as edge dislocations and, more importantly, of grain boundaries, which could act as sources and sinks of vacancies. In case of a fine-grained polycrystalline reaction rim the coupled diffusion of divalent cations and oxygen is thus conceivable. Based on experiments in the $MgO\text{-}SiO_2$ system (GARDÉS AND HEINRICH 2011) and in the $CaO\text{-}MgO\text{-}SiO_2$ system (JOACHIM ET AL. 2010), which were both conducted under ”dry” conditions, coupled diffusion of Mg^{2+} and O^{2-} could indeed be demonstrated. During growth of a polycrystalline dolomite reaction rim in the two component system $MgCO_3\text{-}CaCO_3$ the diffusion fluxes of the two components may be independent.

In our study, we do not consider transfer of carbonate. It is thus sufficient to consider MgO and CaO as the two mobile components. Although the speciation of the diffusing matter is not known, the bulk effect of its transfer can be descried in terms of the MgO and CaO components. If the Mg and the Ca–bearing species indeed diffuse independently, the rim growth rate depends on the mobilities of both components. The relative fluxes of the two components can be inferred from the position of the original calcite-magnesite interface (ABART ET AL. 2004). The off-center position of the original calcite-magnesite interface as

indicated by the platinum markers (**Figure 2.3**), suggests that the diffusive fluxes of the two components were different.

2.5.3 Dolomite rim growth model

The overall reaction (**eq. 2.1**) can be split into two partial reactions, taking place at the dolomite-calcite (**eq. 2.2**) magnesite-dolomite (**eq**. **2.3**) and the interface:

Interface I:
$$\mathrm{CaCO_{3,solid}} + v\ \mathrm{MgCO_{3,mobile}} = v\ \mathrm{CaMg(CO_3)_{2,solid}} + (1-v)\mathrm{MgCO_{3,mobile}} \quad \textbf{(2.2)}$$

Interface II:
$$\mathrm{MgCO_{3,solid}} + (1-v)\mathrm{CaCO_{3,mobile}} = (1-v)\ \mathrm{CaMg(CO_3)_{2,solid}} + v\ \mathrm{MgCO_{3,mobile}} \quad \textbf{(2.3)}$$

where v is the molar amount of MgO forming granular dolomite at the calcite-dolomite interface and (1-v) is the molar amount of CaO producing dolomite palisades from magnesite at the dolomite-magnesite interface. In **Figure 2.8** the geometry of the rim growth setting and the associated component fluxes are illustrated schematically.

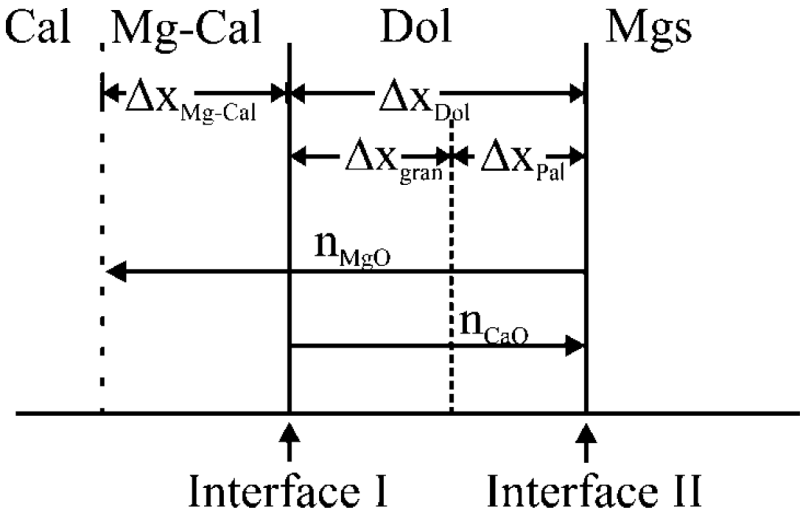

Figure 2.8 Schematic drawing of the growth of dolomite and magnesio-calcite at a calcite-magnesite contact in planar geometry (adopted from ABART ET AL. 2009). The decomposition of magnesite at *interface I* provides mobile MgO, and the decomposition of calcite at *interface II* provides mobile CaO. The *dashed line* within the dolomite layer represents the boundary between dolomite palisades and granular dolomite, i.e. the position of the initial interface between the reactant phases.

Within the dolomite rim the domains with the palisade and the granular microstructures are discerned. Note that the flux of CaO is restricted to the rim of newly formed dolomite; in contrast a fraction of the MgO that is derived from the consumption of the magnesite at the do-

lomite-magnesite interface diffuses across the dolomite-calcite interface and into the calcite forming magnesio-calcite. The fraction v is related to the molar amount (n) of components that are transferred during reaction rim growth

$$v = \frac{n_{MgO}}{n_{MgO} + n_{CaO}} \tag{2.4}$$

where n can be derived from the thickness of dolomite layers Δx_{pal} and Δx_{gran}, the molar volume $\bar{V}^{\gamma}$ of phase γ and the unit cross section$A$.

$$n_{CaO} = \frac{\Delta x_{pal}\, A}{\bar{V}^{dol}} \tag{2.5}$$

$$n_{MgO} = \frac{\Delta x_{gran}\, A}{\bar{V}^{dol}} + \frac{\Delta x_{Mg-Cal}\, c_T\, A}{\bar{V}^{Cal}} \tag{2.6}$$

The second term in equation (**eq. 2.6**) accounts for the formation of magnesio-calcite. The correction factor $c_T$represents the molar Mg concentration, which was determined from measured chemical profiles leading to average values of $c_{750,850} = 0.03$, $c_{800} = 0.04$ and $c_{825} = 0.06$ at T= 750 °C and 850 °C, 800 °C and 825 °C, respectively.

To determine the diffusion coefficients of CaO and MgO the thermodynamic model for diffusion controlled reaction rim growth in a binary system of ABART ET AL. (2009) with extension of GÖTZE ET AL. (2009) was used. This model is based on the assumption that the diffusion of chemical components across the dolomite reaction rim is the only dissipative process and that the potential contribution of dolomite nucleation to the total energy budget can be neglected. Rearrangement of equations 26, 34 and 36 from ABART ET AL. (2009) leads to the combined diffusion coefficient (D_{com}) which accounts for the simultaneous diffusion of both mobile components MgO and CaO:

$$D_{com} = R_g T \frac{\Delta x_{pal}^2 (1-u)}{2t\Delta G_{rim}} \frac{\left(X_{MgO}^{Mgs} X_{CaO}^{Dol} - X_{MgO}^{Dol} X_{CaO}^{Mgs}\right)^2}{(v-1)X_{MgO}^{Dol} - vX_{CaO}^{Dol}} \frac{V^{Dol}}{(V^{Mgs})^2} \frac{1}{X_{CaO}^{Dol} X_{MgO}^{Dol}} \tag{2.7}$$

where R_g is the gas constant, $V^{\gamma}$is the specific molar volume of phase γ, and $X_i^{\gamma}$is the mole fraction of component i in phase γ. The parameter u incorporates the mass balance at the reaction fronts and information of interface motions (ABART ET AL. 2009). Since the original model assumes stoichiometric composition of the reaction rim, we account for the measured

chemical gradient in dolomite **Figure 2.8** by using a modified expression for u using equations 14,15,17,18 and 21 of ABART ET AL. (2009), which leads to (GÖTZE ET AL. 2010):

$$u = 1 - \frac{V^{Dol}}{V^{Mag}}\left[\frac{v(1-2X_{CaO}^{Mgs}) - (1-X_{CaO}^{Mgs})}{v(1-2X_{CaO}^{Pal}) - (1-X_{CaO}^{Pal})} - \frac{\frac{-v(1-2X_{CaO}^{Cal}) + (1-X_{CaO}^{Cal})}{X_{CaO}^{Cal}X_{MgO}^{gran} - X_{MgO}^{Cal}X_{CaO}^{gran}}}{\frac{-v(1-2X_{CaO}^{Pal}) + (1-X_{CaO}^{Pal})}{X_{CaO}^{Mgs}X_{MgO}^{Pal} - X_{MgO}^{Mgs}X_{CaO}^{Pal}}}\right] \quad \textbf{(2.8)}$$

The mean mole fractions at the reaction fronts for a given temperature were determined from microprobe analysis. The Gibbs molar energy of rim formation (ΔG_{rim}) is defined by the ratio of the molar Gibbs free energy of the reaction ($\Delta_r G$) to the specific molar volume of magnesite (V^{Mgs}) (ABART ET AL. 2009; their equation 27):

$$\Delta G_{rim} = \frac{1}{V^{Mgs}}\Delta_r G \quad \textbf{(2.9)}$$

The thermodynamic data of the phases in our experiments used to calculate ΔG_{rim} are given in **Table 2.3**.

	Calcite	Magnesite	Dolomite
$\bar{V}$ (750 °C) [cm³/mol	37.56	28.72	65.84
$\bar{V}$ (800 °C) [cm³/mol]	37.63	28.79	65.98
$\bar{V}$ (825 °C) [cm³/mol]	37.67	28.82	66.05
$\bar{V}$ (850 °C) [cm³/mol]	37.79	28.85	66.13
$\Delta_f G$ (750 °C) [J/mol]	-1,235,207	-1,114,861	-2,354,6
$\Delta_f G$ (800 °C) [J/mol]	-1,246,520	-1,124,56	-2,375,712
$\Delta_f G$ (825 °C) [J/mol]	-1,252,291	-1,129,530	-2,386,457
$\Delta_f G$ (850 °C) [J/mol]	-1,258,138	-1,134,565	-2,397,349

Table 2.3 Molar volumes $\bar{V}$ and Gibbs free energies $\Delta_f G$ of formation of calcite, magnesite and dolomite at T = 750–850 °C and P_c = 400 MPa (from HOLLAND AND POWELL 1998).

The combined diffusion coefficient D_{com} can also be expressed by (ABART ET AL. 2009):

$$D_{com} = kD_{MgO} + (1-k)D_{CaO} \quad \textbf{(2.10)}$$

where k gives the proportion of the component fluxes within the dolomite reaction rim defined as

$$k = \frac{D_{MgO}}{D_{MgO} + D_{CaO}} \tag{2.11}$$

Combining equations (**eq. 2.10**) and (**eq. 2.11**) allows determining the individual component diffusivities:

$$D_{CaO} = D_{com}\frac{(1-k)}{(2k^2-2k+1)} \; and \; D_{MgO} = \frac{D_{com} - D_{CaO}(1-k)}{k} \tag{2.12}$$

The diffusion coefficients obtained from our rim growth experiments are shown in an Arrhenius diagram in **Figure 2.9**, following the relation:

$$D = k_0 e^{-\frac{E_a}{TR_g}} \tag{2.13}$$

with k_0(CaO) = $10^{-4.9 \pm 2.7}$ m²/s, E_a(CaO) = 192 ± 44 kJ/mol and k_0(MgO) = $10^{-4.5 \pm 2.2}$ m²/s, E_a(MgO) = 198 ± 54 kJ/mol respectively.

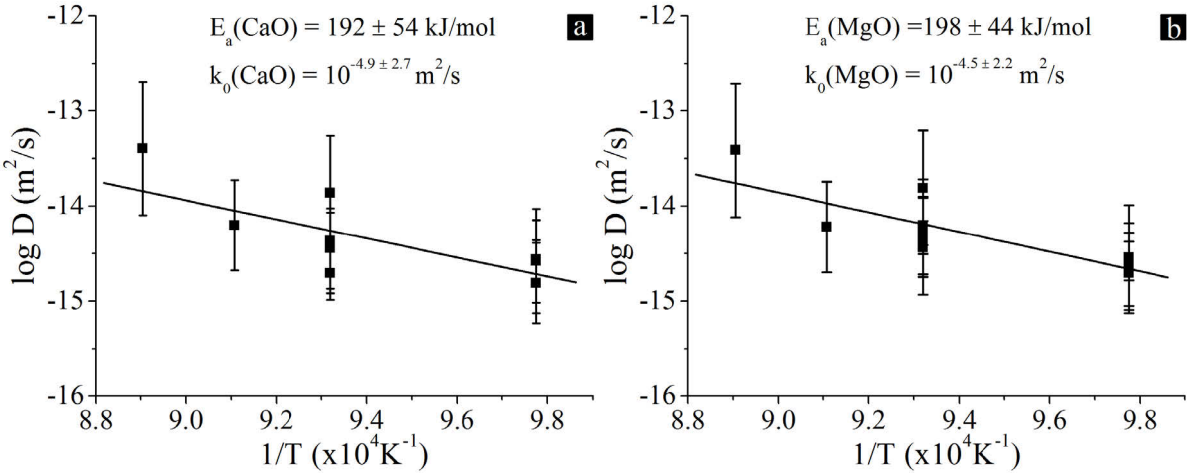

Figure 2.9 Arrhenius plot of the effective diffusion coefficients of (**a**) CaO and (**b**) MgO in dolomite in the range of 750–850 °C. Values are from **Table 2.2**.

Both components show almost identical temperature dependence of their diffusivities, which yields quite similar activation energies in the order of 200 kJ/mol for both components. Out of **Figure 2.5**, a huge difference in activation energies may have been expected due to the increasing or decreasing ratio of layer thicknesses with temperature. Indeed, if plotting the ratio of $\Delta x_{Pal}/(\Delta x_{gran}+\Delta x_{Mg-Cal})$ against time the ratio remains nearly constant between 0.22–0.27, implying similar activation energies for diffusing components.

It must be noted, that the diffusion coefficients refer to the self-diffusion of CaO and MgO in polycrystalline dolomite, where diffusion may occur by a combination of volume-

and grain-boundary diffusion. Diffusion coefficients obtained in this study should be regarded as effective diffusion coefficients. The relatively large size of magnesio-calcite grains compared to dolomite grains with magnesio-calcite grain boundaries oriented mainly perpendicular to the growth direction, and the measured chemical profile within magnesio-calcite may indicate dominantly volume diffusion. In contrast, abundant grain boundaries within the small granular dolomite with abundant twins and relatively straight grain boundaries of the dolomite palisades may suggest preferred grain boundary diffusion.

2.5.4 Comparison with other diffusion coefficients in carbonates

To the best of our knowledge only two studies determined component diffusion in dolomite so far. ANDERSON (1972) determined the self-diffusion coefficients of C and O in crushed dolomite using isotope exchange with CO_2 at T = 645–785 °C and P = 12-93.5 MPa. Diffusion rates of C and O in dolomite are nearly identical with activation energies of E_a(C) = 468 kJ/mol and E_a(O) = 485 kJ/mol (**Figure 2.10**).

MÜLLER, CHERNIAK, AND WATSON (2012) performed thin film experiments between dolomite and siderite or rhodochrosite to determine interdiffusion coefficients of (Mn, Fe) – Mg – Ca in the temperature range of 400–625 °C at 1 atm pressure. The authors determined coupled diffusion of Mn-(Ca+Mg) and Fe-(Ca+Mg) with activation energies of E_a(Mn-(Ca+Mg)) = 63 ± 5 kJ/mol and E_a(Fe-(Ca+Mg)) = 123 ± 10 kJ/mol respectively. The temperature dependence of the quasi-binary exchange of Mn-Mg and Fe-Mg shows a kink at T ~525 °C with an increase of activation energies from E_a(Mn-Mg) = 23 ± 4 kJ/mol to 168 ± 15 kJ/mol and from E_a(Fe-Mg) = 34 ± 10 kJ/mol to 183 ± 14 kJ/mol (**Figure 2.10**) in a low-temperature regime. A proposed explanation is an increased disorder of dolomite at high temperatures, rather than a transition from an extrinsic to an intrinsic diffusion regime (MÜLLER, CHERNIAK, AND WATSON 2012). When extrapolated to the temperatures of our experiments, the interdiffusion coefficients in the Ca, Mg and Ca, Mg, Mn, Fe-couples determined by MÜLLER, CHERNIAK, AND WATSON (2012) are several orders of magnitude lower than the diffusion coefficients we determined for the CaO and MgO components.

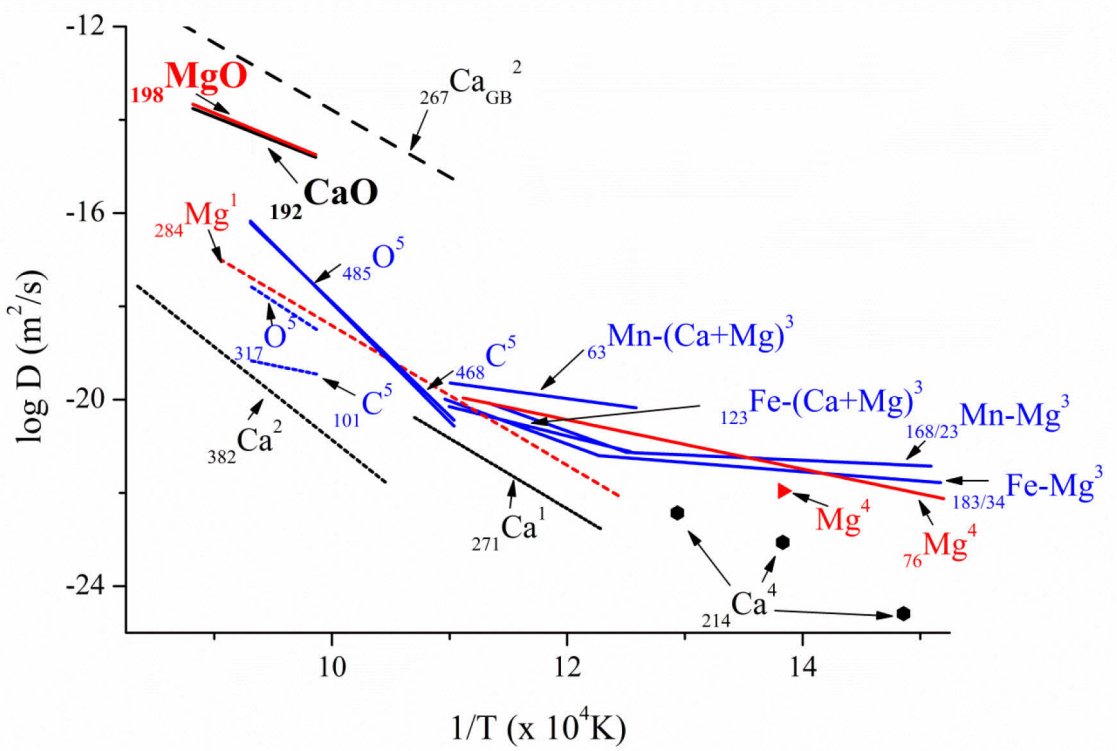

Figure 2.10 Arrhenius diagram for diffusion coefficients of various elements in calcite, magnesite and dolomite. Published data on diffusion in dolomite and calcite are plotted as *solid lines* and *dashed lines*, respectively. *Dots* and *triangles* represent chemical diffusion of Ca and Mg in magnesite, respectively. 1 = FISLER AND CYGAN (1999), 2 = FARVER AND YUND (1996), 3 = MÜLLER, CHERNIAK, AND WATSON (2012), 4 = KENT ET AL. (2001), 5 = ANDERSON (1972). *Indices* at the lower left of the chemical symbols represent activation energies in kJ/mol. All data are determined for volume diffusion, except those marked by *GB*, which represents grain boundary diffusion.

For comparison **Figure 2.10** also shows diffusion coefficients of Ca and Mg in calcite and magnesite. FARVER AND YUND (1996) determined activation energies for Ca volume and grain boundary diffusion in natural samples at P = 0.1 MPa and T = 650–900 °C of 382 ± 37 kJ/mol and 267 ± 47 kJ/mol, respectively. Assuming an effective grain boundary width of 3 nm, diffusion rates would be 6 orders of magnitude higher for diffusion along the grain boundaries than for volume diffusion. Besides, they conducted calcium self-diffusion experiments parallel to the c-axis and perpendicular to the natural cleavage planes of natural calcite single crystals to investigate the anisotropy of diffusion coefficients. Despite the trigonal crystal system there was no anisotropy measureable regarding Ca diffusion in calcite.

FISLER AND CYGAN (1999) measured Ca and Mg self-diffusion coefficients perpendicular to the rhomb plane in natural calcite single crystals. Experiments were performed at T = 550–800 °C and P = 0.1 MPa, for which activation energies were quite similar with E_a(Ca) = 271 ± 80 kJ/mol and E_a(Mg) = 284 ± 74 kJ/mol, although Mg self-diffusion appears to be one order of magnitude faster than Ca self-diffusion. Interestingly, the Ca-diffusivity measured by

FISLER AND CYGAN (1999) is one order of magnitude faster than measured by FARVER AND YUND (1996), which may be related to different amounts of Mg and Mn present in the used starting materials (FISLER AND CYGAN, 1999). KENT ET AL. (2001) investigated Mg chemical diffusion in calcite as well as Ca chemical diffusion and Mg self-diffusion in magnesite. Experiments were performed using fragments of natural cleaved material, calcite or magnesite, which were placed together with dried powder of MgO and $MgCO_3$ for calcite or $CaCO_3$ for magnesite into Pt-capsules. The material was pre-dried and subsequently sealed inside evacuated silica glass tubes for annealing experiments using a muffle furnace. Annealing conditions were between 400 and 600 °C at P = 0.1 MPa. For Mg chemical diffusion in calcite an activation energy of only E_a(Mg) = 76 ± 16 kJ/mol was determined, which may indicate a switch from intrinsic to extrinsic diffusion at low T. Chemical diffusion of Ca in magnesite yielded an activation energy of E_a(Ca) = 214 ± 60 kJ/mol. The measured self-diffusion coefficient of Mg in magnesite at 450 °C is similar to Mg chemical diffusion in calcite. These values are higher than those obtained for diffusion of CaO and MgO in our study (E_a(CaO) =192 ± 54 kJ/mol, E_a(MgO) = 198 ± 44 kJ/mol), but overlap within error bars at least for MgO. The associated diffusivities for calcium, magnesium and oxygen volume diffusion in calcite are 3 to 5 orders of magnitude lower than those estimated for dolomite (**Figure 2.10**). FARVER AND YUND (1996) measured also the grain boundary diffusion of calcium in natural and hot-pressed calcite aggregates, yielding an activation energy of $E_{a,GB}$(Ca) = 267 ± 47 kJ/mol. Assuming a grain boundary width of 1 nm, FARVER AND YUND (1996) obtained a Ca grain-boundary diffusivity in calcite that is about two orders of magnitude faster than the component diffusivities in dolomite measured in our study (**Figure 2.10**). Although differences in the calculated diffusivities may arise from the applied experimental techniques, comparison of all of these diffusion data does not clearly demonstrate whether volume or grain boundary predominates in our dolomite rim growth experiments.

2.6 Conclusions

Annealing experiments on calcite and magnesite single crystals produced a magnesio-calcite layer and a polycrystalline dolomite reaction rim at temperatures between 750 and 850 °C and 400 MPa confining pressure. Within dolomite, two different microstructural domains formed. Stress-induced palisades grew perpendicular to the interface on magnesite and granular dolomite formed on magnesio-calcite. Platinum markers showed that this microstructural boundary represents the original calcite-magnesite interface. Chemical composition of palisades is nearly stoichiometric, while the granular portions show a slight gradient diverging toward magnesio-calcite. All reaction domains, magnesio-calcite, palisades and granular dolomite show a crystallographic orientation relationship to the calcite reactant. Full crystallographic relationships with respect to calcite are restricted to magnesio-calcite and granular dolomite. Axiotactic dolomite grains also appear in the palisade domain, associated with randomly distributed growth twins. The entire dolomite rim thickness increases linearly with the square root of time, indicating a diffusion-controlled mass transport. Thermodynamic considerations lead to activation energies of E_a(CaO) = 192 ± 54 kJ/mol and E_a(MgO) = 198 ± 44 kJ/mol.

2.7 Acknowledgments

We are grateful to S. Gehrmann for sample preparation, M. Naumann for technical support with the Paterson apparatus and W. Heinrich for fruitful discussions. Two anonymous reviewers are thanked for their insightful comments. This work was funded by the Deutsche Forschungsgemeinschaft within the framework of FOR 741, project RY 103/1-1, which is gratefully acknowledged.

3 Influence of stress and strain on dolomite rim growth: a comparative study

3.1 Abstract

Triaxial compression and torsion experiments were performed to investigate the influence of non-isostatic stress and strain on dolomite reaction rim growth using orientated natural calcite and magnesite single crystals at a temperature of 750 °C, 400 MPa confining pressure, stresses between 7 and 38 MPa and test durations up to 171 hours. Reaction products were composed of a polycrystalline magnesio-calcite layer, palisade-shaped dolomite and granular dolomite grains. In all experiments, inelastic deformation was partitioned into calcite and reaction products, while magnesite remained undeformed. Calcite deformed by twinning and dislocation creep, where the activation of additional glide systems at high stress allowed high strain. Depending on grain size, magnesio-calcite deformed by diffusion creep and/or grain boundary sliding, twinning and dislocation creep. Dolomite deformed mainly by diffusion creep, assisted by enhanced dislocation activity allowing Ca enrichment in the granular rim. A weak crystallographic preferred orientation of the reaction products was observed. In triaxial compression, dolomite rim growth was diffusion-controlled and showed no influence of axial stresses up to 38 MPa on the reaction kinetics. At high strain (>0.1), the magnesio-calcite layer is wider suggesting faster growth kinetics. This may be related to additional diffusion pathways provided by enhanced dislocation activity. At very high strain (>0.3-0.6) twisted samples showed a gradual decrease in layer thickness of dolomite and magnesio-calcite with increasing strain (-rate).

3.2 Introduction

Stress-induced deformation and mineral reactions are processes that often occur simultaneously in the Earth's crust. The interaction of these processes may for example induce localized deformation and formation of shear zones by neocrystallization and/or dehydration as frequently reported in literature (e.g., KERRICH ET AL. 1980; RUBIE 1983; BRODIE AND RUTTER 1985; STÜNITZ 1998; NEWMAN ET AL. 1999; KENKMANN AND DRESEN 2002; WHITMEYER AND WINTSCH 2005 and reference therein). However, so far little is known about the influence of

stress and strain on the reaction kinetics. Deformation may enhance mineral reactions via local changes in the density of crystal defects and a reduction of inelastic strain energy, an increase of chemical potential gradients, or by modifications of the microstructure (e.g., BRODIE AND RUTTER 1985). Thermodynamic considerations show that the elastic and plastic strain energy associated with deformation does not significantly change the total Gibbs free energy of a mineral reaction, so that the driving force is not influenced noticeably (KELLER ET AL. 2010). Instead, deformation-induced defects may considerably change diffusion-controlled reaction rates, for example by fast diffusion along dislocation cores, redistribution or formation of new (sub-) grain boundaries, or changes in the texture that influence the diffusivity along specific grain boundaries.

A number of recent experimental studies provide evidence for deformation-enhanced metamorphic reactions in various polycrystalline systems, for example in feldspar-olivine (DE RONDE ET AL. 2004; DE RONDE ET AL. 2005; DE RONDE AND STÜNITZ 2007), periclase-ferropericlase (HEIDELBACH ET AL. 2009) and calcite-dolomite (DELLE PIANE, BURLINI, AND GROBETY 2007; DELLE PIANE, BURLINI, AND KUNZE 2009). Compared to isostatic conditions, reaction rates were up to 3 times faster, likely associated with grain size reduction and grain boundary migration at high strain.

More recently, GÖTZE ET AL. (2010) and KELLER ET AL. (2010) investigated the influence of non-hydrostatic stress on reaction rates within the system MgO-Al_2O_3-SiO_2 in the temperature range of 1150 to 1350 °C and at ambient confining pressure. GÖTZE ET AL. (2010) performed sandwich annealing experiments in the subsystems MgO-SiO_2 and MgO-Al_2O_3 using synthetic single crystals (quartz, forsterite, periclase) and polycrystals (corundum) as well as natural single crystals (quartz, San Carlos olivine) and polycrystals (novaculite) as starting materials. Natural starting materials were found to be more reactive than synthetic crystals, possibly attributed to their higher initial dislocation density and a high amount of structurally bonded water. At T = 1250 °C and a run duration of t = 44.5 h, the average thickness of orthopyroxene rims between natural olivine and novaculite increased by about 45% by an increase of stress from σ = 1.2 MPa to σ = 24 MPa. In contrast, double rims of forsterite-enstatite growing between periclase and quartz decreased in thickness by about 39% if stress is increased from 2.9 to 29 MPa at 1350 °C and 72 h run duration, whereby the volume proportion of forsterite decreases from 87 to 64 vol.%. Even if the phenomenon is not fully understood yet, volume changes at the reaction interfaces are assumed to be responsible for the observed change of rim reaction rates with stress. Within the subsystem Al_2O_3-MgO, diffu-

sion-controlled spinel reaction rim growth between (polycrystalline) corundum and periclase single crystals were hardly influenced by applied axial stress between 3 and 30 MPa (KELLER ET AL. 2010). However, using orientated single crystals of sapphire as starting materials instead, spinel rim growth exhibited a fourfold increase in total rim thickness at similar temperature-time conditions. The authors showed that a stress-induced change in texture and microstructure is likely responsible for the different behaviors. At low stress, large spinel palisades grew epitactically with sapphire, i.e., azimuthally oriented with respect to the substrate structure, and rotated out of epitaxy at higher stresses. Contrarily, small spinel grains in contact with periclase exclusively grew epitactic at both, low and high stresses. Therefore, rearrangement of (sub-) grain boundaries with increasing stress at the interface with sapphire probably led to faster diffusion pathways and enhanced reaction rates (KELLER ET AL. 2010).

Here, we focus on the $CaCO_3$-$MgCO_3$ system since carbonates are of great geological interest with calcite ($CaCO_3$) and dolomite ($CaMg[CO_3]_2$) often found in crustal shear zones and magnesite ($MgCO_3$) occurring in subduction zones and ultrahigh pressure metamorphic terranes (HOLYOKE, KRONENBERG, AND NEWMAN 2013; HOLYOKE ET AL. 2014). In a previous study (HELPA ET AL. 2014) we investigated diffusion-controlled dolomite reaction rim growth at the contacts of oriented calcite and magnesite single crystals at isostatic conditions of pressure P_c = 400 MPa, T = 750–850 °C and t = 3-146 hours. Polycrystalline dolomite reaction rims showed a palisade-like microstructure in contact with magnesite and granular grains in contact with calcite. In between the granular dolomite and the calcite reactant, large magnesio-calcite grains evolved due to the incorporation of magnesium into the calcite reactant. All reaction products showed at least an axiotactic (one crystallographic direction parallel) relation or even a topotactic (all crystallographic directions are parallel) relation to the calcite single crystal.

In this subsequent study we investigate the impact of stress/strain on dolomite rim growth between calcite and magnesite single crystals at similar P-T conditions in triaxial and torsion experiments, combined with detailed microstructural, chemical and texture analysis. We used single crystal starting materials to allow direct comparison to isostatic rim growth experiments and to evaluate the potential effect of deformation-induced textural changes on reaction rates.

3.3 Starting materials and experimental methods

3.3.1 Starting materials and sample preparation

The experiments were conducted using natural, optically clear calcite (Brasil, Minas Gerais) and magnesite (Brasil, Bahia Brumado) single crystals. Chemical compositions of starting materials were obtained using a field emission gun electron microprobe (JEOL JXA-8500 F HYPERPOBE) at 15 keV accelerating voltage, 10 nA beam current and 15 µm beam diameter with a counting time of 60 s on peak and 30 s for the background. Within one single crystal 5 different locations were measured to ensure reliable results. Results verify relatively pure calcite with trace amounts of Ba, while magnesite contains on average 0.18 ± 0.02 wt.% impurities of calcium and trace amounts of Fe (**Table 3.1**).

For deformation tests on calcite and magnesite single crystals, cylindrical samples of 7 mm in diameter and 2.7 to 6.3 mm in length were cored perpendicular to the natural cleavages of crystal rhombohedra and subsequently polished. Test assemblies consist of calcite-magnesite stacks attached to alumina spacers above and below each sandwich. The whole assembly of was jacketed in copper sleeves with ≈8.3 mm outer diameter. After deformation, the jacketed samples were cut longitudinally along the cylinder axis to investigate the reaction products between single crystals. For twisted samples, additional longitudinal tangential sections (TG) were prepared close to the cylinder surface (PATERSON AND OLGAARD 2000).

	Calcite ± 1σ	**Magnesite ± 1σ**
MgO	0.01 ± 0.00	48.94 ± 1.19
FeO	0.00 ± 0.00	0.10 ± 0.08
CaO	55.79 ± 0.15	0.18 ± 0.02
SrO	0.02 ± 0.00	0.00 ± 0.00
MnO	0.00 ± 0.01	0.02 ± 0.02
TiO_2	0.02 ± 0.02	0.01 ± 0.01
SiO_2	0.01 ± 0.01	0.01 ± 0.01
BaO	0.06 ± 0.04	0.04 ± 0.04
SO_3	0.00 ± 0.00	0.00 ± 0.00
CO_2	44.08 ± 0.18	50.68 ± 1.31

Table 3.1 Composition of starting materials. Values (in wt.%) represent mean data based on five-point analyses of 16 reactants. CO_2 contents were calculated assuming an oxide total of 100%.

3.3.2 Analytical techniques

Investigations of single crystal reactants and reaction products were done using optical and electron microscopy. Rim thickness, microstructures and grain sizes were evaluated using an optical microscope (Leica DM RX) with an attached high-resolution digital camera (Leica DFC 420). A set of reflected-light pictures was taken along the complete initial interface line and analyzed by digitizing phase and microstructural boundaries. The grain widths were measured for 50 grains within individual reaction products and averaged. For detailed microstructure analysis of selected areas with different stress-strain conditions, grain boundary maps were manually drawn and subsequently digitized. The area (A), perimeter (P), minor (n) and major axis (m) length of each grain was calculated using an open source image analysis program (Image J; http://imagej.nih.gov/ij/). A grain boundary correction was done to account for the thickness of the redrawn segment lines (f), yielding the corrected area ($\tilde{A}$), the circle-equivalent diameter ($\tilde{a}$), the corrected axes length ($\tilde{m}, \tilde{n}$) and aspect ratio (AR) of each grain using:

$$\tilde{A} = A + f\left(\frac{P}{2} + f\right);\ \tilde{a} = \sqrt{\tilde{A}\frac{4}{\pi}};\ \tilde{m} = m + f;\ \tilde{n} = n + f;\ AR = \frac{\tilde{m}}{\tilde{n}} \qquad \textbf{(3.1)}$$

Using an electron microprobe, chemical composition line scans were performed across the reaction products from one reactant to the other via wavelength dispersive X-ray (WDS) analysis. Only major elements Ca (Kα, PETJ) and Mg (Kα, TAP) were measured applying an accelerating voltage of 15 kV, a beam current of 2 nA, a beam diameter of 2 µm and a step size of 2 µm. Counting time at every point was 20 s for the peak and 5 s for the background.

Crystallographic orientations of reactants and products were analyzed using a dual-beam scanning electron microscope (FEI Quanta 3d FEG SEM-FIB). A combination of electron backscatter diffraction (EBSD, TSL DigiView) and semi-quantitative energy dispersive spectroscopy (EDS) was used for investigations, which allowed unambiguous identification of the phases. Details of operating conditions and evaluating procedures are described by HELPA ET AL. (2014). Transmission electron microscopy (TEM) examinations were done using a Tecnai™G2 F20 X-twin microscope equipped with a field emission gun (FEG). Investigated foils were cut via focused ion beam (FIB) technique (FEI FIB 200 TEM) parallel to the cylindrical axis and perpendicular to the reaction interface with the dimension 15 x 10 x 0.15 µm.

3.3.3 Deformation experiments

Triaxial compression and torsion tests were performed using a Paterson-type gas-deformation apparatus (PATERSON 1970; PATERSON AND OLGAARD 2000) at fixed temperature of 750 °C and confining pressure of 400 MPa. Tests were performed as creep tests at constant load or at constant twist rate (**Table 3.2**).

Experiment	Test	T (K)	t (h)	Strain	Strain rate (s^{-1})	Stress (MPa)
Triaxial				ε	$\dot{\varepsilon}$	σ_{max}
CaMg-17	creep	1023	29	0.124	$2\cdot10^{-6}$– $6\cdot10^{-7}$	27
CaMg-19	creep	1023	29	0.333	$2\cdot10^{-5}$–$1\cdot10^{-6}$	38
CaMg-20	creep	1023	29	0.031	$4\cdot10^{-7}$–$1\cdot10^{-9}$	17
CaMg-21	creep	1023	29	0.029	$3\cdot10^{-7}$–$1\cdot10^{-9}$	7
CaMg-22	creep	1023	4	0.192	$1\cdot10^{-5}$–$7\cdot10^{-6}$	22
CaMg-23	creep	1023	76	0.107	$1\cdot10^{-6}$–$1\cdot10^{-7}$	15
CaMg-24	creep	1023	50	0.123	$1\cdot10^{-6}$–$3\cdot10^{-7}$	15
CaMg-25	creep	1023	171	0.081	$4\cdot10^{-7}$–$7\cdot10^{-8}$	17
CaMg-26	creep	1023	29	0.167	$5\cdot10^{-6}$ –$5\cdot10^{-7}$	24
CaMg-33	creep	1023	119	0.013	$3\cdot10^{-10}$–$4\cdot10^{-9}$	19
CaMg-31	creep	773	24	0.130	$2\cdot10^{-5}$ –$8\cdot10^{-7}$	65
	anneal	1023	29	-	-	-
Torsion				γ	$\dot{\gamma}$	τ_{max}
CaMg-18	creep	1023	29	0.8	$6\cdot10^{-5}$–$2\cdot10^{-6}$	12
CaMg-27	ctr	1023	18	3.5	$6\cdot10^{-5}$	11.5
CaMg-28*	creep	1023	16 (29)	0.4	$8\cdot10^{-5}$–$2\cdot10^{-7}$	13.3
CaMg-29	creep	1023	97	2.1	$5\cdot10^{-5}$–$5\cdot10^{-7}$	12.3
CaMg-30	creep	1023	29	5.6	$2\cdot10^{-4}$–$2\cdot10^{-5}$	14.5

Table 3.2 Mechanical data of deformation experiments on calcite-magnesite single crystal stacks at 400 MPa confining pressure at varying temperatures (T) and run durations (t). Deformation tests were either performed at constant stress (creep) or at constant twist rate (ctr). Data represent the resulting axial stress σ_{max}, axial strain (ε) and strain rate ranges ($\dot{\varepsilon}$) for triaxial compression experiments and the maximum shear stress τ_{max}, shear strain (γ) and shear strain rate ranges ($\dot{\gamma}$) for torsion tests. Experiment CaMg-31 was pre-deformed at 773 K for 24 h at the given conditions and afterwards annealed at 1023 K for 29 h (anneal).

Temperature was controlled using a thermocouple (Pt-Pt/13%Rh), 3 mm away from the sample stack. The elevated confining pressure ensures a good contact of sample interfaces and prevents carbonates from decomposition. Heating and cooling rates were 20 °C/min and 2 °C/min, respectively. Reported stresses and strains were calculated assuming constant volume deformation of calcite single crystals only, which were considerably weaker than magnesite at the experimental conditions. Magnesite showed almost no inelastic deformation. All values were corrected for the strength of the copper sleeve and apparatus distortion

(RYBACKI ET AL. 2013).

A total of 11 triaxial loading experiments were performed with run durations of 4 to 171 h and axial stresses between 7 and 65 MPa (**Table 3.2**). To explore the effect of deformation on reaction rates, 5 samples were deformed for 29 h at varying axial stresses between 7 and 38 MPa, resulting in final strains of 2.9-33.3%. The time dependence of rim growth at axial stresses of 17 ± 2 MPa was measured on 5 samples at run durations between 29 and 171 h, yielding total final strains between 1.3% and 12.3%. To test the possible influence of pre-existing crystal defects in the starting material on the mineral reaction, we pre-deformed one sample (CaMg-31) at 500 °C for 24 hours by increasing the axial stress stepwise up to 65 MPa, resulting in total axial strain of 13%. Subsequently, the sample was annealed for 29 hours to promote dolomite reaction. In addition, 5 torsion tests were performed at similar *P-T* conditions allowing investigation of the influence of stress and strain on rim growth within a single sample (**Table 3.2**). Unlike in triaxial compression, stress and strain within twisted samples are distributed inhomogeneously. Both vary from almost zero in the center of the sample to a maximum at the outer periphery of the cylinders. Strain increases linearly with the sample radius while stress increases non-linearly for dislocation-accommodated creep. Assuming power-law creep rheology, shear stress at any radius is given by (PATERSON AND OLGAARD 2000):

$$\tau(r) = \tau_{max}\left(\frac{2r}{d}\right)^{\frac{1}{n}} \qquad \textbf{(3.2)}$$

where $r$and d refer to the radius and diameter of the sample, respectively and τ_{max} is the maximum shear stress at the outer periphery. For the stress exponent n, we used a value of 9.5, based on results for calcite single crystal deformation in the temperature range between 700-800 °C (DE BRESSER 1991). Four tests were done at t = 29-97 h and constant torques of about 1.4 and 1.9 Nm, equivalent to maximum shear stresses of ≈12 and 14.5 MPa at the sample surface. The resulting maximum shear strains of calcite are 0.4 to 5.6 (**Table 3.2**). In addition, one sample was deformed at a constant twist rate for 18 h up to a maximum shear strain of 3.5, resulting in a maximum shear stress of 11.5 MPa.

For comparison of torsion and triaxial compression experiments, shear stresses (τ)and strain rates ($\dot{\gamma}$) were converted to equivalent axial stresses σ_{eq} and equivalent strain rates ($\dot{\varepsilon}_{eq}$) (**Table 3.3**) using the relations (PATERSON AND OLGAARD 2000):

$$\sigma_{eq} = \sigma_{ax} = \tau\sqrt{3} \quad \textbf{(3.3)}$$

$$\dot{\varepsilon}_{eq} = \dot{\varepsilon}_{ax} = \frac{1}{\sqrt{3}}\dot{\gamma} \quad \textbf{(3.4)}$$

Experiment	Equivalent axial strain	Equivalent axial stress	Δx_{Dol}	Δx_{Pal}	Δx_{gran}	Δx_{Mg-Cal}	a_{Pal}	a_{gran}	a_{Mg-Cal}
Triaxial		(MPa)	(µm)	(µm)	(µm)	(µm)	(µm)	(µm)	(µm)
CaMg-17	0.124	27	12.9 ± 3.4	7.3 ± 2.5	5.6 ± 1.7	35.5 ± 7.9	4.8 ± 1.7	4.2 ± 1.1	28.0 ± 13.9
CaMg-19	0.333	38	8.3 ± 2.3	5.4 ± 1.7	2.9 ± 1.2	36.0 ± 14.2	2.6 ± 0.7	2.7 ± 0.9	20.7 ± 11.8
CaMg-20	0.031	17	10.5 ± 2.3	5.8 ± 1.5	4.7 ± 1.5	29.1 ± 8.1	2.2 ± 0.4	2.2 ± 0.6	22.1 ± 12.0
CaMg-21	0.029	7	10.7 ± 3.8	6.5 ± 2.3	4.2 ± 2.3	29.1 ± 8.9	2.6 ± 0.5	2.4 ± 0.5	23.8 ± 12.4
CaMg-22	0.192	22	11.1 ± 3.4	5.2 ± 2.3	5.9 ± 1.8	35.3 ± 20.1	3.2 ± 1.1	2.8 ± 0.8	22.5 ± 12.2
CaMg-23	0.107	15	24.3 ± 3.8	13.2 ± 2.7	11.2 ± 2.7	63.3 ± 11.5	5.2 ± 1.2	5.0 ± 1.0	34.8 ± 18.3
CaMg-24	0.123	15	15.4 ± 4.7	8.5 ± 2.8	6.9 ± 2.8	50.5 ± 17.4	4.9 ± 1.2	4.3 ± 1.0	27.3 ± 14.4
CaMg-25	0.081	17	16.7 ± 3.3	9.9 ± 2.4	6.9 ± 1.8	64.4 ± 10.8	3.4 ± 0.7	3.2 ± 0.8	38.8 ± 18.4
CaMg-26	0.167	24	11.9 ± 2.9	7.3 ± 2.0	4.6 ± 2.4	41.1 ± 19.7	3.1 ± 0.8	3.0 ± 0.8	21.0 ± 9.9
CaMg-33	0.013	19	24.7 ± 14.7	16.7 ± 8.16	10.9 ± 6.1	43.2 ± 16.3	6.7 ± 1.6	5.5 ± 1.4	35.7 ± 21.3
CaMg-31	0.130	65	6.4 ± 2.2	NA	NA	25.0 ± 8.4	1.1 ± 0.5	2.6 ± 0.5	22.0 ± 11.0
Torsion									
CaMg-18	0.5	20.8	20.1 ± 6.7	10.2 ± 3.9	9.9 ± 3.9	38.2 ± 8.5	6.0 ± 2.1	5.0 ± 1.7	24.5 ± 11.4
CaMg-27	2	19.9	13.2 ± 4.1	NA	NA	27.3 ± 9.3	3.6 ± 1.3	3.6 ± 0.8	32.2 ± 16.7
CaMg-28	0.2	23	11.1 ± 4.1	5.7 ± 1.6	5.3 ± 1.3	28.1 ± 12.8	4.0 ± 0.8	3.8 ± 1.0	26.0 ± 12.7
CaMg-29	1.2	21.3	24.5 ± 9.1	NA	NA	58.3 ± 16.6	6.6 ± 1.8	6.4 ± 1.6	27.4 ± 17.0
CaMg-29-TG	1.1	21.1	2.9 ± 1.1	NA	NA	42 ± 8.1	NA	NA	22.0 ± 11.0
CaMg-30	3.2	25.1	9.1 ± 3.5	NA	NA	33.3 ± 11.7	4.1 ± 1.1	4.1 ± 0.9	21.0 ± 12.3
CaMg-30-TG	3.1	25	2.9 ± 1.1	NA	NA	22.4 ± 10.9	NA	NA	7.8 ± 3.3

Table 3.3 Stress strain conditions and microstructural data of reaction products, given by the average layer thickness of entire dolomite (Δx_{Dol}), dolomite palisades (Δx_{Pal}), granular dolomite layers (Δx_{gran}) and magnesio-calcite (Δx_{Mg-Cal}). Mean grain diameter of dolomite palisades, granular dolomite and magnesio-calcite are denoted by a_{Pal}, a_{gran} and a_{Mg-Cal}, respectively. The abbreviation 'NA' indicates Not Available.

3.4 Mechanical behavior

3.4.1 Triaxial experiments

Equivalent strain-time curves of triaxial compression experiments performed at run durations between 4 and 171 h and axial stresses of σ_{ax}= 17 ± 2 MPa are shown in **Figure 3.1 a**. Initial elastic deformation led to axial strains between 0.008 and 0.02, followed by primary creep with hardening. Nearly steady-state creep was observed for samples CaMg-25 and CaMg-20 yielding approximate strain rates of $7 \cdot 10^{-8}$ s^{-1} and $1 \cdot 10^{-9}$ s^{-1}, respectively (steps in curve of sample CaMg-25 are induced by argon pump strokes to ensure a constant confining pressure). Sample CaMg-33 exhibited a very slow strain rate on the order of $4 \cdot 10^{-9}$ s^{-1} after yielding, while sample CaMg-24 deformed much faster with a final rate of $\approx 3 \cdot 10^{-7}$ s^{-1}.

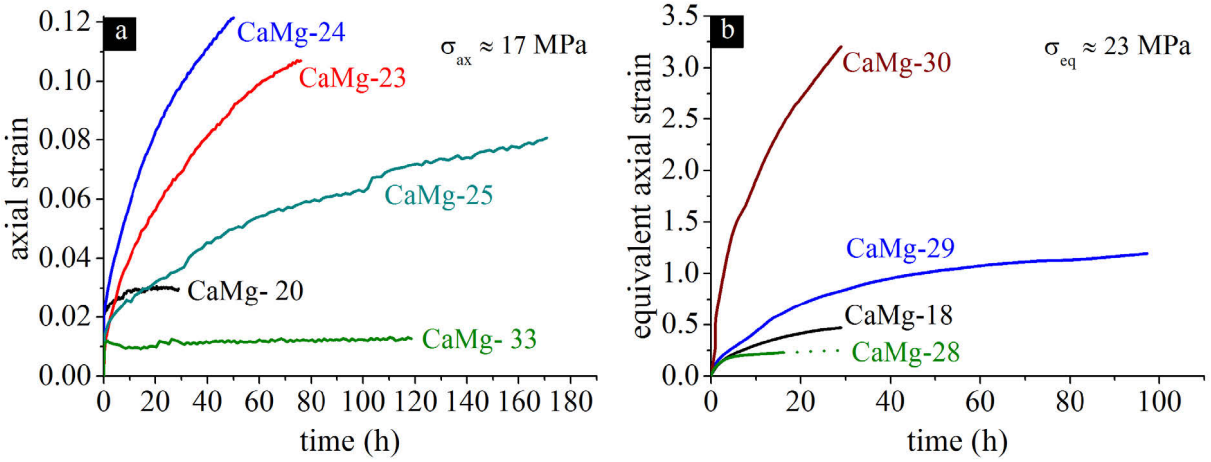

Figure 3.1 Equivalent strain-time curves of deformed samples at 750 °C temperature and 400 MPa confining pressure for (**a**) triaxial compression experiments at σ_{ax} = 17 ± 2 MPa and (**b**) torsion tests at σ_{eq} = 23 ± 2 MPa. Individual curves are labeled by sample number.

3.4.2 Torsion experiments

Four samples were twisted at constant torques yielding maximum equivalent stresses between 19.9 - 25.1 MPa and equivalent strains of 0.2 to 3.2 at the sample periphery (**Figure 3.1 b**). Initial equivalent strain rates after yielding are in the range of 10^{-4}-10^{-5} s^{-1}, decelerating by about 1-2 orders of magnitude towards steady state conditions at the end of testing. Sample CaMg-28 slipped after ≈16 h deformation and was subsequently annealed for 13 h for comparison with other samples (**Table 3.2**). The final equivalent strain rates of samples CaMg-18 and CaMg-29 were $\approx 1.4 \cdot 10^{-6}$-$1.3 \cdot 10^{-6}$ s^{-1}. Sample CaMg-30 showed a substantially faster increase in strain with time resulting in a final equivalent strain rate of $\approx 1.5 \cdot 10^{-5}$ s^{-1}.

3.5 Microstructures

3.5.1 Deformation microstructures of single crystal reactants

Sample stacks deformed in axial compression show barrel-shaped distortion of calcite single crystals (**Figure 3.2 a**). In contrast, magnesite single crystals exhibit (possibly unloading) microfractures, which are locally constrained at the samples' edges in the low stress (7 MPa) experiment and homogeneously distributed at higher stresses. In all triaxial compression experiments, calcite single crystals exhibit deformation twins (**Figure 3.2 a, c, e**). At least two sets of twins are common, but three sets also occur at stresses above 7 MPa. Formation of twins preferentially starts at the edges of the single crystal or at contact interfaces (**Figure 3.2 a**). Although most of the twins appear as parallel, few microns thin straight lines in low stress experiments, some curved thicker wedge-shaped twins also occur in high stress tests. The former are frequent, even spaced and penetrate often the whole crystal, while the latter mostly appear in small size patches. Deformation zones evolve in high stress experiments, characterized by undulose extinction, subgrain formation and irregular boundaries with the less deformed crystal parts. These zones lead to distortion of pre-existing straight twin sets and formation of low angle grain boundaries (**Figure 3.2 c**). Some large magnesio-calcite grains adjacent to pure calcite also contain thin straight twins (**Figure 3.2 e**) with different orientation from those in pure calcite, presumably by rotation of magnesio-calcite grains. Microcracking is rare in calcite, but if present, mostly in orientations mimicking the natural cleavages. In contrast, magnesite single crystals show abundant distinct microfractures (**Figure 3.2 a**), often parallel to the orientations of natural cleavages and seldom curved microcracks.

In torsion experiments, calcite single crystals accommodate most of the bulk strain (**Figure 3.2 b**). As seen in **Figure 3.2 b** the strain is not necessarily distributed homogenously, but shows a bilinear partioning. Next to the reaction interface up to half of calcite reactant, the strain is twice larger compared to the rest of the calcite. Analogously to triaxial experiments, every calcite crystal exhibits at least two sets of twins with thin twins cross-cutting the whole crystals. Thick, wedge-shaped twins are wider and longer compared to triaxial compression tests. Cracks in calcite are straight with distinct orientations and interaction with twins is common (**Figure 3.2 d**). Cross-cutting of twin sets is more distinguished in twisted than in axially compressed samples, leading to the formation of new subgrains indicated by low angle grain boundaries (**Figure 3.2 f**). In the high stress/strain experiment CaMg-30 ap-

proximately 90% of the whole calcite single crystal is composed of patchy areas of curved twins. Abundant polygonal grains formed at the high strain periphery. As in triaxial experiments, oriented microfractures in magnesite are common in torsion experiments.

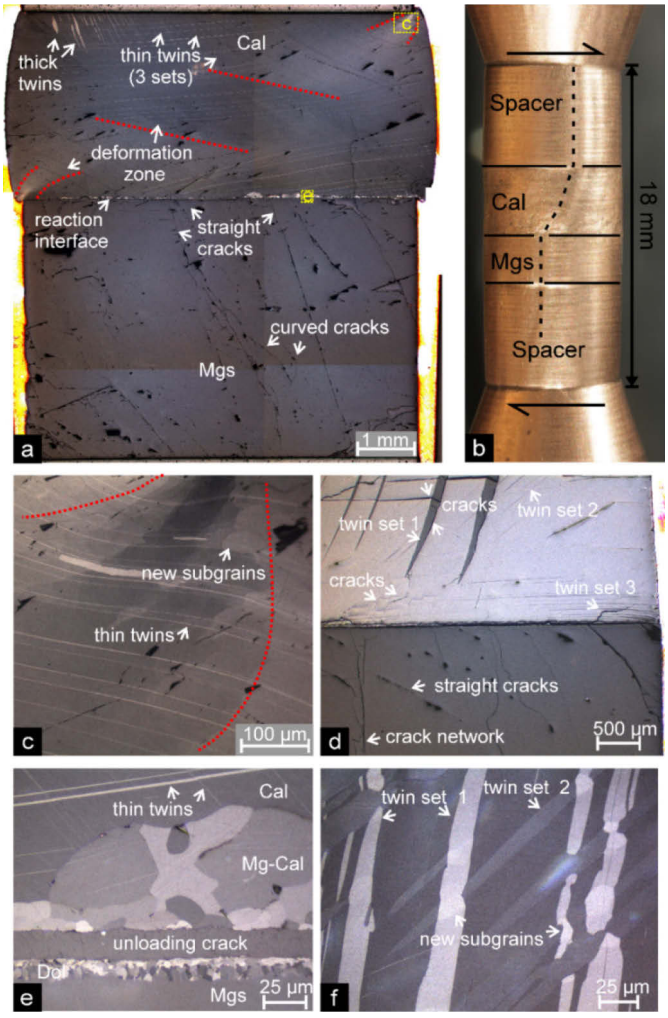

Figure 3.2 Deformation microstructures in single crystal reactants induced by axial compression (left column) and torsion (right column). (**a, c, e**) Sample CaMg-22, triaxially deformed at 24 MPa for 4 h. (**b, d, f**) Sample CaMg-28, twisted for 29 h with a maximum equivalent stress of 23 MPa. (**a**) Barrel-shaped calcite single crystal (Cal) with 2 sets of thin twins penetrating the whole sample and with thick, wedge-shaped curved twins at the upper left edge. Deformation zone boundaries are indicated by *dashed red lines*. The magnesite single crystal (Mgs) shows mostly straight cracks and minor curved cracks. (**b**) Jacketed sample after torsion with dextral shear sense. *Dashed black line* shows the distribution of strain indicated by wrinkles in the copper sleeve. (**c**) Close up of a deformation zone outlined in (**a**) showing curved twins and the formation of low angle grain boundaries. (**d**) Twisted sample exhibiting 3 twin sets and some microcracks in calcite, apparently interacting with twins. Magnesite shows straight microcracks with different orientations similar to the axially compressed sample. (**e**) Cross-cutting thin twin sets in calcite next to the reaction interface. Note that larger magnesio-calcite grains inherit thin straight twins with different orientations. (**f**) Interaction of two twin sets in calcite leading to necking and the formation of small angle boundaries. Note different scales.

3.5.2 Reaction rim microstructures

Reaction products at the contact interfaces between calcite and magnesite single crystals are composed of polycrystalline dolomite rims and large magnesio-calcite grains in contact with pure calcite. Dolomite rims consist of palisade-shaped, elongated grains growing into magnesite and granular dolomite grains growing towards calcite reactants. In addition, large magnesio-calcite grains formed in contact with granular dolomite due to the incorporation of Mg into pure calcite, which is interpreted as a precursor to dolomite nucleation (HELPA ET AL. 2014). Grain sizes of magnesio-calcite tend to increase from the dolomite boundary towards pure calcite (**Figure 3.3**). Large magnesio-calcite grains next to pure calcite show convex grain boundaries and often straight boundaries with neighboring grains including 120° triple junctions. The curved grain boundaries of magnesio-calcite towards pure calcite indicate that growth of grains occurs by chemically-induced grain boundary migration accompanied by diffusion processes (EVANS, HAY, AND SHIMIZU 1986; HERWEGH, XIAO, AND EVANS 2003).

Quite similar microstructures to those observed in triaxially deformed samples at different stresses and strains (**Figure 3.3 b-d, g**) evolved in static annealing experiments using comparable starting materials and similar P, T, t conditions (**Figure 3.3 a**; adopted from HELPA ET AL. 2014). The boundary between palisades and granular dolomite was identified by platinum markers as the initial contact of starting materials. Considering large error bars, axial stresses up to 38 MPa at t = 29 h yield no significant influence of the average reaction rim width of dolomite and magnesio-calcite (**Table 3.3**; **Figure 3.4 a**).

The time series performed at stresses of 17 ± 2 MPa shows a linear increase of dolomite rim thickness with the square root of time (**Figure 3.4 c**), indicating that the reaction progress is diffusion-controlled as observed in static annealing tests (HELPA ET AL. 2014, *solid line* in **Figure 3.4 c**). The outlier at t = 171 h (sample CaMg-25) can be explained by a long crack in the calcite single crystal with adjacent large magnesio-calcite grains, probably acting as sink for diffusion of the MgO component and therefore lowering the magnesio-calcite and dolomite production at the reaction interface. In contrast, the magnesio-calcite layer shows enhanced growth at almost all durations compared to annealed samples (*broken line* in **Figure 3.4 c**), in particular for high strain samples. Application of axial stresses led to a larger variation of the entire dolomite reaction rim thickness across the initial contact area compared to annealing experiments (**Figure 3.5**). Fluctuations of the magnesio-calcite layer thickness are also very large, up to 57% within a single sample, resulting from pronounced grain boundary migration (**Figure 3.2**). At the edges of the contact interface, the magnesio-calcite

layer is dragged by the deforming calcite single crystal (**Figure 3.2 a**). For the thinner dolomite rim no unambiguous extrusion or dragging is noticeable.

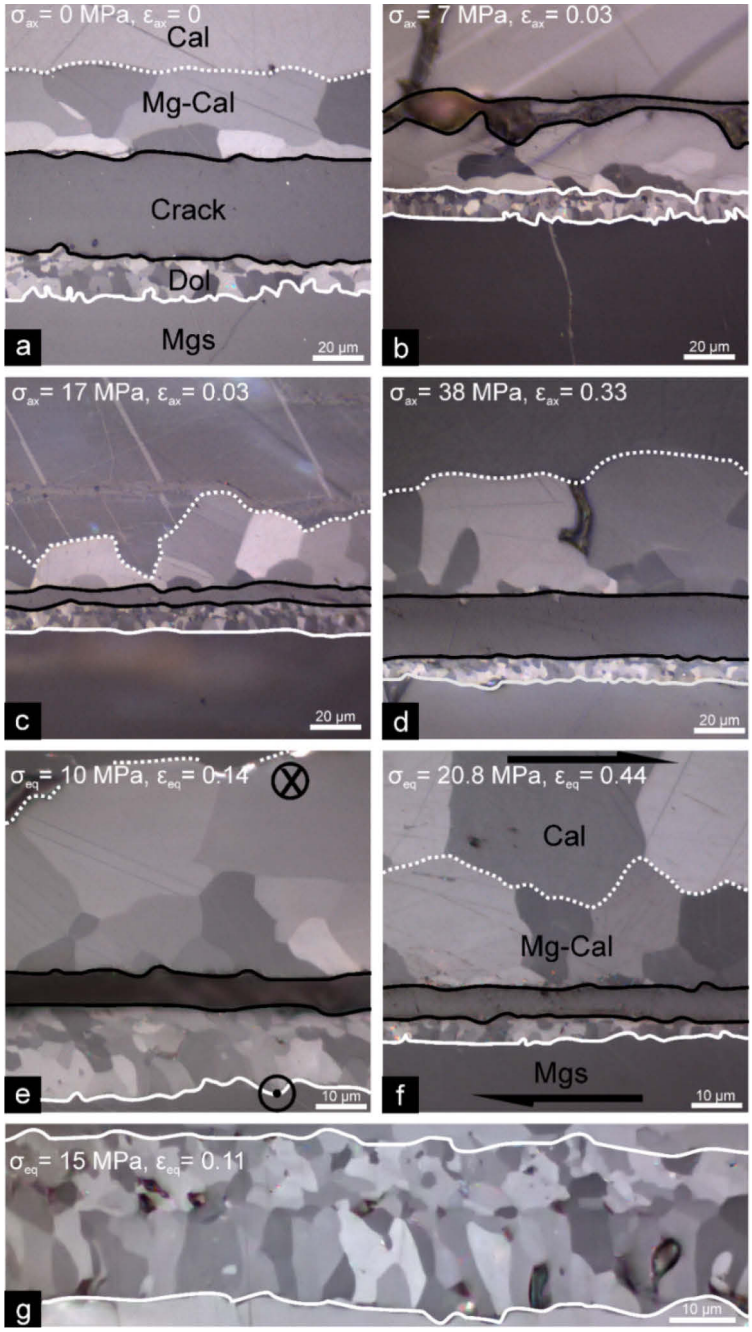

Figure 3.3 Optical micrographs of dolomite (Dol) and magnesio-calcite (Mg-Cal) reaction products in between single crystal reactants of calcite (Cal) and magnesite (Mgs) at different experimental conditions. Epoxy filled unloading cracks are surrounded by *black lines*, while *white lines* represent phase boundaries. (**a-f**) All experiments were performed at 750 °C for 29 h. Stress-strain conditions are given in each micrograph. Note different scales. (**a**) Annealing experiment (sample CaMg-15 from HELPA ET AL. 2014), (**b-d**) triaxial compression experiments and (**e-f**) torsion test. (**e-f**) Micrographs are from sample CaMg-18 showing (**e**) an almost central part of an axial longitudinal section and (**f**) a high stress/strain location within the tangential section. The sense of shear is indicated by *arrows*. (**g**) Internal microstructure of dolomite rim formed in triaxial compression for 76 h.

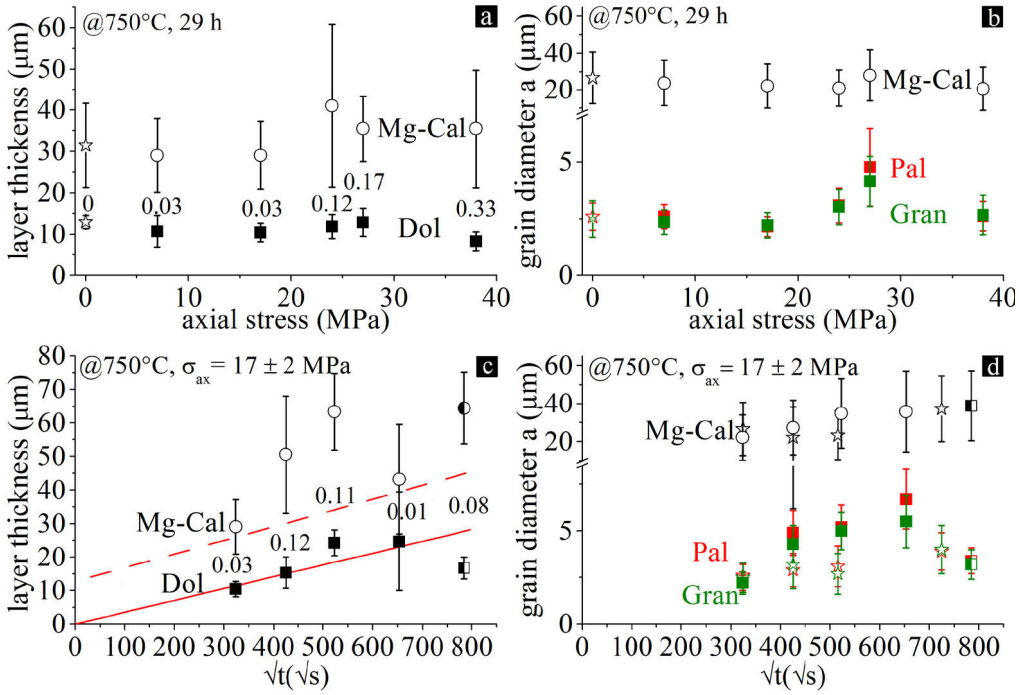

Figure 3.4 Average reaction rim thicknesses and gran sizes of magnesio-calcite (Mg-Cal) and dolomite (Dol) in axially compressed samples. All tests were performed at T = 750°C and either at a fixed time of t = 29 h and varying axial stress from 7 to 38 MPa (**a, b**) or a fixed axial stress of σ_{ax} = 17 ± 2 MPa in a time range between 29-171 h (**c, d**). (**a**) Reaction rim thickness of magnesio-calcite and dolomite (including palisades and granular grains) shows no systematic correlation with stress for dolomite and a slight increase of magnesio-calcite thickness above ≈20 MPa stress. The results of a static annealing test (0 MPa axial stress) indicated by *open stars* at similar conditions are adopted from HELPA ET AL. (2014). *Values* besides the symbols indicate the total strain of the test. (**b**) Grain diameters for magnesio-calcite, dolomite palisades and granular dolomite grains with increasing applied axial stress. (**c**) Increase of dolomite layer thickness with square-root of time. *Red lines* represent results of annealing experiments at similar temperature for dolomite reaction rim thickness (*solid line*) and magnesio-calcite thickness (*dashed line*), adopted from HELPA ET AL. (2014). The dolomite rim thicknesses of deformed and annealed samples are in good agreement, while magnesio-calcite is often thicker. *Half open symbols* are probably underestimated values of long lasting experiment CaMg-25 (see text for explanation). As in (**a**), values represent the total strains. (**d**) Grain coarsening in triaxial compression tests versus square-root of experimental run duration. For comparison, results of annealing test are shown by stars (HELPA ET AL. 2014). Again, *half open symbols* may be underestimated values.

In torsion experiments some distinct differences to axial compression tests are obvious, regarding the layer thickness variation along the contact interface. Dolomite reaction rim thickness and magnesio-calcite layer width decrease from the center of the sample towards the edge (**Figure 3.5**, **Figure 3.6**). The magnesio-calcite layer is about twice the size in the center compared to the periphery, while the difference in dolomite reaction rim thickness is up to a factor of 6. Continuous reduction in layer thickness of dolomite and magnesio-calcite is noticeable at a radius of about 1.9 mm, corresponding to equivalent stress and strain conditions of σ_{eq}≈ 20 MPa; ε_{eq}≈ 0.3 for sample CaMg-18 and σ_{eq}≈ 20 MPa, ε_{eq}≈ 0.5-0.6 for sample CaMg-30 (**Figure 3.6**). For twisted sample CaMg-30, the onset of width reduction occurs at σ_{eq}≈ 22 MPa and ε_{eq}≈ 0.7 (**Figure 3.5**).

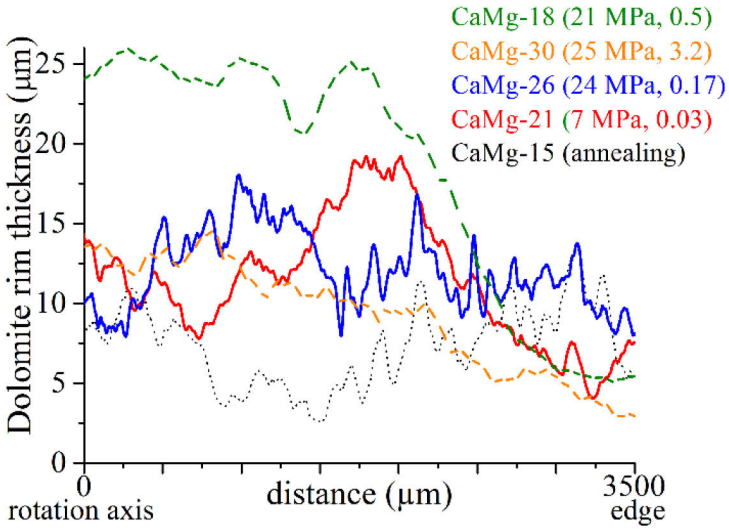

Figure 3.5 Variation of dolomite reaction rim thickness from the center (*rotation axis*) of samples towards their periphery. Triaxial tests (CaMg-26, -21) are represented by *solid lines*, torsion tests (CaMg-18, -30) by *dashed lines* and the annealing experiment (CaMg-15, HELPA ET AL. 2014) by the *dotted line*. All experiments were performed at 400 MPa confining pressure, 750 °C temperature and a run duration of 29 h. Compared to annealed sample, triaxially deformed samples show more rim thickness fluctuation and twisted samples exhibit a strong decrease of rim width from approximately half of the distance towards their edge. Stress, strain conditions are labelled.

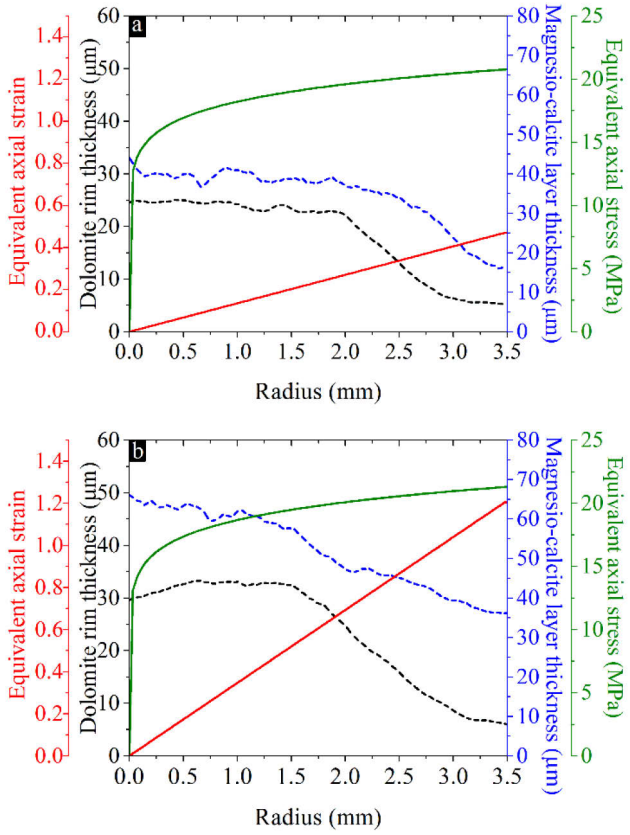

Figure 3.6 Stress, strain, dolomite and magnesio-calcite layer thickness along the radius of twisted samples (**a**) CaMg-18 (t = 29 h, max. σ_{eq}= 20.8 MPa, max. ε_{eq} = 0.5) and (**b**) CaMg-29 (t = 97 h. max. σ_{eq}= 21.3 MPa, max. ε_{eq}= 1.2).

For detailed microstructural analyses, 6 different areas were selected within sample CaMg-18, reflecting different strain conditions of ε_{eq} = 0.09-0.43 at σ_{eq}= 18.0-19.2 MPa, respectively (**Table 3.4**).

Type	**18c**	**18b**	**18d**	**18f**	**18e**	**18a**
σ_{eq} **(MPa) /** ε_{eq}	**18.03 / 0.09**	**18.83 / 0.17**	**18.95 / 0.18**	**19.10 / 0.32**	**19.17 / 0.43**	**19.17 / 0.43**
Δx_{Dol} (µm)	18.9 ± 2.6	28.7 ± 4.7	20.5 ± 1.7	15.9 ± 1.7	3.6 ± 0.9	4.7 ± 0.9
$\tilde{a}_{Dol}$ (µm)	5.6 ± 3.1	6.4 ± 3.6	5.6 ± 3.8	5.6 ± 2.3	3.0 ± 1.0	4.7 ± 4.3
AR_{Dol}	2.1 ± 0.8	1.8 ± 0.7	1.9 ± 0.8	1.9 ± 0.6	1.9 ± 0.7	1.9 ± 0.7
$\tilde{a}_{Pal}$ (µm)	7.7 ± 3.4	7.2 ± 3.5	8.2 ± 4.2	6.6 ± 2.3	3.1 ± 1.1	3.4 ± 1.1
AR_{Pal}	1.9 ± 0.6	1.8 ± 0.5	1.8 ± 0.6	1.8 ± 0.5	1.9 ± 0.7	1.8 ± 0.7
Δx_{Mg-Cal} (µm)	28.0 ± 14.8	35.4 ± 5.9	38.4 ± 9.8	33.3 ± 7.1	15.4 ± 3.3	27.7 ± 2.0
$\tilde{a}_{Mg-Cal}$ (µm)	17.4 ± 11.6	16.7 ± 11.6	19.2 ± 12.2	14.9 ± 11.4	7.2 ± 4.6	9.7 ± 6.4
AR_{Mg-Cal}	1.8 ± 0.6	1.9 ± 0.6	2.1± 0.9	2.2 ± 1.0	1.9 ± 1.0	1.8 ± 0.6

Table 3.4 Microstructure evolution of twisted sample CaMg-18. Data represent rim/layer thickness (Δx), corrected grain sizes ($\tilde{a}$) and aspect ratios (AR) for entire dolomite, dolomite palisades and magnesio-calcite within six areas (18 a-f) with different σ_{eq}- ε_{eq}conditions.

At almost constant stress and increasing strain from the center towards the edge, the entire dolomite rim width decreases from Δx_{Dol} = 18.9 ± 2.6 µm to 3.6 ± 0.9 µm and the magnesio-calcite layer thickness decreases from Δx_{Mg-Cal} = 28.0 ± 14.8 µm to 15.4 ± 3.3 µm. Associated with decreasing rim thickness, the average grain size of the entire dolomite rim reduces slightly with increasing strain from 5.6 µm to 3.0-4.7 µm, but the aspect ratios (AR) of ≈ 2 remains almost constant (**Table 3.4**; **Figure 3.3 e-f**). In particular, for dolomite palisades in contact with magnesite the grain size reduces from $\tilde{a}_{Pal}$= 7.7 ± 3.5 µm to $\tilde{a}_{Pal}$= 3.1 ± 1.1 µm, again with no significant change in AR (≈ 1.9). Also, the average grain size of magnesio-calcite decreases with strain from 17.4 ± 1.8 µm to 9.7 ± 1.8 µm, with a constant AR of about 1.9.

The average grain sizes of palisade-shaped dolomite (a_{Pal}) and granular dolomite (a_{gran}) are larger in torsion experiments than in axial compression tests at comparable durations, where the latter reveal no significant influence of the applied stress magnitude (**Table 3.3**). For example, at t = 29 h, a_{Pal}= 2.6 ± 0.6 µm after annealing, a_{Pal}= 2.6 ± 0.5 µm at 7 MPa and a_{Pal} = 2.6 ± 0.7 µm at 38 MPa stress (**Figure 3.4 b**), and a_{Pal}= 4.0 ± 0.8 - 6.0 ± 2.1 µm for twisted samples at 21-25 MPa stress. Granular dolomite grains also show similar average grain sizes with a_{gran}= 2.4-2.7 µm, independent of axial stress (**Figure 3.4 b**), whereas

twisted samples span 3.8 to 5.0 µm in grain size (**Table 3.3**). In contrast, the average grain size of magnesio-calcite is in the range of a_{Mg-Cal}≈ 21-27 µm, almost unaffected by stress in triaxial and torsion deformation (**Figure 3.4 b; Table 3.3**). However, grain coarsening with time occurred in all microstructural domains (**Figure 3.4 d**). For example, at t = 29 h, a_{Pal} and a_{gran} are in the range of 2.2 µm each, whereas at t = 119 h both domains contain larger grains with a_{Pal}= 6.7 ± 1.6 µm and a_{gran}= 5.5 ± 1.4 µm. This increase in grain size appears to be more pronounced in deformation than in isostatic annealing tests (cf., **Figure 3.4 d**). For magnesio-calcite an increase in grain size with time from 22.1 ± 12.0 µm to 35.7 ± 21.3 µm is observed. As mentioned before, results of a long duration experiment (CaMg-25) may provide lower values than expected due to the migration of the MgO component along the inclined crack.

TEM reveals distinct densities of dislocations in the various reaction rim areas. **Figure 3.7 a** and **b** show TEM micrographs of different parts of the dolomite reaction rim evolved in the triaxially deformed sample CaMg-17 (σ_{ax}= 27 MPa, t = 29 h). Calcium rich (see below) dolomite close to the interface to magnesio-calcite shows irregular grain boundaries and patches of frequent, often parallel, dislocations (**Figure 3.7 a**). The central part of the dolomite reaction rim close to the initial contact interface shows dislocation-poor dolomite palisades (*P* in **Figure 3.7 b**) with gently curved grain boundaries. In contrast, granular dolomite grains (*G*) show abundant dislocations close to the grain boundary (*arrow* in **Figure 3.7 b**). Within the granular layer, evolution of pores appears adjacent to areas with high dislocation density. The same microstructural features within distinct domains were also observed in sample CaMg-20, deformed at a lower stress of 17 MPa and t = 29 h. Magnesio-calcite grains usually reveal relatively high dislocation densities. For example, sample CaMg-21 (σ_{ax}= 7 MPa, t = 29 h) contains densities of about 2.1 ± 0.7·10^{13} m^{-2} (**Figure 3.7 c**), determined by the point intersect method (BUTLER 1969). Dislocations are usually curved and tangled near grain boundaries and less frequent (≈8·10^{12} m^{-2}) and straight in the cores of individual magnesio-calcite grains. Magnesite and calcite single crystals exhibit only a few straight dislocations with a density less than ≈8·10^{12} m^{-2} and ≈1·10^{12} m^{-2}, respectively.

In torsion experiments a remarkable difference in the dislocation density between dolomite in the inner (low stress/strain) and outer part (high stress/strain) occurs. Similar to triaxially deformed samples, the microstructure in the central area reveals dislocation-poor palisade-shaped dolomite, but granular dolomite is also almost free of dislocations with straight

grain boundaries forming 120° triple junctions (**Figure 3.7 d**). In the highly deformed outer part, all dolomite grains are equiaxed with abundant dislocations close to the curved grain boundaries (**Figure 3.7 e**). Magnesio-calcite grains at the edge of twisted samples also contain dislocations (**Figure 3.7 f**, sample CaMg-18), which are straighter compared to triaxially deformed samples, partially forming dislocation walls.

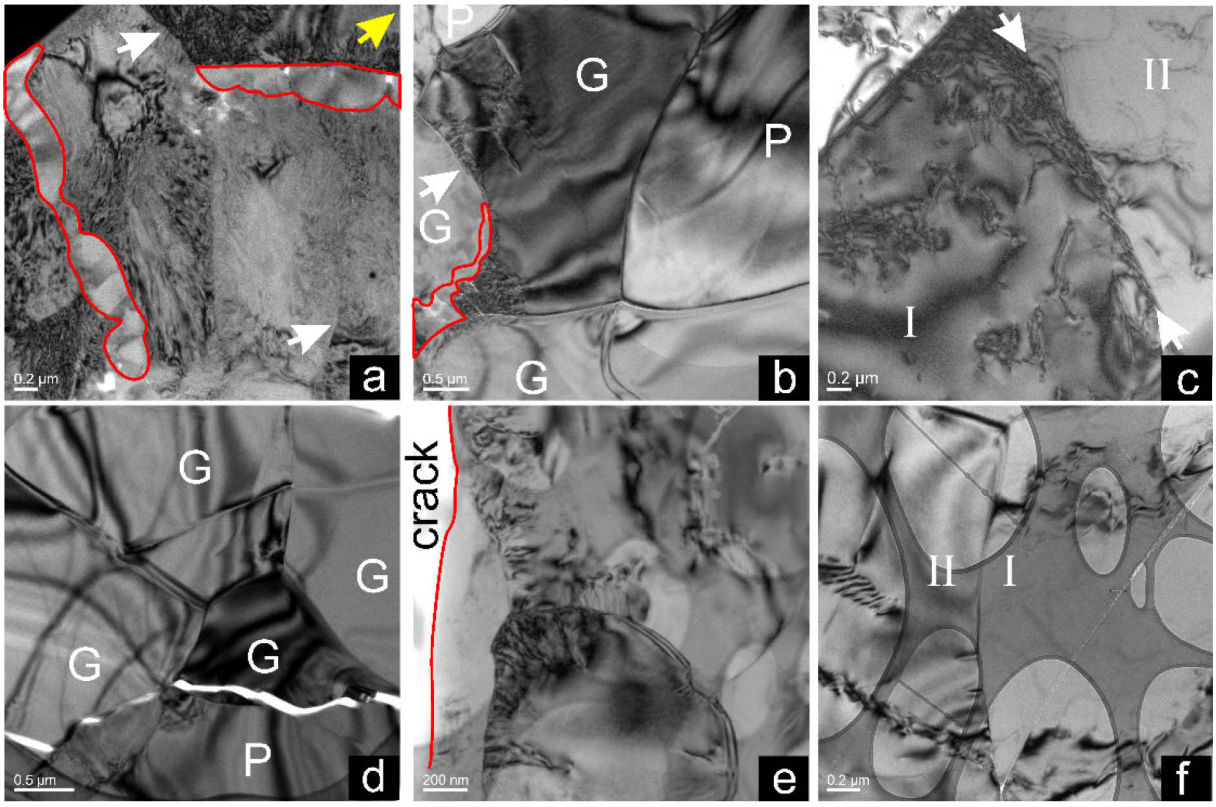

Figure 3.7 Bright field transmission electron micrographs of (**a-c**) axially compressed samples and **d-f** twisted sample CaMg-18 (σ_{max}= 20.8 MPa), all deformed for 29 h. Epoxy filled pores are indicated by red trace lines. (**a-b**) Dolomite reaction rim produced in experiment CaMg-17 (σ_{max}= 27 MPa). (**a**) Granular dolomite close to magnesio-calcite contains abundant crystal defects and irregular grain boundaries (*white arrows*). The *yellow arrow* points towards the direction of magnesite. (**b**) Central part of dolomite reaction rim. Palisades (*P*) show regular curved boundaries to neighboring grains. Dislocations are locally restricted at the grain boundary. Granular dolomite (*G*) show curved high angle boundaries, indicated by an *arrow*. (**c**) Sample CaMg-21 (σ_{max}= 7 MPa) show magnesio-calcite grains (*I, II*) with curved and tangled dislocations, concentrated near the grain boundary. (**d**) Dislocation poor dolomite with straight grain boundaries in the central part of sample CaMg-18 (ε_{eq}≈ 0.09). (**e**) Dolomite in the outer part of the reaction rim with abundant dislocations oriented perpendicular to grain boundaries (ε_{eq}≈ 0.44). (**f**) Two magnesio-calcite grains (*I, II*) from the outer part of the rim (ε_{eq}≈ 0.44), showing low angle grain boundaries. Holes are carbon film artifacts on the foil and not part of the sample.

3.6 Texture and chemistry

3.6.1 Texture analyses

Different areas of four samples deformed in axial compression and three samples deformed in torsion were selected to investigate orientation relationships between single crystal reactants and reaction products and to examine the texture evolution of reaction products with increasing applied stress/strain. In some cases, however, an accurate discrimination of dolomite palisades and granular grains via EBSD was not possible. Representative pole figures are illustrated in **Figure 3.8**, where the reaction interface (E-W) and the growing direction (GD) of reaction products (N-S) serve as a reference frame. For triaxially deformed samples, GD is parallel to the axis of maximum compression. In twisted samples GD is parallel to the rotation axis and the shear plane is parallel to the reaction interface. Since the starting material was cored perpendicular to one of the $\{10\bar{1}4\}$ planes, single crystal orientations are constrained by the orientation of one of the three $\{10\bar{1}4\}$ poles parallel to GD. This constraint implies a certain degree of freedom for the **c**-axis to arrange in a concentric girdle around the compression or rotation axis. Almost all deformed samples investigated in this study reveal only a weak crystallographic relationship of the reaction products with respect to the calcite reactant. In contrast to isostatic annealing experiments all reaction products show at least an axiotactic relationship with calcite reactants and full topotaxy prevailing in magnesio-calcite layers and granular dolomite (HELPA ET AL. 2014). Here, crystallographic relationships are most pronounced in the granular part of the dolomite reaction rim, but also observed in dolomite palisades and magnesio-calcite grains of some samples (cf., numbers **1-4** in **Figure 3.8**). Compared to the annealing experiments, most dolomite grains are rotated, so that the $[0001]$ axes reoriented parallel or near to GD and the poles of $\{2\bar{1}\bar{1}0\}$ and $\{10\bar{1}0\}$ prismatic planes rearranged within or close to the reaction interface.

The strength of the crystallographic preferred orientation (CPO) increases with increasing axial stress, for example for samples CaMg-21 and CaMg-20, deformed to similar axial strains of about 0.03, but at different stresses of 7 and 17 MPa, respectively (**Figure 3.8 a-b**). In dolomite palisades, the $[0001]$ axes are concentrated subparallel or at low angles to GD. The poles of prismatic planes $\{2\bar{1}\bar{1}0\}$ and $\{10\bar{1}0\}$ are distributed along broad and discontinuous girdles parallel to the reaction interface, whereas the poles of $\{10\bar{1}4\}$ rhombs are either parallel to GD or form three symmetric maxima. The CPO of granular dolomite is sometimes similar to that of the palisades (i.e., CaMg-20), but it may also differ significantly

(i.e., CaMg-21), where the [0001] maxima lies between the GD and the reaction interface and the poles of prismatic and rhomb planes are symmetrically distributed, mimicking the calcite single crystal (**Figure 3.8 a-b**). The CPO evolution shows no significant changes either with run duration (CaMg-25) or with further strain (CaMg-26).

Magnesio-calcite CPO is characterized by the strong alignment of [0001] axes parallel to the GD, with the poles of prismatic planes $\{2\bar{1}\bar{1}0\}$ and $\{10\bar{1}0\}$ forming a girdle parallel to the reaction interface and the poles of rhomb $\{10\bar{1}4\}$ forming a conical girdle around GD (**Figure 3.8 a-b**). Note that the number of magnesio-calcite grains is smaller than for dolomite in each map due to their large grain sizes. For this reason the CPO patterns appear to be stronger compared to dolomite.

In twisted samples, unambiguous discrimination of equiaxed and palisade-like dolomite grains was difficult, due to microcracks penetrating the reaction rim. However, at least in the central parts of the samples, a rotation of [0001] axes towards GD and a rearrangement of $\{2\bar{1}\bar{1}0\}$ and $\{10\bar{1}0\}$ poles within the reaction interface is evident in dolomite and magnesio-calcite. Unfortunately, it was not possible to obtain any reliable data for the outer high strain parts of the reaction rim due to bad indexing.

The distribution of misorientation angles between correlated dolomite-dolomite grain boundaries of most samples is random (**Figure 3.8 c**), except one remarkable peak associated with low angle grain boundaries (<11°). The shape of the distribution appears to be independent of the applied stress and loading direction (triaxial vs. shear), but the fraction f of low angle grain boundaries increases with increasing strain (e.g., from $f \approx$ 15-25% at ε_{ax}= 0.03 to $f \approx$ 34% at ε_{ax}= 0.17).

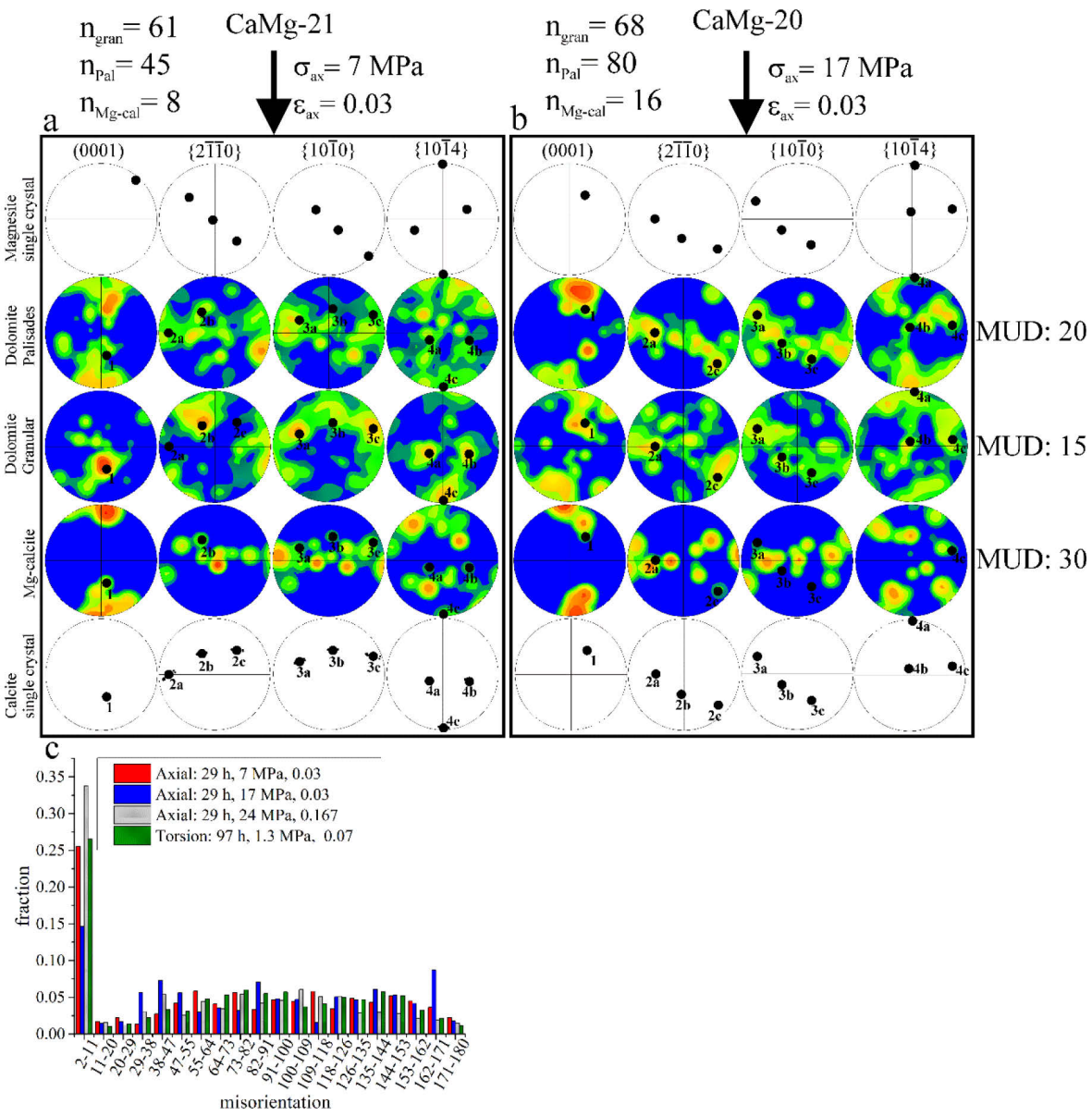

Figure 3.8 (**a-b**) Crystallographic preferred orientations of single crystal reactants (magnesite, calcite) and individual reaction products (dolomite palisades, granular dolomite and magnesio-calcite) of sample a CaMg-21 (σ_{ax}= 7 MPa) and (**b**) CaMg- 20 (σ_{ax}= 17 MPa), compressed for 29 h at 750 °C. Pole figures of [0001] axes and poles of prismatic planes {2$\bar{1}\bar{1}$0}/{10$\bar{1}$0} are equal-area lower hemisphere projections with a Gaussian half-width of 10° and a confidence index (CI) of >0.2. Pole figures of corresponding reaction products are color-contoured at the same scale, with maximum multiples of uniform distribution (MUD) between 15 and 30. Number of analyzed grains (n) is given by for individual reaction layers.The reference frame is defined by the E-W plane representing the reaction interface and the growing direction parallel to the direction of applied stress (*arrows*), oriented N-S. The numbers (**1-4**) on pole figures indicate individual crystallographic relationships between calcite single crystals and reaction products. (**c**) Distribution of misorientation angles (in 9° bins) from 2-180° within the entire dolomite reaction rim of triaxially compressed samples CaMg-21 (*red*), CaMg-20 (*blue*), CaMg-26 (*gray*) and of the central part of twisted sample CaMg-29 *(green*). Run durations, equivalent stresses and measured bulk strains are listed in the legend.

3.6.2 Chemical analyses

Chemical analyses via electron microprobe were performed on seven triaxially deformed samples and on three twisted samples. For each sample, we measured at least two line scans across dolomite rims and magnesio-calcite. The results are quite similar, independent of deformation mode (**Figure 3.9**). In general, reactants reveal flat profiles with nearly ideal compositions, indicated by normalized mole fractions of $X_{Ca} > 0.99$ ($X_{Ca} = x_{Ca}/[x_{Ca}+x_{Mg}]$) for calcite and $X_{Mg} > 0.99$ ($X_{Mg} = x_{Mg}/[x_{Ca}+x_{Mg}]$) for magnesite, where x_{Ca} and x_{Mg} denote mole fractions of calcium and magnesium, respectively. Within dolomite, however, a gradient in the element distribution is noticeable. Dolomite palisades next to magnesite are characterized by a nearly stoichiometric composition (51 mol% Mg expected for local chemical equilibrium), while granular dolomite next to magnesio-calcite incorporated ≈42 mol% Mg (**Figure 3.9**). Magnesio-calcite grains in contact with this granular calcian-dolomite, also known as protodolomite (e.g., ETSCHMANN ET AL. 2014), incorporated between 16 and 21 mol% Mg. Twisted samples commonly show a higher Mg-content in magnesio-calcite than triaxially compressed samples at similar stresses and temperatures, but within twisted samples no significant difference in Mg incorporation is evident between low and high stress strain conditions (cf., **Figure 3.9 b, c**). At the experimental conditions of $T = 750$°C and $P_c = 400$ MPa, magnesio-calcite is expected to contain 14 mol% Mg in local equilibrium with calcian-dolomite, which may contain up to 48 mol% Mg (HELPA ET AL. 2014). Therefore, the deformed samples close to the phase boundary show an excess solution of Mg in magnesio-calcite and a depletion of Mg in granular dolomite.

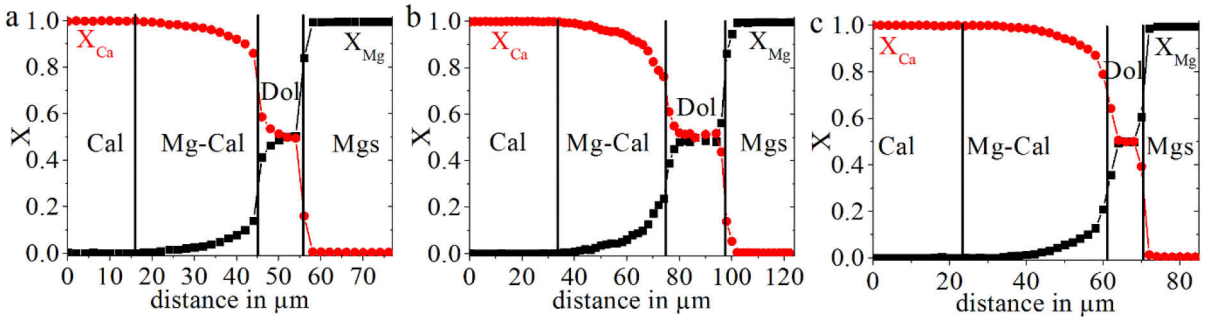

Figure 3.9 Chemical profiles in (**a**) axially compressed sample CaMg-26 ($t = 29$ h, $T = 750$ °C, $\sigma_{ax} = 24$ MPa, $\varepsilon_{ax} = 0.167$) and (**b-c**) twisted sample CaMg-30 ($t = 29$ h, $T = 750$ °C). Stress strain conditions in the central part of sample CaMg-30 are $\sigma_{eq} = 17.5$ MPa, $\varepsilon_{eq} = 0.1$ (**b**) and in the outer part $\sigma_{eq} = 24.1$ MPa, $\varepsilon_{eq} = 2.2$ (**c**). The mole fractions of calcium (X_{Ca}) and magnesium (X_{Mg}) are shown in *red* and *black*, respectively. *Solid vertical lines* indicate locations of phase boundaries.

3.7 Discussion

Deformation experiments performed in this study serve to investigate the influence of stress/strain on dolomite rim growth. The main results can be summarized as follows. At the experimental conditions, the sample stacks showed partitioning of strain into the calcite single crystal, whereas magnesite remained almost undeformed (**Figure 3.2**). The amount of inelastic strain within calcite varies substantially, even under similar stress, temperature and time conditions; accommodated by twinning, subgrain formation, and limited microcracking (**Figure 3.1**; **Figure 3.2**). The reaction rim contains dolomite palisades in contact with magnesite and granular dolomite in contact with magnesio-calcite adjacent to calcite (**Figure 3.3**).

Coaxial deformation reveals no significant change in the dolomite rim and magnesio-calcite width with increasing axial stress (**Figure 3.4 a**). The grain size in both layers is almost constant at different stresses, but increases with time (**Figure 3.4 b, d**). This increase in grain size is larger than in isostatic annealing experiments, particularly for dolomite. The linear increase in dolomite reaction rim layer thickness with the square root of time is similar to that observed in static annealing experiments. At high strain the magnesio-calcite layer thickness growth rate increases and deviates from diffusion-controlled behavior (**Figure 3.4 c**).

In simple shear (torsion) deformation, the thickness of dolomite and magnesio-calcite layers progressively decreases with strain beyond a certain threshold of ≈0.3-0.7 (**Figure 3.5**; **Figure 3.6**). In the low strain center of samples, the dolomite rim is roughly 2 times thicker than the rim measured in axial compression, decreasing by a factor of 3-5 towards the high strain rim. At the same time, the magnesio-calcite layer thickness, which is close to the thickness observed under axial compression, decreases by about 1/3, i.e., less pronounced than for dolomite. In both cases, the decrease in layer thickness is associated with a reduction in grain size by a factor of about 1.3-1.9. Compared to axial compression, the grain size of magnesio-calcite is similar in torsion, but for dolomite it is ≈2 times higher.

Dolomite palisades, which are almost stoichiometric in composition, usually show very limited intracrystalline deformation microstructures, whereas granular dolomite exhibits abundant grain boundary dislocations in axial compression and high strain areas of twisted samples. Close to magnesio-calcite, the dislocation density is very high, accompanied by a Ca-enrichment and the evolution of pores (**Figure 3.7**; **Figure 3.9**). The fraction of subgrains within dolomite increases with strain (**Figure 3.8**). Enhanced dislocation densities are also

evident in magnesio-calcite grains, in particular at grain boundaries and in high strain regions of twisted samples. Compared to isostatic annealing, the magnesio-calcite incorporates more Mg, specifically in torsion deformation and apparently independent of total strain. Also, the texture of deformed samples is less pronounced, but the strength of the CPO increases with applied stress by rotation of the [0001] axis parallel to the growth direction, mainly in granular dolomite (**Figure 3.8**).

In the following, we discuss first the deformation mechanisms and strength of all phases involved and secondly the effect of stress and strain on the chemical composition, reaction progress, and texture evolution of the reactants.

3.7.1 Deformation mechanisms and strength

With respect to the educt phases, magnesite single crystals show almost no evidence of inelastic deformation with the exception of some microcracks. Inelastic deformation of calcite is accommodated by twinning and dislocation creep. Twinning is dominant at low strain and low stresses since the critical resolved shear stress for the initiation of $\mathbf{e}\,\{01\bar{1}8\}\langle 40\bar{4}1\rangle$ twinning is low compared to activation of dislocation glide (DE BRESSER 1991). At higher strain ($\gtrsim$0.08), twin lamellae tend to be broader and slightly curved, indicating a strain dependence on the twin appearance (RYBACKI ET AL. 2013). Deformation zones evolve at a strain of $\gtrsim$0.10, associated with undulose extinction and the formation of low angle boundaries, indicating enhanced dislocation activity.

With respect to the product phases, magnesio-calcite layer deformation also involves twinning and dislocation activity. Twins are rare and only present within large magnesio-calcite grains next to pure calcite. Some grains show relatively straight grain boundaries, equilibrium angles at neighboring grain triple junctions and abundant dislocations, often close to grain boundaries. Weak crystallographic textures of deformed magnesio-calcite may indicate grain boundary sliding (GBS) as an important deformation mechanism (RAJ AND ASHBY 1971; GIFKINS 1976), which agrees with triaxial deformation experiments on polycrystalline magnesio-calcite samples (HERWEGH, XIAO, AND EVANS 2003). HERWEGH, XIAO, AND EVANS (2003) suggested a combination of grain boundary sliding and grain boundary diffusion creep at temperatures between 750 and 800 °C and stresses <40 MPa, almost independent of magnesium content. In the high strain part of twisted samples, magnesio-calcite grains show dislocations walls forming low angle grain boundaries, implying a non-conservative movement

of dislocations via climb. Deformation of the relatively fine grained (2-7 μm) dolomite reaction rim may occur mainly by diffusion creep in palisades and probably in granular dolomite in the low strain inner part of twisted samples, indicated by the low dislocation density and appearance of straight or gently curved grain boundaries. This interpretation fits to other deformation experiments on dolomite. DAVIS, KRONENBERG, AND NEWMAN (2008) observed diffusion creep of fine-grained (2-12 μm) dolomite in triaxial compression experiments at temperatures >700 °C, whereas coarse-grained (240 μm) dolomite deformed by dislocation creep. In the temperature range of 700–1000 °C, HOLYOKE, KRONENBERG, AND NEWMAN (2013) noticed a transition from dislocation creep to diffusion creep at high strain, induced by the development of fine-grained (<10 μm) shear zones associated with strain weakening. In our experiments, however, particularly in dolomite regions of chemical disequilibrium close to magnesio-calcite and those of high stress/strain, grain boundary bulging occurs by the reduction of high dislocation densities along grain boundaries, potentially leading to the observed slight increase of low angle grain boundaries with applied stress (**Figure 3.8 c**).

A very striking observation in our experiments is that at similar applied stresses the resulting strain (-rates) vary significantly between samples, both in torsion and compression tests (**Figure 3.1**). Since most of the measured bulk strain is accommodated by twinning and dislocation creep of calcite, we suggest that the difference in strain (- rates) results from the activation of different slip systems. For the activation of a certain slip system the yield stress (σ_{yield}) must be achieved, which depends on the critical resolved shear stress ($CRSS$) and the Schmid factor (S). Schmid factors are related to the crystallographic orientation of calcite single crystals with respect to the compression axis. Because our samples were cored perpendicular to the $\{10\bar{1}4\}$ rhomb planes, the axial compression axis in triaxial deformation and the rotation axis in torsion tests were oriented perpendicular to one of the three rhomb planes $\mathbf{r_1}$, $\mathbf{r_2}$ or $\mathbf{r_3}$. For compression normal to $\mathbf{r_1}$,the calculated S for twinning and **r**, **f**, and **c**-slip are given in **Table 3.5**, together with the corresponding approximate critical resolved shear stresses ($CRSS$, adopted from DE BRESSER 1991). The resulting yield stresses ($\sigma_{yield}= CRSS/S$) are between 3 and 64 MPa (**Table 3.5**).

type	Slip system	S compression ⊥ r_1	σ_{yield} in MPa
e-twinning			
$\mathbf{e_1}$	$(\bar{1}018)[40\bar{4}1]$	0.3	3
$\mathbf{e_2}$	$(1\bar{1}08)[\bar{4}401]^+$	0	-
$\mathbf{e_3}$	$(01\bar{1}8)[0\bar{4}41]^+$	0	-
r-slip ($CRSS \approx 3$ MPa)			
$\mathbf{r_1}$	$(10\bar{1}4)[\bar{2}021]^+$	0	-
$\mathbf{r_2}$	$(\bar{1}104)[2\bar{2}01]$	0.19	18
$\mathbf{r_3}$	$(0\bar{1}14)[02\bar{2}1]$	0.19	18
f-slip (low T) ($CRSS \approx 15$ MPa)			
$\mathbf{f_1}$	$(\bar{1}012)[2\bar{2}01]^+[02\bar{2}1]^-$	0.24; 0.24	64;64
$\mathbf{f_2}$	$(1\bar{1}02)[\bar{2}021]^+[0\bar{2}21]^-$	0; 0.47	-;32
$\mathbf{f_3}$	$(01\bar{1}2)[\bar{2}021]^+[\bar{2}201]^-$	0; 0.47	-;32
f-slip (high T) ($CRSS \approx 10$ MPa)			
$\mathbf{f_1}$	$(\bar{1}012)[10\bar{1}1]$	0.3	35
$\mathbf{f_2}$	$(1\bar{1}02)[\bar{1}101]$	0.3	35
$\mathbf{f_3}$	$(01\bar{1}2)[0\bar{1}11]$	0.3	35
c-slip ($CRSS \approx 6$ MPa)			
$\mathbf{c_1}$	$(0001)[\bar{1}\bar{1}20]$	0.43	15
$\mathbf{c_2}$	$(0001)[\bar{1}2\bar{1}0]$	0	-
$\mathbf{c_3}$	$(0001)[0\bar{1}\bar{1}0]$	0.43	15

Table 3.5 Schmid factors (S) and approximate yield stresses (σ_{yield}) for activation of **e**-twinning and glide systems in calcite single crystals. Slip systems were reported by WENK (1985) and DE BRESSER (1991). Critical resolved shear stress were calculated after DE BRESSER (1991). Axis of axial compression was constrained to be perpendicular to one of the 3 rhomb planes, resulting in symmetric S factos and σ_{yield}. Positive and negative sense of glide like defined by TURNER, GRIGGS, AND HEARD (1954), are indicated by + or – respectively. Loading was calculated for $[20\bar{2}1]$, $[\bar{2}201]$ and $[0\bar{2}21]$ directions using cell the hexagonal structural cell with a = 4.99 Å and c = 17.06 Å (DEER, HOWIE, AND ZUSSMAN 1992).

In summary, **e** twinning and **c** and **r**-slip are the most likely systems for inelastic deformation, probably assisted **f**-slip at higher stresses. Based on these estimations, we suggest that partial activation of $\mathbf{r}\{10\bar{1}4\}\langle 20\bar{2}\bar{1}\rangle$ and $\mathbf{c}(0001)\langle 2\bar{1}\bar{1}0\rangle$ slip with $\sigma_{yield} \approx$ 15-18 MPa, close to the applied stresses of 17 ± 2 MPa and 23 ± 2 MPa for triaxial compression and torsion, respectively (**Figure 3.1**). This yield stress is responsible for those samples that exhibited high strain. The activation of additional **r**- and **c**-slip systems helps to satisfy the von Mises criterion (activation of 5 independent slip systems) for homogeneous plastic deformation. The interaction of twins and slip systems and the formation of deformation zones and subgrains may also account for the different strains obtained at similar stresses.

Regarding strength of the other phases involved, at the experimental conditions magnesite was stronger than calcite, showing only minor intracrystalline deformation. Magnesite single crystals were deformed by HIGGS AND HANDIN (1959) at temperatures <500 °C and 500 MPa confining pressure, loaded parallel to the **c**-axis. Gliding on **r** was observed even at 25 °C, but no significant flow occurred up to 500 °C. More recently, HOLYOKE ET AL. (2014) investigated the deformation behavior of natural magnesite aggregates in the temperature range of 400 to 1000 °C and strain rates of 10^{-4}-10^{-7} s^{-1}. Tests were conducted on fine-grained (1 µm) magnesite at 300 MPa confining pressure and on coarse-grained (100 µm) magnesite at 900 MPa effective pressure. The authors formulated flow laws for dislocation creep and for diffusion creep of magnesite, revealing that magnesite is stronger than calcite at all experimental conditions. Flow laws for dislocation and diffusion creep of magnesio-calcite were measured by HERWEGH, XIAO, AND EVANS (2003) and XU ET AL. (2009). Diffusion creep appears to be independent of the magnesium content, but for dislocation creep, higher magnesium concentrations increase the strength of magnesio-calcite. Constitutive equations for creep of dolomite in both regimes are provided by HOLYOKE, KRONENBERG, AND NEWMAN (2013), partially based on measurements performed by DAVIS, KRONENBERG, AND NEWMAN (2008) and DELLE PIANE ET AL. (2008).

A comparison of the estimated strength of all phases is shown in **Figure 3.10**, related to the experimental conditions shown in **Figure 3.1**. For calcite, we used the flow laws for single crystals given by DE BRESSER (1991) and for polycrystalline Carrara marble SCHMID, PATERSON, AND BOLAND (1980). The predicted rates for dislocation creep of calcite are in good agreement with the strain rates measured in our axial compression experiments and close to the slowest rates measured in torsion experiments. Note that the single crystal flow law was derived for compression parallel to $[40\bar{4}1]$, not perpendicular to one of the $\{10\bar{1}4\}$ planes as in our study. Plastic deformation of magnesite yields lower strain rates than those of pure calcite, which is in agreement with our observations. The measured dolomite grain sizes predict diffusion creep at rates similar to the bulk (calcite) rates measured in torsion experiments and at higher rates than those measured in axial compression experiments. Magnesio-calcite is predicted to deform by diffusion creep for grain sizes $\lesssim$30 µm or by dislocation creep for larger grain sizes. Note that a decrease in Mg-content leads to slower strain rates for dislocation creep. Here, we plotted the deformation rates for Mg-Cal 80 (≈17 mol% $MgCO_3$), close to the measured Mg-content of $\gtrsim$16 mol% $MgCO_3$ at the dolomite phase boundary (**Figure 3.9**).

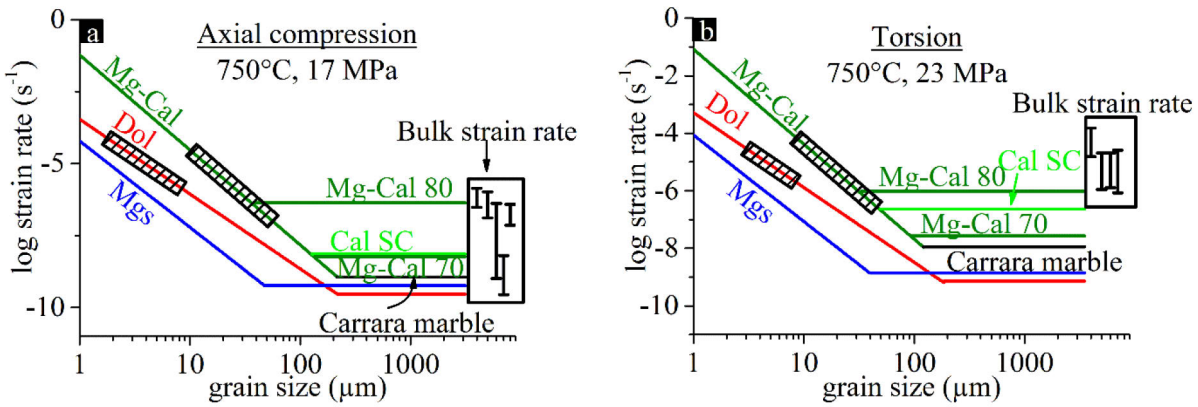

Figure 3.10 Grain size-independent dislocation creep and grain size-dependent diffusion creep of different phases at 750 °C and stresses of 17 MPa (**a**) and 23 MPa (**b**) applied on triaxial compression and torsion experiments, respectively. Measured experimental bulk strain rates with respect to calcite single crystals are indicated within the *black boxes*. Measured grain size (diameter) ranges for dolomite and magnesio-calcite (Mg-Cal) are indicated by *shaded boxes* superimposed on associated flow law predictions. At the prevailing bulk strain rates deformation may be accommodated by diffusion creep of dolomite and magnesio-calcite, and by dislocation creep of calcite single crystals. Flow laws for magnesite are provided by HOLYOKE ET AL. (2014), for dolomite by HOLYOKE, KRONENBERG, AND NEWMAN (2013), for magnesio-calcite (Mg-Cal; Mg-Cal 70/80) by HERWEGH, XIAO, AND EVANS (2003) and XU ET AL. (2009), for calcite single crystals (Cal SC) by DE BRESSER (1991), for Cararra marble by SCHMID, PATERSON, AND BOLAND (1980).

Assuming that the flow laws can be applied to our samples, the products dolomite and magnesio-calcite appear to be weakest phases, preferentially deforming by diffusion creep because of their small grain size. However, we did not observe any strain partitioning into the reaction layers (**Figure 3.2**), although this may be obscured by their small width, composed of just few-grains-thick layers. Therefore, dislocation-accommodated grain boundary sliding with strain rates in between those of dislocation and grain boundary diffusion creep (e.g., HIRTH AND KOHLSTEDT 2003; HANSEN, ZIMMERMAN, AND KOHLSTEDT 2011) may be prevailing in magnesio-calcite and granular dolomite, which agrees with our microstructural and textural observations. In addition, due to end effects the mechanical behavior of thin layers is presumably different than of thick aggregates, which makes application of the flow laws more complicate. For example, frictional sliding effects (JI ET AL. 2000; JI ET AL. 2005) or inhomogeneous stress distributions (e.g., TURNER ET AL. 1954; GÖTZE ET AL. 2010) at contact interfaces will likely influence the deformation behavior and composite strength. On the other hand, any inelastic deformation of dolomite will result in a decrease of the reaction rim thickness in triaxial compression (e.g., by about 10%, if deformed by diffusion creep at a rate of $\approx 10^{-6}$ s^{-1} for 29 h). This may mask the effect of stress on rim growth kinetics and result in an apparently constant or decreasing thickness with increasing stress and time (**Figure 3.4**). It may also explain why the dolomite rims in axial compression are thinner than in the low strain center of twisted samples, where shear deformation prevails.

3.7.2 Effect of stress and strain on chemical composition and reaction rim growth

In our experiments, magnesio-calcite grains show a positive correlation between chemical composition and density of dislocations. For example, grain *I* shown **Figure 3.7 c** contain 1.75 wt.% Mg and $\rho \approx 2.8 \cdot 10^{13}$ m, whereas *II* contains 1.03 wt.% Mg and $\rho \approx 1.4 \cdot 10^{13}$ m^{-2}. For dolomite, we observed that dolomite palisades are stoichiometric with low dislocation densities, indicating thermodynamic equilibrium. Also, granular dolomite next to dolomite palisades exhibits few dislocations and forms equilibrium angles at grain triple junctions (**Figure 3.7**). The boundary between these microstructural domains is interpreted as the initial contact (HELPA ET AL. 2014), so that dolomite grains close to this boundary should have formed first and incorporation of magnesium and ordering should be almost complete, probably by multiple events of chemical reorganization during deformation (MALONE, BAKER, AND BURNS 1996). In contrast, dolomite close to magnesio-calcite reveals a high dislocation density and depletion of the Mg-content (**Figure 3.7**; **Figure 3.9**), because a non-ideal chemical composition is likely to be accommodated by defects in the crystal structure (WENK, BARBER, AND REEDER 1983). MALONE, BAKER, AND BURNS (1996) observed an increase of dolomite lattice parameters with increasing calcium content, leading at $T = 200$ °C to an increase in the dolomite cell volume of about 0.6% for a decrease in Mg component from 48.6 to 46 mol%. This lattice distortion-induced volume change may explain the development of some nano-pores within granular dolomite close to the magnesio-calcite boundary, in conjunction with the pile-up of dislocations (e.g., RYBACKI, WIRTH, AND DRESEN 2010). In addition, pore space may be formed by the negative volume change of ≈12%, induced by the partial reaction at this interface (cf., HELPA ET AL. 2014). Interestingly, a correlation between chemical variation and dislocation distribution within dolomite was also found in isostatic reaction rim experiments (HELPA ET AL. 2014, their sample CaMg-15), similar to our results. This suggests that the defects are induced chemically rather than by the applied external stress. However, twisted samples show higher magnesium concentrations in magnesio-calcite (≈16-21 mol% Mg) than in triaxial compression and isostatic annealing (≈14 mol%; **Figure 3.9**). These values are in agreement with torsion experiments on calcite-dolomite aggregates conducted by DELLE PIANE, BURLINI, AND KUNZE (2009), who measured at $T = 700$ °C and $t = 10$ h an incorporation of ≈20 mol% Mg in deformed calcite and ≈13 mol% Mg in isostatically annealed calcite. Therefore, shear deformation (torsion) appears to promote incorporation of Mg in magnesio-calcite and chemical disequilibrium at the magnesio-calcite/dolomite boundary, compared to coaxial deformation or isostatic pressure. It is

conceivable that this is due to enhanced transport kinetics in torsion tests. Concerning the effect of stress and strain on reaction rim growth, the kinetics may be changed in two ways: by changing the thermodynamic driving force of the reaction or by modifying the microstructure/texture and the associated reaction pathway. The driving force for a reaction under differential stress can be determined from the total Gibb's energy (ΔG_{tot}), which is the sum of the Gibbs free energy of the reaction ($\Delta_r G$) and the stress induced elastic ($E_{el} = \frac{V_m}{2E}\sigma_1^2$) and plastic($E_{pl} = 0.5 V_m \rho G b^2$) strain energy (KELLER ET AL. 2010):

$$\Delta G_{tot} = \Delta_r G + \frac{V_m}{2E}\sigma_1^2 + 0.5 V_m \rho G b^2 \qquad \textbf{(3.5)}$$

where V_m is the molar volume, E is Young's modulus, σ_1 is the maximum compressive stress, ρ is dislocation density, G is shear modulus and b is the length of the burgers vector. For dolomite with V_m= 65.84 $\frac{\mathrm{cm}^3}{\mathrm{mol}}$, $G \approx$ 50 GPa, $E \approx$ 128 GPa (GEBRANDE 1982) and $b \approx$ 7.7 Å (1/3<02$\bar{2}$1>, BARBER AND WENK 2001) we obtain $E_{el} \approx$ $1.2 \cdot 10^{-1}$- $3.7 \cdot 10^{-1}$ J/mol for the stress range in our triaxial experiments of σ_1 = 7-38 MPa. Since TEM investigations revealed quite variable dislocation densities, we estimate an upper bound of $\rho \approx 10^{12}$-10^{14} m^{-2}, yielding a plastic strain energy of $E_{pl} \approx$ $9.8 \cdot 10^{-1}$–98 J/mol. For comparison, at T = 750 °C and P_c = 400 MPa, the Gibbs free energy for the reaction calcite + magnesite → dolomite is -4610 J/mol (HELPA ET AL. 2014). Therefore, the contribution of the elastic strain energy to the total Gibb's energy is about 0.003-0.008% and of the plastic strain energy 0.02-2.1%. This appears to be negligible compared to the free Gibbs energy of the reaction. Accordingly, a stress/strain-induced change of the driving force for dolomite growth can be excluded at our experimental conditions. For comparison, the free Gibbs energy for enhanced spinel formation in between periclase and corundum at T = 1350 °C, P = 0.1 MPa and an uniaxial stress σ_1 = 30 MPa is $\Delta_r G \approx$ -34000 J/mol. In line with the carbonate system, the contributions of elastic and plastic strain energy to the total Gibb's energy are insignificantly small with ≈0.0002% and ≈0.02% (KELLER ET AL. 2010).

The second possibility for changing the reaction rate kinetics by elevated stress or strain is a modification of the microstructure and CPO. This may enhance for example by diffusive mass transfer by incorporation of dislocations and a reduction in grain size and subgrain size. Any change of the grain size or aspect ratio may alter the growth rate if the kinetics were grain boundary-diffusion-controlled. Similarly, any change of the texture by defor-

mation may alter the grain boundary character distribution (GBCD), which describes the amount and type of grain boundaries in a polycrystalline material. Diffusion of species through the reaction layers along new pathways may be enhanced or reduced, depending on the GBCD and the associated diffusion coefficients. The latter effect was, for example, suggested to explain fast spinel growth rates at elevated axial stresses (KELLER ET AL. 2010). Unfortunately, we do not know if grain boundary or volume diffusion predominates in our experiments. From annealing experiments, it is confirmed that mass transfer during dolomite rim growth occurs by counter diffusion of MgO and CaO with diffusion coefficients in between those for pure volume diffusion and grain boundary diffusion (HELPA ET AL. 2014). Also, the diffusivities along specific grain boundary types in dolomite are unknown, so that the discussion of texture and grain size-related changes of reaction growth rates is restricted to qualitative estimates.

For the time series performed at constant axial stress, we measured a parabolic growth behavior for dolomite rims with increasing time giving a similar growth rate as that observed in static annealing tests (**Figure 3.4 c**). However, the increase in grain size with time is more pronounced in deformed samples than in annealed samples (**Figure 3.4 d**). Since one would expect faster growth rates in fine grained material if by grain boundary diffusion predominates, we conclude that volume diffusion in dolomite is effective even at small grain sizes. Another interesting observation is that pre-deformed sample CaMg-31reveals after annealing a dolomite and magnesio-calcite layer thickness of about 1/2 and 4/5 of that measured in conventional annealing experiments, respectively. At the same time, the average dolomite grain size of the pre-deformed sample is 5-6 times smaller than under isostatic conditions and the magnesio-calcite grain size is reduced by about 1/3. The pre-deformed sample stack showed a high density of long twins oriented parallel to the interface and some microcracks within calcite, which possibly acted as fast pathways for diffusion, reducing boundary-normal growth. Consequently, pre-existing damage of the reactant phase may strongly affect the reaction kinetics, even at isostatic pressure.

In the central part of most twisted samples the dolomite layer thickness is about two times thicker than in triaxially compressed samples. As mentioned above, this may reflect an axial shortening process in triaxial compression that does not occur in torsion. Since the grain size of twisted dolomite is roughly twice the grain size measured in axial compression, predominantly volume diffusion is expected here. The observed CPO development is remarkably similar to the CPO development of fine-grained dolomite in torsion experiments at $T = 600$–

800 °C (DELLE PIANE ET AL. 2008). There dolomite deforms in a linearly viscous manner with evidence for GBS accommodated by dislocation activity.

Another striking observation is the reduction of dolomite and magnesio-calcite layer thickness in the high strain portion of twisted samples (**Figure 3.5**; **Figure 3.6**). Simultaneously with reduction in layer thickness, grain size is also reduced towards the high strain region of the rim. The reduced grain size at high strain may result from abundant nucleation sites. In addition, ongoing grain rotation within the calcite educt phase will possibly slow down the mass transport necessary for the product phase formation.

3.8 Geological implication

In nature, the interplay of metamorphic reactions and deformation is of great importance (e.g., RUBIE 1983; BRODIE AND RUTTER 1985). The small grain size of reaction products can result in a switch from grain size insensitive to grain size sensitive creep associated with strain localization and weakening within reaction zones (e.g., FITZ GERALD AND STÜNITZ 1993; FURUSHO AND KANAGAWA 1999; NEWMAN ET AL. 1999; BURLINI AND BRUHN 2005) Evolution of the reaction product layers can be influenced by pinning of grain boundaries due to secondary phases and/or ongoing recrystallization during deformation (HERWEGH ET AL. 2011). Both processes may inhibit grain growth and promote further strain localization (KRUSE AND STÜNITZ 1999). Ongoing strain localization and mineral reaction may be facilitated by fluid infiltration as observed in natural systems (e.g., WHITMEYER AND WINTSCH 2005). Since carbonates are present in a broad range of environments, their behavior is of great interest in the formation of mylonitic shear zones and subduction zones (HOLYOKE, KRONENBERG, AND NEWMAN 2013; HOLYOKE ET AL. 2014).

In this study, we observed the formation of fine-grained polycrystalline dolomite and magnesio-calcite in between single crystals of calcite and magnesite during deformation. In coaxial deformation, no pronounced strain partitioning and no significant influence of axial stress on the reaction kinetics of dolomite was recognized. This was also observed during torsion tests. These results suggest that the weakening effect of reaction-induced dolomite formation is subordinate in deforming dry natural coarse-grained carbonate systems. However, the magnesio-calcite layer showed a slightly enhanced growth rate at high strains, which is in line with results of other experimentally investigated systems (e.g., HOLYOKE AND TULLIS 2006; DE RONDE AND STÜNITZ 2007) and in natural shear zones (TERRY AND HEIDELBACH

2006). Interestingly, a gradual decrease in dolomite and magnesio-calcite layer thickness was observed at high strain (-rate) in simple shear (torsion) experiments, which may be related to kinetic constraints.

3.9 Conclusion

The influence of non-isostatic stress and strain conditions on dolomite reaction rim growth was investigated by triaxial compression and torsion tests at T = 750 °C and P_c = 400 MPa. During deformation, a fine-grained, polycrystalline dolomite reaction rim and layer of large magnesio-calcite grains evolved at the contact interface of oriented magnesite and calcite single crystals. The microstructure of dolomite reaction rims is characterized by palisade-shaped grains growing into magnesite and granular grains next to calcite.

Most of the bulk deformation is accommodated by calcite single crystals, whereas magnesite remains almost undeformed. At constant applied stress the resulting strain (-rates) varies substantially, likely induced by partial activation of the $\mathbf{r}\{10\bar{1}4\}\langle 20\bar{2}\bar{1}\rangle$ and $\mathbf{c}(0001)\langle 2\bar{1}\bar{1}0\rangle$ slip systems. Microstructural observations suggest that the fine-grained dolomite reaction rim deforms mainly by diffusion creep, partly combined with high dislocation activity in the granular part. Progressive Ca enrichment towards the magnesio-calcite boundary is associated with an enhanced dislocation density in the granular dolomite that helps to accommodate the lattice distortion. Magnesio-calcite grain size increases from the dolomite rim towards pure calcite associated with decreasing magnesium content. Diffusion creep and/or grain boundary sliding predominates in small grains assisted by twinning and dislocation creep in larger grains. The texture of dolomite and magnesio-calcite appears to be slightly stronger at elevated axial stress, resulting in a rotation of [0001] axes parallel to the compression/rotation axis and poles of $\{2\bar{1}\bar{1}0\}$ and $\{10\bar{1}0\}$ prismatic planes parallel to the reaction interface. In contrast, the fraction of low angle boundaries does not change significantly with stress, but increases with strain.

At the experimental conditions, the dolomite rim growth kinetics are diffusion-controlled and independent of the applied axial stress and strain in triaxial compression. This is in agreement with thermodynamic calculations indicating that the stress/strain-induced change in the driving force for dolomite growth is negligible. In contrast, the magnesio-calcite layer thickness increases at high strain, probably by providing fast diffusion pathways through

activation of additional slip planes and accompanied elevated dislocation density within the calcite reactant. However, existing flow laws suggest that the product phases are relatively weak and may have slight flattening during growth, resulting in apparently constant growth kinetics. In twisted samples, reaction product layers decrease almost linearly with strain above a critical value of ≈0.3-0.6. The simultaneous decrease of grain size indicates preferential volume diffusion, which is likely reduced at high shear strain rates by deformation of the minerals.

3.10 Acknowledgments

We are grateful to P. Jeřábek for discussions, S. Gehrmann for sample preparation, M. Naumann for technical support with the Paterson apparatus and R. Wirth for help with the TEM. Caleb Holyoke and two other anonymous reviewers are thanked for their valuable comments and suggestions. This work was funded by the Deutsche Forschungsgemeinschaft within the framework of FOR 741, project RY 103/1-1, which is gratefully acknowledged.

4 Influence of grain size, water and deformation on dolomite reaction rim formation

4.1 Abstract

Solid-solid mineral reaction rates are influenced by the microfabric of reactant phases and concurrent deformation by providing different diffusion pathways. To gain information about this interplay in carbonate systems, we performed annealing and deformation experiments on polycrystalline and single crystal calcite and magnesite, forming dolomite (Dol) and magnesio-calcite (Mg-Cal). At a fixed temperature of T = 750 °C and a confining pressure of P = 400 MPa, sample stacks were either annealed for 29 h, deformed in triaxial compression or torsion for 18 h using a Paterson-type gas deformation apparatus. At the contact interface of starting reactants, Dol reaction rims and polycrystalline Mg-Cal layers formed. The width of the layers varied between 4-117 µm and 5-57 µm, depending on the microstructure of starting materials and experimental conditions. Annealing experiments with polycrystalline reactants in contact with each other resulted in ~22 times thicker Dol rims compared to two single crystals in contact and ≈5 times larger Mg-Cal layer width. Consequently, the microstructure of magnesite is rate-limiting for the reaction front migration. Between polycrystalline starting materials, axial stress has a slight retarding effect on Dol growth rates (≈-20%) and an accelerating effect on Mg-Cal growth kinetics (≈+50%). For torsion experiments at ≈2 MPa shear stress, almost the same trend is observed, independent of strain. Highly strained torsion samples show Dol formation along grain boundaries in Mg-Cal and in the polycrystalline calcite reactant, indicating enhanced grain boundary diffusion at high strain rates. The reduction of Dol rim thickness between polycrystalline reactants is possibly caused by concurrent grain coarsening of polycrystalline magnesite, slowing down the grain boundary diffusion rate. Adding water of ~0.3 wt.% revealed no change of Dol and Mg-Cal growth kinetics between single crystals.

The experiments demonstrate that Dol reaction kinetics strongly correlate with magnesite grain sizes, while deformation enhances Mg-Cal production. Therefore in nature, we would expect fastest reaction progress for Dol and Mg-Cal in environments of very fine-grained reactants in association with deformation.

4.2 Introduction

In nature, metamorphic rocks often exhibit deformation and mineral reactions at the same time (e.g., RUBIE 1983; RUTTER AND BRODIE 1988; NEWMAN ET AL. 1999) and reference therein). Evidence for the concurrent occurrence of these processes is well documented in natural mylonites (RUBIE 1983; FITZ GERALD AND STÜNITZ 1993; NEWMAN ET AL. 1999; TSURUMI, HOSONUMA, AND KANAGAWA 2003). Neocrystallization of fine-grained reaction products may allow a change in deformation mechanism from grain size insensitive dislocation creep to grain size sensitive diffusion creep and/or grain boundary sliding, facilitating strain localization (KERRICH ET AL. 1980; RUBIE 1983).

In recent years, many experimental studies have been performed in several systems addressing syn-deformational reactions. For example plagioclase-olivine forming spinel + clinopyroxene + orthopyroxene (DE RONDE ET AL. 2004; DE RONDE ET AL. 2005; DE RONDE AND STÜNITZ 2007) biotite + plagioclase + quartz forming garnet + K-feldspar + water (HOLYOKE AND TULLIS 2006) and dolomite decomposition to periclase + CO_2 (DELLE PIANE, BURLINI, AND GROBETY 2007). In all experiments enhanced reaction rates in deformed samples were observed compared to static conditions. Deformed samples with concurrent reaction progress showed strain weakening due to a change in deformation mechanism from dislocation creep to diffusion creep, similar to observations in naturally deformed samples.

In silicate systems, the presence of water at grain boundaries can considerably enhance mineral reaction rates (e.g., GARDÉS ET AL. 2012), probably assisted by fast diffusion through fluid-filled pore channels (MILKE ET AL. 2013). Small amounts of water accelerates also the deformation rate of silicates, for example in olivine (MEI AND KOHLSTEDT 2000A; MEI AND KOHLSTEDT 2000B; KARATO AND JUNG 2003; HIRTH AND KOHLSTEDT 2003), pyroxene (DIMANOV AND DRESEN 2005; HIER-MAJUMDER, MEI, AND KOHLSTEDT 2005), feldspar (RYBACKI AND DRESEN 2000; RYBACKI AND DRESEN 2004; RYBACKI ET AL. 2006) and quartz (POST, TULLIS, AND YUND 1996; HIRTH, TEYSSIER, AND DUNLAP 2001; RUTTER AND BRODIE 2004). In contrast, the effect of water on deformation in carbonate systems is minor (DE BRESSER, URAI, AND OLGAARD 2005).

Here, we focus on the calcite ($CaCO_3$) – magnesite ($MgCO_3$) carbonate system, forming a solid solution of dolomite ($CaMg(CO_3)_2$). Preceding experiments on calcite and magnesite single crystals under isostatic and non-isostatic conditions revealed diffusion-controlled dolomite reaction rim growth, which was almost unaffected by applied axial stresses up to 38 MPa, but gradually reduced at high strain rates (HELPA ET AL. 2014; HELPA ET AL. 2015).

Annealing and deformation experiments were performed on single crystal and polycrystalline starting materials to determine the effect of microstructure on the mineral reaction rates. In addition we examined the effect of water on dolomite formation.

4.3 Materials and experimental methods

4.3.1 Starting materials

In this study, we used natural single crystals and polycrystalline calcite and magnesite for the starting assembly. Calcite (Brazil, Minas Gerais) and magnesite (Brazil, Bahia Brumado) single crystals were optically clear with a rhombohedral habit. Chemical compositions of single crystals were obtained by 8-10 point measurements using a field-emission electron microprobe (JEOL JXA-8500 F HYPERPROBE) at 15 keV accelerating voltage, 5 nA beam current, and 15 µm beam diameter with a counting time of 20 s on peak. Results confirmed relatively pure single crystals except some minor amounts of 0.17 wt.% Ba in calcite as well as 0.15 wt.% Fe and 0.23 wt.% Ca in magnesite.

For experiments with polycrystalline starting material, Solnhofen limestone (Germany), Lorrano Bianco marble (Italy, Carrara) and magnesite from Zimbabwe (Africa) were used. Average grain sizes and porosities were determined by the line-intercept method. Mineralogical composition of polycrystalline starting materials was determined by powder X-ray diffraction (XRD) using a STOE Stadi P diffractometer with CuKα radiation (λ = 1.5405 Å). Data were collected from 5 to 125 ° 2θ, at a counting rate of 0.01 ° 2θ s^{-1}. Water contents of the starting materials were estimated using a Vario EL III element analyzer (Elementar Analysesysteme GmbH).

Solnhofen limestone with an average grain size of 6 ± 1 µm and 4% porosity is composed of 80% pure calcium carbonate and 20% of $Ca_{0.97}Mg_{0.03}CO_3$. The measured water content ranges between 0.4 and 0.58 wt.%. Cararra marble is composed of >99% calcite with a porosity of <0.5%, a random crystallographic preferred orientation (CPO) and an average grain size of 220 ± 40 µm (RYBACKI ET AL. 2013). The estimated water content is ≈0.6 wt.%. Polycrystalline magnesite is fine-grained (4 µm) with a porosity of 6%. It is composed of 92 wt.% Mg and 8 wt.% Ca with 0.4-0.58 wt.% water.

Sample assemblies were composed of various stacks of starting material cylinders with 7 mm diameter and 2.5-4.8 mm length. Single crystal cylinders were cored and polished

perpendicular to the natural cleavage planes and Solnhofen limestone cylinders were cored perpendicular to the bedding. Solnhofen limestone shows a weak initial CPO with by **c**-axes oriented parallel to the bedding plane (LLANA-FUNEZ AND RUTTER 2014). To evaluate the effect of starting material microstructure on reaction progress in a single run, we stacked single crystal and polycrystalline cylinders in different combinations (**Table 4.1**). In the following we will use abbreviations as defined in **Table 4.1.**

Experiment	Starting assembly	t (h)	Strain	Strain rate (s^{-1})	Stress (MPa)
annealing			ε	$\dot{\varepsilon}$	σ_{max}
Stack-01	Soln/Mgs/Cal /poly-Mgs/Soln	29	-	-	-
pCa_Mg_pCac-01	Soln/Mgs/Carrara	29	-	-	-
Ca_Mg_Dia-01	Mgs/Cal	29	-	-	-
pCa_pMg_pCac-01	Soln/poly-Mgs/Carrara	29	-	-	-
Triaxial					
Ca_pMg_pCa_Mg-01	Cal/poly-Mgs/Soln/Mgs	18	0.17	$1 \cdot 10^{-4}$	20 (for 0.5 h)
Torsion			γ	$\dot{\gamma}$	τ_{max}
pCa_pMg-01	Soln/poly-Mgs	18	2	$3.1 \cdot 10^{-5}$	3.8 ± 0.5
Ca_pMg-02	Cal /poly-Mgs	18	4	$6.2 \cdot 10^{-5}$	1.7 ± 0.4

Table 4.1 Starting material assemblies (from top to bottom) and experimental conditions. All experiments were performed at 750 °C temperature and 400 MPa confining pressure. t is time, ε is bulk axial strain and $\dot{\varepsilon}$ is the strain rate measured in triaxial compression at constant axial stress σ_{max}. τ_{max}, is the maximum shear stress and γ is the maximum shear strain obtained in torsion experiments at constant shear strain rate $\dot{\gamma}$. Note: Soln = Solnhofen limestone, Mgs = magnesite single crystal, Cal = calcite single crystal, poly-Mgs = polycrystalline magnesite, Carrara = Carrara marble.

4.3.2 Experimental procedure

All experiments were performed using a Paterson type gas-deformation apparatus at a fixed temperature of T = 750 °C, a confining pressure of P_c = 400 MPa and run durations of t = 18 h for triaxial compression and torsion experiments, and 29 h for static annealing experiments (**Table 4.1**). Shorter run durations for deformation experiments were chosen because of the relatively fast deformation of polycrystalline starting materials. Nevertheless, a run duration of 18 h ensures a direct comparison with results of dolomite rim growth in between Cal and Mgs during deformation (HELPA ET AL. 2015). Each specimen stack was sandwiched between ≈2 mm thick aluminum oxide spacers and pistons. The entire stack was jacketed by cooper sleeves with a thickness of ≈0.65 mm, to prevent intrusion of the (argon) confining pressure medium. Samples were heated at a rate of 20 °C/min to the target temperature and cooled with 2 °C/min after the run duration. Temperature was monitored by a Pt-Pt/13%Rh (R-type)

thermocouple located 3 mm away from the assembly.

Three annealing experiments were performed on different reactant stacks using samples with as-is water content. In addition, one annealing experiment was done with a modified assembly (Ca_Mg_Dia-01) to examine the role of water on mineral reaction between two single crystals. A borehole of 2.3 mm diameter was drilled in the center of the Mgs parallel to the cylindrical axis and filled with diaspore (AlOOH). At the confining pressure of 400 MPa diaspore dehydrates to corundum (Al_2O_3) at $T \approx$ 420 °C (HAAS 1972), releasing ≈15 wt.% H_2O.

One triaxial compression experiment was conducted at constant stress of σ = 20 MPa allowing to investigate the effect of coaxial stress on the rim growth behavior. After yielding, the sample stack deformed at a bulk rate of about $1 \cdot 10^{-4}$ s^{-1} to a bulk strain of 0.17 within ≈0.5 h duration. Subsequently, the assembly was annealed for 17.5 h to allow comparison to torsion tests. To evaluate the influence of high strain deformation on reaction, two torsion experiments were performed at a constant twist rate of $\approx 7 \cdot 10^{-5}$ s^{-1} to maximum shear strains at the cylinder periphery of γ = 2 and 4 (**Table 4.1**). Since deformation was mainly partitioned into the (weak) polycrystalline reactant phases, here strain is referred to the length of the corresponding starting samples. For determination of maximum shear stress from measured torque, we expected power law creep behaviour with a stress exponent of 1.66 and 1.1 for Soln limestone and poly-Mgs, respectively (SCHMID, BOLAND, AND PATERSON 1977; HOLYOKE ET AL. 2014). For experiment pCa_pMg-01 with polycrystalline starting materials, the shear stress was 1.7 ± 0.4 MPa up to a shear strain of 0.6, followed by strain hardening to a maximum shear stress of 3.8 ± 0.5 MPa at γ = 2, whereas for experiment Ca_pMg-02 with Cal and poly-Mgs as starting materials the shear stress of 1.7 ± 0.4 MPa was constant up to γ = 4. In this high strain experiment, wrinkles on the copper jacket indicate partial deformation of the Cal (≈0.5 mm wide), associated with twins and cracks orientated parallel to natural cleavages.

Mechanical data were corrected for the strength of the copper jackets and system compliance. The reported error of stress results from uncertainty in jacket strength. After experiments, sample assemblies were cut along the cylindrical axis, embedded in epoxy and polished for analysis of the reaction products. In addition, tangential thin sections were prepared from twisted samples, cut parallel to the cylindrical axis close to the outer periphery.

4.3.3 Analytical methods

Reaction product thicknesses and grain size were analyzed using an optical microscope (Leica DM RX) with an attached high-resolution digital camera (Leica DFC 420). For determination of rim/layer thickness, a set of reflected-light micrographs along the reaction interface was collected and phase boundaries were redrawn by hand. Samples deformed in torsion were cut parallel to sample axis at the outer periphery to produce tangential thin sections. In experiments with polycrystalline starting material, phase boundaries were identified petrographically by a change in microstructure and/or grain sizes. The average reaction layer thicknesses were calculated from digitized traces of the entire phase boundaries. Grain sizes of reaction products were estimated by measuring the size of 50 individual grains within each layers and subsequently averaged (JOACHIM ET AL. 2010).

Using an electron microprobe, the distributions of major elements Ca (Kα, PETJ) and Mg (Kα, TAP) across the reaction products were investigated. Line scans of wavelength dispersive X-ray analyses were collected at an accelerating voltage of 15 keV, a beam current of 2 nA and a counting time of 20 s on each peak. To avoid damage of the carbonates, a beam diameter of 2 µm and a step size of 2 µm were used for point measurements. Crystallographic orientation relations between reactants and reaction products were investigated by a combination of electron backscatter diffraction (EBSD, TSL DigiView) and semi-quantitative energy dispersive spectroscopy (EDS). Operating details and evaluation procedures are described by HELPA ET AL. (2014).

4.4 Results

In all experiments a coarse-grained magnesio-calcite (Mg-Cal) layer next to a calcite reactant and a subsequent fine-grained dolomite (Dol) reaction rim evolved at the initial contact interface of starting reactants. The microstructures and layer thicknesses of reaction products strongly depend on starting material microstructure.

Experiment	interfaces	t (h)	Δx_{Dol} (μm)	$\Delta x_{Dol-Mgs}$ (μm)	$\Delta x_{Dol-Cal}$ (μm)	Δx_{Mg-Cal} (μm)	$a_{Dol-Mgs}$ (μm)	$a_{Dol-Cal}$ (μm)	a_{Mg-Cal} (μm)
annealing									
Stack-01	Soln/Mgs	29	5 ± 1	NA	NA	30_a	NA	NA	NA
	Mgs/Cal		47 ± 11	24 ± 6	23 ± 6	41 ± 9	5.0 ± 1.1	4.5 ± 1.0	24.3 ± 13.4
	Cal/poly-Mgs		98 ± 7	46 ± 6	51 ± 4	52 ± 7	6.9 ± 1.3	6.7 ± 1.6	28.4 ± 11.7
	poly-Mgs/Soln		108 ± 8	49 ± 6	59 ± 6	130 ± 13	6.3 ± 1.1	5.7 ± 1.0	20.9 ± 9.4
pCa_Mg_pCac-01	Soln/Mgs	29	5 ± 1	NA	NA	30_a	NA	NA	NA
	Mgs/Carrara		9 ± 2	5 ± 1	4 ± 1	29 ± 8	2.1 ± 0.5	2.3 ± 0.7	17.1 ± 10.8
Ca_Mg_Dia-01	Mgs/Cal	29	14 ± 4	9 ± 2	6 ± 2	37 ± 10	4.5 ± 1.5	4.2 ± 1.6	23.5 ± 14.3
pCa_pMg_pCac-01	Soln/poly-Mgs	29	117 ± 7	57 ± 5	59 ± 5	147 ± 14	6.6 ± 1.6	5.7 ± 1.6	21.3 ± 8.4
	poly-Mgs/Carrara		108 ± 5	50 ± 5	59 ± 3	65 ± 10	6.7 ± 1.8	5.4 ± 2.0	24.0 ± 16.1
Triaxial									
Ca_pMg_pCa_Mg-01	Cal /poly-Mgs	18	65 ± 4	33 ± 3	32 ± 3	43 ± 5	5.4 ± 1.3	5.0 ± 1.3	23.6 ± 11.5
	poly-Mgs/Soln		67 ± 4	32 ± 4	35 ± 4	69 ± 9	6.0 ± 1.7	4.9 ± 1.0	21.3 ± 7.2
	Soln/Mgs		4 ± 1	NA	NA	32_a	NA	NA	NA
Torsion									
pCa_pMg-01	Soln/poly-Mgs	18	47 ± 6	22 ± 3	25 ± 4	70 ± 19	6.5 ± 2.2	6.4 ± 2.2	18.4 ± 9.2
Ca_pMg-02	Cal /poly-Mgs	18	48 ± 6	22 ± 4	26 ± 5	53 ± 9	5.9 ± 1.9	6.3 ± 1.9	24.5 ± 14.9

Table 4.2 Measured average layer thicknesses of the entire polycrystalline dolomite (Δx_{Dol}), dolomite in contact with magnesite ($\Delta x_{Dol-Mgs}$), dolomite in contact with magnesio-calcite ($\Delta x_{Dol-Cal}$) and magnesio-calcite (Δx_{Mg-Cal}). The mean grain diameters of the dolomite and magnesio-calcite grains are represented by $a_{Dol-Mgs}$, $a_{Dol-Cal}$, and a_{Mg-Cal}. Note: The lower subscript a denotes thicknesses estimated by petrographically observations together with microprobe analyses. NA denotes "Not Available".

4.4.1 Thickness of reaction products

The measured Dol rim and Mg-Cal layer thickness and grain size of all experiments are summarized in **Table 4.2**. During annealing, the thickness of reaction layers is considerably higher for polycrystalline than for single crystal starting materials (**Figure 4.1**).

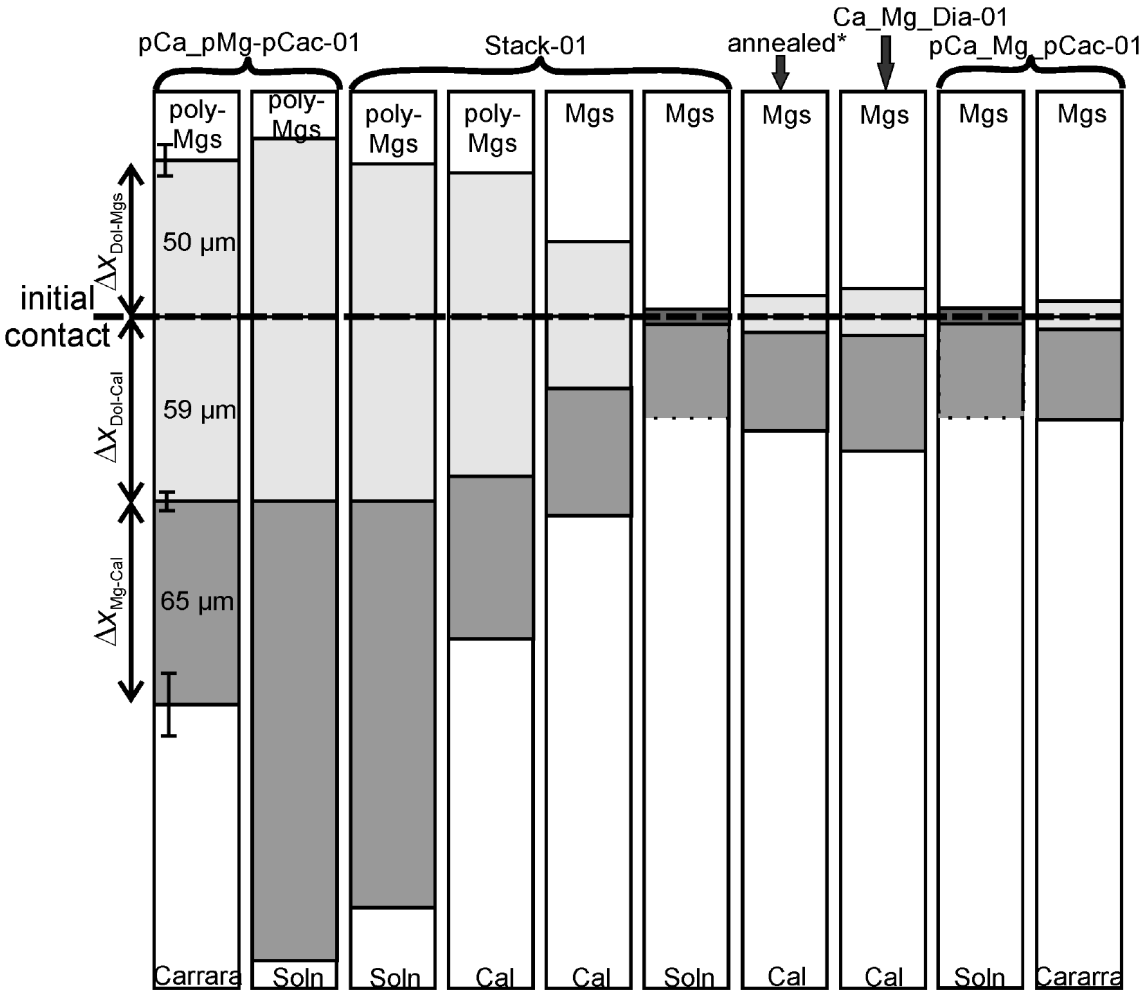

Figure 4.1 Schematic diagram of reaction product widths in samples annealed for 29 h. Width of the entire dolomite reaction rim Δx_{Dol} (*light grey*) and magnesio-calcite layer Δx_{Mg-Cal} (*intermediate grey*) are given between different starting materials (top and bottom). The *dashed line* represents the initial contact of starting materials. *Dark grey* boxes indicate dolomite rims, where no initial contact interface could be estimated. In the first column measured values are listed and uncertainties are given by error bars at phase boundaries. Following columns are normalized with respect to the first column. Measurements of the corresponding experiments are from **Table 4.2**. Asterisk (*) indicates annealing experiment performed by HELPA ET AL. (2014).

For example, in sample stack-01 the entire Dol layer thickness ($\Delta x_{Dol} = \Delta x_{Dol-Cal} + \Delta x_{Dol-Mgs}$) is nearly twice the size when two polycrystalline reactants are used instead of two single crystals, leading to $\Delta x_{Dol} \approx 108$ µm compared to $\Delta x_{Dol} \approx 47$ µm (**Figure 4.1**). For the

Mg-Cal layer thickness, a similar trend is obvious with $\Delta x_{Mg-Cal} \approx$ 130 µm and $\Delta x_{Mg-Cal} \approx$ 41 µm for polycrystalline and single crystal reactant phases, respectively. Using combinations of polycrystalline and single crystal starting materials yields remarkably different results. Poly-Mgs in contact with Cal results in a Dol rim thickness of $\Delta x_{Dol} \approx$ 98 µm, but a Mg-Cal layer thickness of only $\Delta x_{Mg-Cal} \approx$ 52 µm. The latter is only half as wide as measured between two polycrystalline starting materials. The smallest Dol rim of $\Delta x_{Dol} \approx$ 5 µm was measured between Soln in contact with a Mgs (**Figure 4.1**).

Experiment pCa_Mg_pCac-01 shows a similar result for Dol ($\Delta x_{Dol} \approx$ 5 µm) produced between Soln and Mgs, but a thicker Dol rim of $\Delta x_{Dol} \approx$ 9 µm when coarse-grained Carrara is used instead of fine-grained Soln (**Figure 4.1**). Carrara in contact with poly-Mgs (experiment pCa_pMg_pCac-01) yields approximately the same Dol rim width as obtained between Soln and poly-Mgs (108-117 µm), but a different width of Mg-Cal. In between Carrara and poly-Mgs the Mg-Cal layer is ~65 µm thick, while it ranges between 106–147 µm when a Soln and poly-Mgs is used (cf. **Table 4.2**; **Figure 4.1**). The thicknesses of Dol and Mg-Cal for Mgs in contact with Carrara are ≈9 µm and 30 µm. This is roughly comparable to the results obtained between single crystals ($\Delta x_{Dol} \approx$ 13 µm and $\Delta x_{Mg-Cal} \approx$ 32 µm, HELPA ET AL. 2014, **Figure 4.1**). Excess water provided by dehydration of diaspore (experiment Ca_Mg_Dia-01) yields comparable results for two single crystals in contact ($\Delta x_{Dol} \approx$ 14 µm and $\Delta x_{Mg-Cal} \approx$ 37 µm). However, between the Mgs and Cal of sample stack-01 the layers are distinctly thicker with ($\Delta x_{Dol} \approx$ 47 µm and $\Delta x_{Mg-Cal} \approx$ 41 µm).

The effect of deformation on reaction progress is shown in **Figure 4.2**. As for the annealing experiments, the layer thicknesses are much thicker for poly-Mgs compared to Mgs, but they are hardly affected if the Cal is used instead of poly-Cal (**Table 4.2**). However, the reaction layer width obtained in triaxial compression leads to thinner Dol rims if poly-Mgs is used. For direct comparison of the deformation experiments with those of annealed samples, Dol rim and Mg-Cal layer widths were back-calculated from run durations of t = 29 h to t = 18 h. Expected values for the Dol rims were derived assuming a parabolic rim growth behavior. Since the Mg-Cal layer does not grow linearly with the square root of time initially, growth rates reported by HELPA ET AL. (2014) for Mg-Cal layer growth between single crystals were used to determine expected layer widths. Thus, the entire Dol rim thickness between poly-Mgs and a Cal is only ~65 µm in deformed samples compared to ~77 µm in annealed samples after 18 h. For the Mg-Cal layer, widths are similar with ~43 µm. In between poly-

Mgs and fine-grained Soln the effect is more pronounced with thicknesses of ~67 µm and ~85 µm for the triaxially compressed sample compared to the annealing experiment. However, the Mg-Cal layer is significantly larger in deformed samples with $\Delta x_{Mg-Cal} \approx$ 69 µm, compared to the expected of $\Delta x_{Mg-Cal} \approx$ 46 µm for static annealing. Starting with two single crystal reactants, no influence of deformation was observed on the reaction product growth. The same Dol rim thickness of $\Delta x_{Dol} \approx$ 4 µm, and similar Mg-Cal layer thicknesses between 27 and 32 µm were observed between Mgs and Soln.

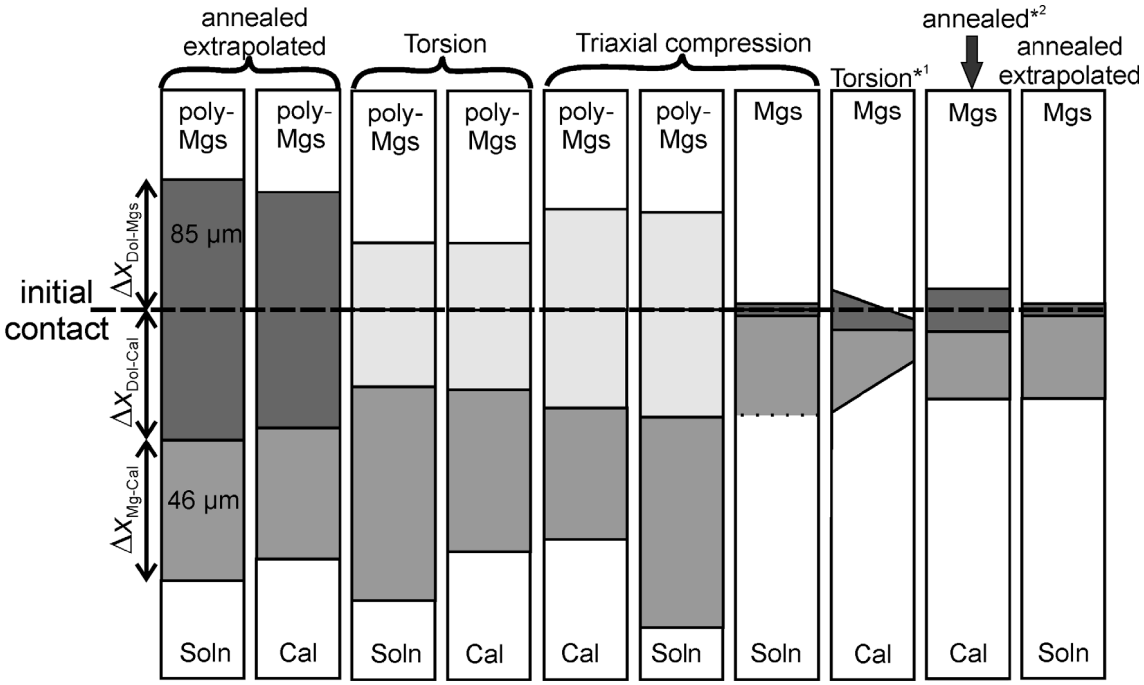

Figure 4.2 Schematic diagram of reaction product width in samples deformed over 18 h. For detailed information, see **Figure 4.1**. Asterisks (*) indicates results of 1) torsion experiment by HELPA ET AL. (2015) and 2) annealing test perfomed by HELPA ET AL. (2014). In torsion test of HELPA ET AL. (2015), a decrease in of Dol rim Mg-Cal layer thickness was observed with increasing strain.

High strain torsion experiments compared to low strain axial compression showed that the width of Dol rims between Soln and poly-Mgs is reduced by 30% in torsion, whereas the Mgs-Cal layer is not affected. Similarly, in torsion a reduction of Δx_{Dol} between Cal and poly-Mgs is observed, but an increase of 23% for the Mg-Cal layer thickness.

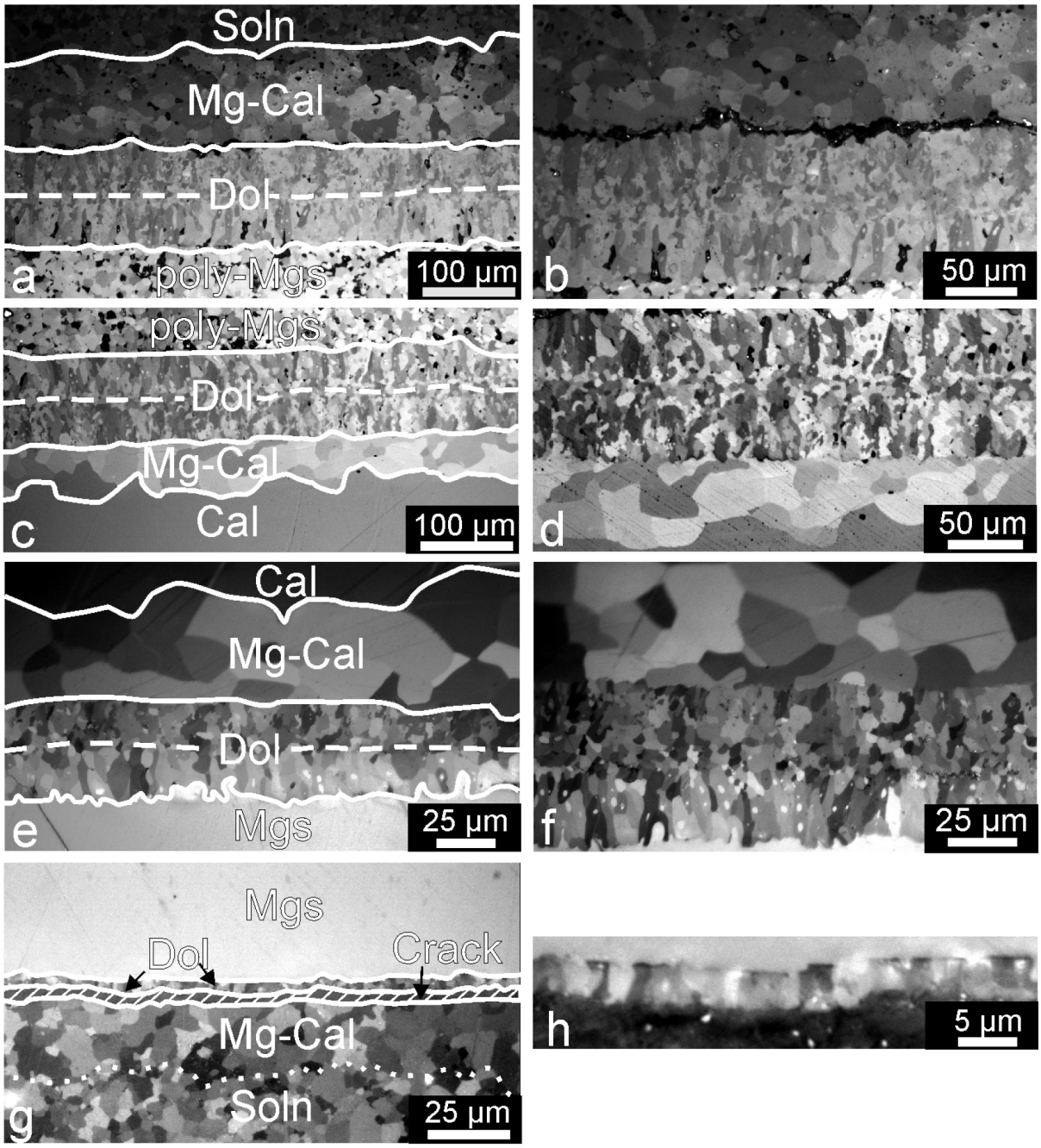

Figure 4.3 Optical micrographs of Dol and Mg-Cal between different starting materials formed during static annealing at 750 °C for 29 h in stack-01. Images in the left column show reaction products in between reactant phases. Phase boundaries are retraced by *solid lines* and the initial contact of starting material is indicated by the *dashed lines*. *Dotted line* in (**g**) indicates the petrographical boundary between Mg-Cal and Soln. In the right column corresponding close-ups of the Dol microstructures are shown. Note different scales.

4.4.2 Microstructures of reaction products

4.4.2.1 Static annealing microstructures

Dol rims produced between polycrystalline starting materials are composed of elongated grains on both sides of the initial contact interface, oriented perpendicular to the reactant phases (**Figure 4.3 a-b**). The initial interface is estimated from the presence of granular Dol just a few grains in thickness, located at the center of the Dol rim (**Figure 4.3 b**). This microstructural boundary within Dol is comparable to the boundary between elongated and granular Dol at the initial interface observed in annealing experiments of single crystal starting materials (HELPA ET AL. 2014). Elongated Dol grains in contact with poly-Mgs show slightly curved grain boundaries and contain isolated inclusions of magnesite. Boundaries of Dol grains next to Mg-Cal are often irregular in shape with little or no evidence of inclusions. Large Mg-Cal grains show curved boundaries with low porosity, often associated with Dol formation.

The microstructure of Dol between poly-Mgs and Cal educt reactants is quite similar (**Figure 4.3 c-d**). The Mg-Cal layer is composed of small numbers of large grains with curved boundaries and no porosity (**Figure 4.3 c-d)**.

Dol grown between two single crystals shows two distinct microstructural domains (**Figure 4.3 e-f**). Elongated, palisade-shaped Dol grains growing into magnesite are characterized by relatively straight grain boundaries often containing inclusions of magnesite. In the center of the rim, Dol grains are equiaxed with slightly curved but regular grain boundaries, which are more irregular next to Mg-Cal. Large Mg-Cal grains increase in size from the Dol boundary towards pure Cal with mostly straight or gently curved grain boundaries, often forming 120° triple junctions. The microstructures of Dol and Mg-Cal that evolved between single crystals at water saturated conditions due to dehydration of diaspore (experiment Ca_Mg_Dia-01) are quite similar, albeit with more irregular grain boundaries in both Dol domains.

Microstructures of Dol in the thin, often only one grain wide, rim between Mgs and fine-grained Soln are barely developed (**Figure 4.3 g-h**). Mg-Cal grains next to Dol reaction rim are slightly coarser compared to the grain size of Soln. Similar to the reaction products between polycrystalline starting materials, Dol formed at pores within the Mg-Cal layer. Using coarse-grained Carrara marble instead of fine-grained Soln as starting a material produced straighter or only slightly curved Dol grain boundaries as observed between two single crystals. The

average grain size of Dol grains is ≈5-6 µm and of Mg-Cal ≈20-25 µm, independent of the starting material, except between Mgs and Carrara where Dol grain size is distinctly smaller (**Table 4.2**).

4.4.2.2 Deformation microstructures

The microstructures of reaction products deformed in triaxial compression and test that were subsequently annealed are similar to those developed in static annealing experiments.

In torsion experiments, strain partioning into the Dol reaction rim is apparent from the microstructure. Dol grains next to magnesite between two polycrystalline reactants are slightly elongated**,** whereas calcite-grown Dol grains are more equiaxed or partially flattened parallel to the shear plane. Grain boundaries are more often curved or irregular compared to the grains in contact with magnesite. Similar to annealing experiments, Dol formed around pores within the Mg-Cal layer. Interestingly, Dol also decorates grain boundaries in Soln up to a distance of at least 100 µm from the reaction interface between the limestone and Mg-Cal (**Figure 4.4**). Inspection of tangential thin sections reveals a tilting of the long axis direction of elongated Dol grains towards the direction of shear.

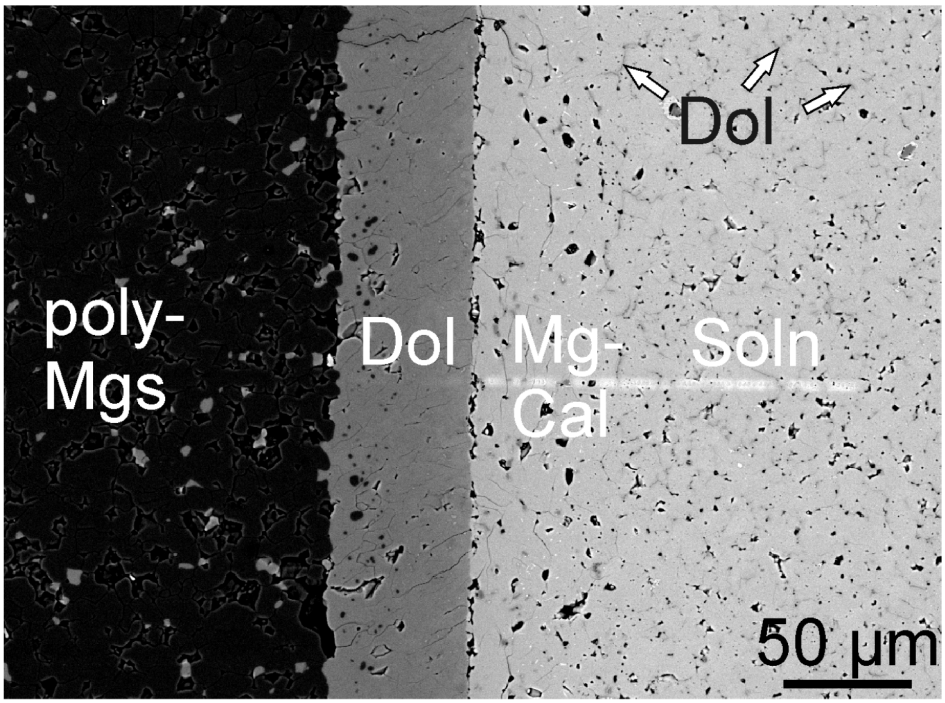

Figure 4.4 Backscatter electron image of reaction products between polycrystalline startingmaterials in twisted sample pCa_pMg-01. Grain boundaries of Soln are decorated by dolomite as indicated by the *white arrows*.

Dol grains next to magnesite produced between Cal and poly-Mgs are marginally elongated with straight boundaries in the high strain region, while equiaxed Dol grains have straight or slightly curved boundaries in the center of the Dol rim. Close to the Mg-Cal and Dol phase boundary, grains are tilted towards the direction of shear and grain boundaries are highly irregular.

Twisted samples form a thin Mg-Cal layer between the copper jacket and the calcite reactant phase, in particular along the Cal reactant, revealing a high mobility of Mg in the highly strained portion of samples.

4.4.3 Texture analysis

4.4.3.1 Static annealing (stack-01)

For two single crystals in contact, all reaction products show at least an axiotactic (one crystallographic axis parallel) relation with respect to the Cal, similar to textures observed in previous annealing experiments on similar starting materials (HELPA ET AL. 2014).

The Dol reaction rim between poly-Mgs in contact with a Cal shows considerably different results. While Mg-Cal grains still show a weak crystallographic orientation relation with respect to the original Cal, the crystallographic orientations of Dol are independent of the starting materials. Poles figures show that the entire Dol is characterized by $[0001]$ axes forming girdles lying within the reaction interface and poles of $\{2\bar{1}\bar{1}0\}$ and $\{10\bar{1}0\}$ prismatic planes arranged (sub-) parallel to the growing direction (GD). $\{10\bar{1}4\}$ poles are blurred and distributed all over the pole figures. The strength of the CPO is slightly stronger for elongated Dol grains in contact with magnesite compared to calcite-grown grains.

CPO of Dol produced in between poly-Mgs and Soln are very similar to CPOs of reaction products in between poly-Mgs and Cal. In this case, Soln reactant has a very similar CPO caused by initial starting orientation. Mg-Cal grains show a weak CPO characterized by $[0001]$ axes parallel to GD and poles of $\{2\bar{1}\bar{1}0\}$ and $\{10\bar{1}0\}$ prismatic planes forming broad diffuse girdles parallel to the reaction interface. Poles of the $\{10\bar{1}4\}$ rhomb planes are randomly distributed.

4.4.3.2 Torsion test (pCa_pMg-01)

In the high strain outer part of the assembly ($\gamma \approx 2$), both polycrystalline reactants exhibit a distinct CPO (**Figure 4.5**). The Soln CPO is characterized by **c**-axes forming a girdle subparallel to the reaction interface and poles of $\{2\bar{1}\bar{1}0\}$ and $\{10\bar{1}0\}$ prismatic planes oriented subparallel to GD, which is also the rotation axis respectively (**Figure 4.5 c**). The poly-Mgs is characterized by $[0001]$ axes distributed along a girdle oblique to the interface reaction, whereas the poles of $\{2\bar{1}\bar{1}0\}$ and $\{10\bar{1}0\}$ prismatic planes have maxima in intermediate positions not related to the external reference frame. The two Dol domains show different microstructures, but similar textures, independent of the starting materials (**Figure 4.5 c**). In both cases, the [0001] axes form girdles oblique at around 45° in relation to the reaction interface, with maxima concentration lying in intermediate positions between the GD and the center of the net. The pole of the prismatic planes form tilted girdles with respect to the reaction interface (shear plane), but in opposite direction. The Mg-Cal layer shows a CPO with the maxima of [0001] parallel to the shear direction and other secondary maxima spread all over the pole figures, with poles of prismatic and rhomb planes forming clusters lying in intermediate positions of the stereoplot.

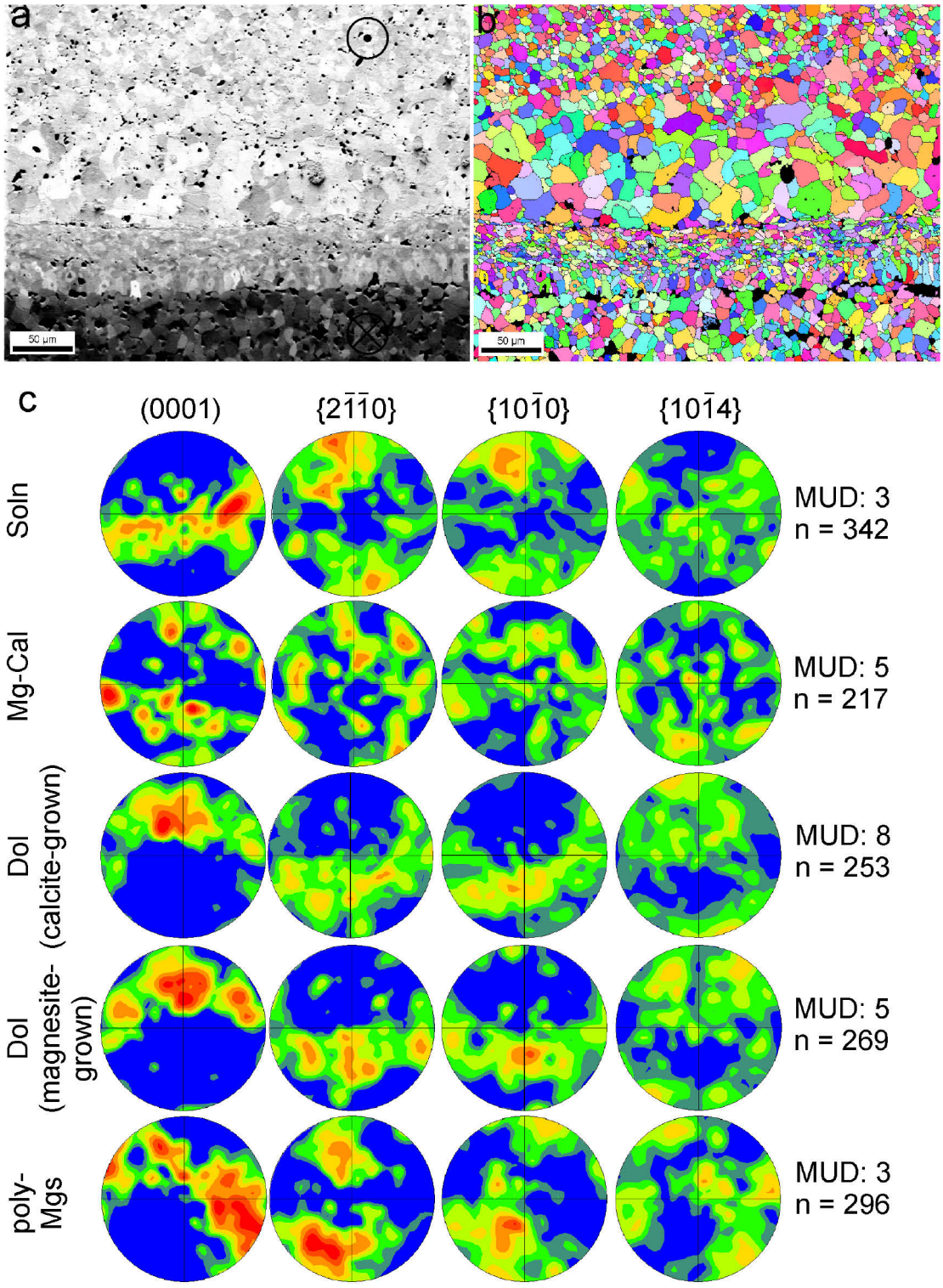

Figure 4.5 Crystallographic preferred orientaions of polycrystalline limestone (Soln), polycrystalline magnesite (poly-Mgs) and reaction products (Mg-Cal, calcite-grown Dol, magnesite-grown Dol) of twisted sample pCa_pMg-02. (**a**) Forward scatter electron image and (**b**) EBSD inverse pole figure (IPF) color-coded map of the investigated area. The section was mapped at the edge of an axial cut section ($\tau \approx 3.8$ MPa, $\gamma \approx 2$). The direction of shear is perpendicular to the image (*arrows*). (**c**) Corresponding pole figures of [0001] axes and poles of prismatic planes {2$\bar{1}\bar{1}$0}/{10$\bar{1}$0} are equal-area lower hemisphere projections with a Gaussian half-width of 10° and a confidence index (CI) of >0.2. Multiple uniform distribution (*MUD*) maxima and number of indexed grains (n) are given next to each contour line plot.

4.4.4 Microprobe analysis

Chemical profiles across the reaction products after static annealing and high strain torsion are shown in **Figure 4.6** and **Figure 4.7**, respectively. Single crystal reactants reveal a homogenous composition indicated by mole fractions $X_i = 1$ for X_{CaO} in Cal and X_{MgO} in Mgs (HELPA ET AL. 2014). Spikes in the chemical profiles of polycrystalline starting materials correspond to impurities and pores (**Figure 4.6 b**). Generally, a nearly stoichiometric composition is achieved in Dol from the initial contact interface to the magnesite reactant, but local deviations are attributed to isolated magnesite inclusions within poly-Mgs reactants (**Figure 4.6; Figure 4.7**). In contrast, calcite-grown Dol reveals an excess of CaO component, continuously increasing towards the Mg-Cal boundary. For the Mg-Cal layer, a successive decrease is observed in Mg component from the Dol boundary towards pure calcite. Using a calcite single crystal, the decreasing Mg content correlates with an increase in grain size. Small peaks in the chemical profiles are caused by pores at grain boundaries accompanied with some Dol formation, if Soln or Carrara marble is used as starting material.

In the central, low strain ($\gamma \approx 0.1$) part of the twisted sample stack Ca_pMg-02, the element distributions of CaO and MgO is comparable to the annealed sample (**Figure 4.7 a**). In contrast, at intermediate ($\gamma \approx 1.9$) and high ($\gamma \approx 3.4$) strain conditions, stagnant mole fraction values are observed on both sides next the Dol|Mg-Cal boundary (**Figure 4.7 b-c**), probably induced by high phase boundary mobility.

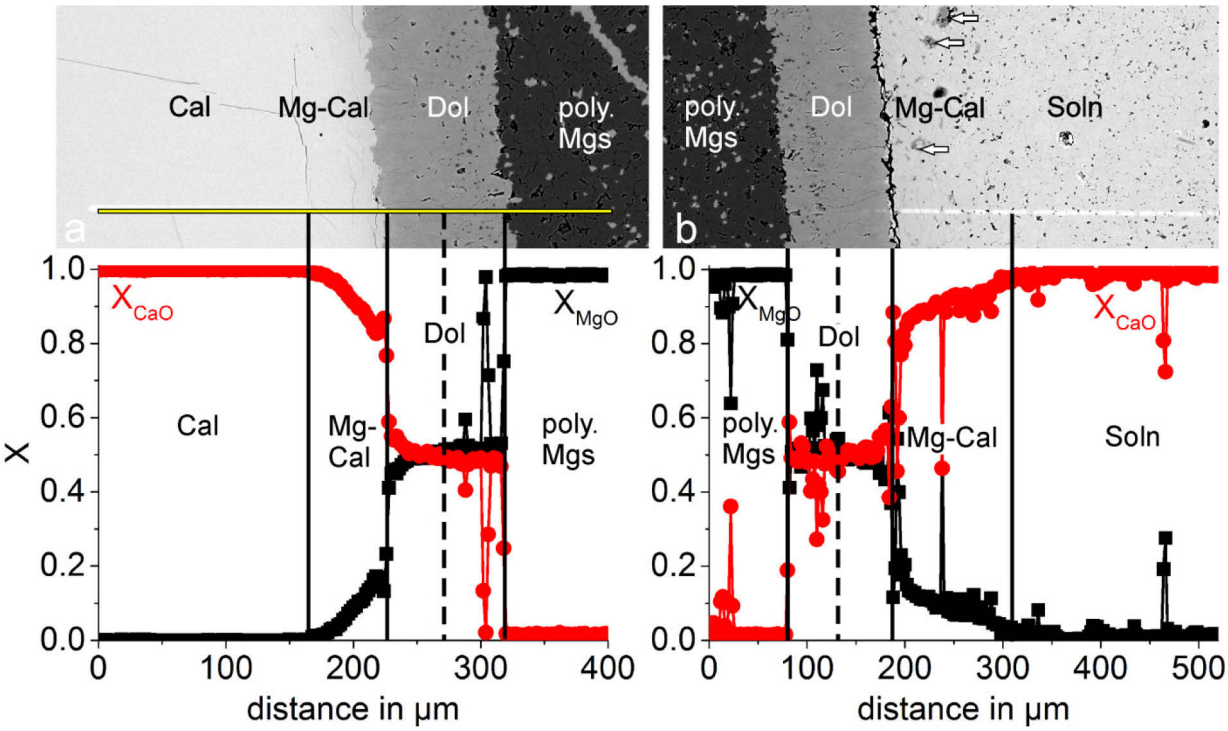

Figure 4.6 Backscatter electron (BSE) images and chemical profiles of reaction products between (**a**) Cal and poly-Mgs and (**b**) poly-Mgs and Soln from experiment stack-01 (t = 29, annealed). Mole fractions of calcium (X_{CaO}) and magnesium (X_{MgO}) across the reaction rim. *Solid vertical lines* represent phase boundaries and *dashed lines* indicate the location of the initial interface between reactants. *White arrows* in (**b**) indicate dolomite formation associated with pores.

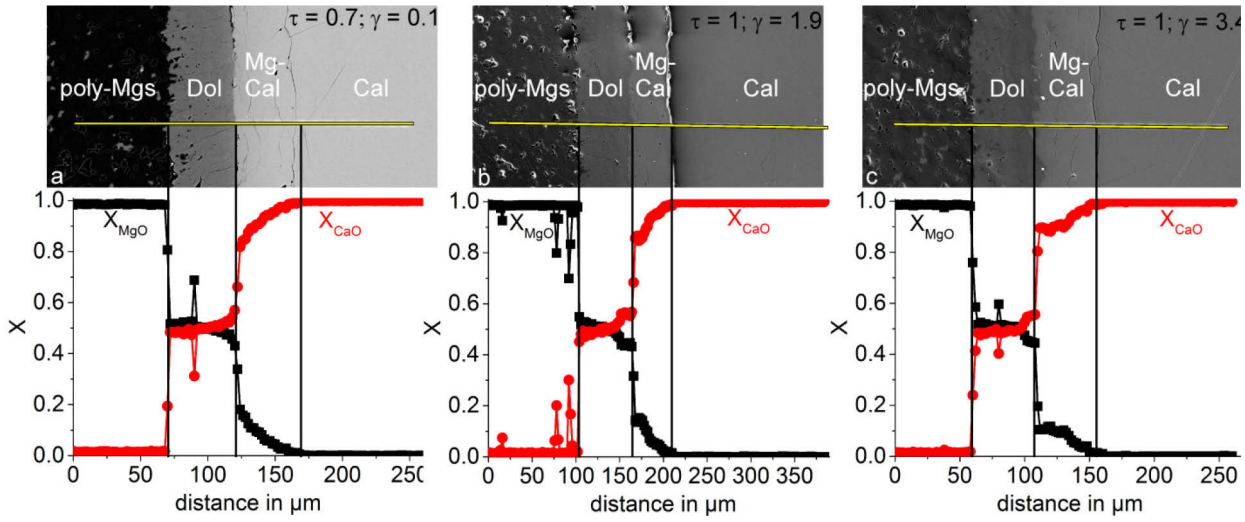

Figure 4.7 BSE images and chemical profiles of torsion experiment Ca_pMg-02, including Cal and poly-Mgs. Plotted are the mole fractions *X* of CaO and MgO component versus the distance. (**a-c**) Line scans were done at different locations within the sample representing a certain shear stress/strain condition. Corresponding shear stresses and strains are given in each micrograph.

4.5 Discussion

4.5.1 Influence of microstructure on reaction progress

Diffusion-controlled solid reaction rim growth is limited by the transport of matter from one reaction front to the other. Two different pathways are available, by volume diffusion through the crystal lattice or by diffusion along grain boundaries. Grain boundary diffusion is usually several orders of magnitudes faster compared to volume diffusion and operates on larger spatial scales (DOHMEN AND MILKE 2010). Depending on grain size, a combination of these two transport processes yields an effective diffusion coefficient, where the diffusion of the slowest species along its fastest path is rate-limiting and controls the overall effective growth rate. For Dol rim growth between calcite and Mgs under hydrostatic conditions, counter-diffusion of CaO and MgO was inferred (HELPA ET AL. 2014). Unfortunately, the determined diffusion coefficients ($D_{CaO,MgO} \approx 10^{-14}$ m/s²) did not allow to discriminate if volume or grain boundary diffusion predominates at these conditions.

In our experiments on two single crystal reactants, the reaction at the Dol-Mgs front seems to be the slowest reaction step for Dol formation as indicated by the chemical profiles. Transport of CaO across the reaction rim forms stoichiometric Dol at this reaction front. In contrast, composition of calcite-grown Dol is not stoichiometric and the formation of Mg-Cal requires further diffusion of the MgO component into the Cal, resulting in a longer diffusion path. The difference is likely to be caused by the relatively large ionic radius of Ca (0.99 Å) compared to the relatively small Mg ion radius of 0.66 Å and similar lattice parameters of Cal and Mgs (ALTHOFF 1977).

Our results demonstrate that the grain size of the magnesite starting material has an important influence on the Dol reaction rim formation. Annealing experiments revealed that the Dol layer is considerably thicker if fine-grained poly-Mgs is used instead of single crystals (**Figure 4.1**). In addition, Dol grown into poly-Mgs contains isolated inclusions of magnesite within individual grains, which appear to be smaller next to the initial interface than at the Dol-magnesite reaction interface (**Figure 4.4; Figure 4.6; Figure 4.7**). We interpret the inclusions as residual magnesite that is progressively consumed by Dol with ongoing reaction progress. The left-over inclusions and the thicker Dol rim evolving in poly-Mgs compared to Mgs suggests that the complete Dol transformation is controlled by lattice reorganization, while the reaction front mobility is controlled by the diffusion of CaO along grain boundaries in magnesite.

In line with these interpretations is the observation that the width of the entire Dol rim is hardly affected by the grain size of the calcite starting material (≈7 mm for Cal, 220 µm for Carrara and 6 µm for Soln). In contrast, the thickness of the Mg-Cal layer increases continuously with decreasing grain size of the calcite reactant (**Figure 4.1**), suggesting predominantly grain boundary diffusion of the Mg component into calcite. To maintain charge neutrality, at the same time Ca has to diffuse towards the Dol interface, which is considerably faster along grain boundaries than intracrystaline (FARVER AND YUND 1996). We expect also fast diffusion along interconnected pores, as suggested by the presence of Dol along pores within the Mg-Cal layer in contact to Soln. The pores are preferentially located at triple junctions and grain boundaries (**Figure 4.4; Figure 4.6 b**) and more likely interconnected in the limestone with 4% porosity than in the marble with <0.5% porosity.

4.5.2 Influence of deformation on reaction progress

Reaction progress of dolomite formation and magnesio-calcite layer growth significantly changes during deformation. Using poly-Mgs in contact with Cal yield 15% thinner Dol rims in triaxially compressed samples and 39% thinner rims in twisted samples compared to the annealing experiment. The width of the Mg-Cal layer is not influenced by triaxial compression, but is about 23% larger in torsion experiments.

The effect of deformation is even more pronounced using poly-Mgs and Soln as reactants. Triaxial compression leads to 21% thinner dolomite rims and torsion lowers the Dol rim width by about 45%. For the magnesio-calcite layer, enhanced thicknesses of 50 to 52% were observed for coaxial loading and twisting.

In summary, triaxial deformation slows down the reaction kinetics of Dol formation and accelerates Mg-Cal layer growth rate, in particular for two polycrystalline starting materials. The retardation effect on Dol is even more pronounced in torsion experiments, almost independent of strain, i. e. similar at the center and periphery of the sample. The different responses of the Mg-Cal layer and the Dol reaction rim to deformation may reflect the additional step of lattice structure reorganization required for dolomite formation.

The impact of stress and strain on Dol growth between single crystals was discussed by HELPA ET AL. (2015), showing that stresses up to 38 MPa do not alter the reaction rate of Dol and do not change significantly the thermodynamic driving forces. The authors observed also a slightly enhanced rate of Mg-Cal production at high strains >0.1, which was attributed

to enhanced dislocation activity, providing additional diffusion pathways. In agreement with that, we observed a slight enhancement of Mg-Cal width in our experiments, in particular if fine-grained Soln is used. Deformation may also increase the mobility of grain boundaries and grain boundary diffusion rates leading to Dol formed along grain boundaries in Mg-Cal and Soln in highly strained torsion samples.

	Porosity (%)	Grain size (µm)
Polycrystalline magnesite		
Starting material	6	4 ± 0
29 h annealing	6.8	11 ± 3
18 h triaxial compression	6.8	11 ± 2
18 h torsion	10.8	10 ± 3
Solnhofen limestone		
Starting material	4	6 ± 1
29 h annealing	3.7	9 ± 1
18 h triaxial compression	3.7	9 ± 1
18 h torsion	3.1	9 ± 1

Table 4.3 Porosity and grain sizes for polycrystalline magnesite and Solnhofen limestone at different experimental conditions.

The thinner Dol rim thickness in deformed samples with poly-Mgs starting material is notably related to an increase of magnesite grain size, assuming that CaO diffusion in magnesite is rate-limiting. The measured average grain sizes of the involved polycrystalline phases are given in **Table 4.3**, showing grain growth with almost similar sizes after experiments. Assuming a grain growth law of the form

$$d^n - d_0^n = Kt \qquad \textbf{(4.1)}$$

with d_0 = initial grain size, d = final grain size after time t, K = rate constant and n = 2-3 (OLGAARD AND EVANS 1986; OLGAARD AND EVANS 1988; COVEY-CRUMP 1997), the grain size of magnesite can be back-calculated from 29 to 18 h annealing time, resulting in a size of ≈9.0-9.5 µm. If we further neglect the Mg-Cal formation and assume for simplicity that the effective diffusivity D is inversely proportional to the grain size d and proportional to the square of rim thickness Δx_{Dol} (i.e., $(\Delta x_{Dol})^2 \sim D \sim d^{-1}$, GARDÉS AND HEINRICH 2011), then the predicted reduction in Dol rim thickness between annealed and triaxially deformed samples is about 7-10%, depending on the assumed grain growth exponent n. Within error bars, this agrees with the observed reduction of ≈14%.

Although the difference is small, we observed a slightly more reduced Dol rim width in torsion experiments compared to axially deformed samples, which cannot be explained by

poly-Mgs grain sizes, since it is similar for compressed and twisted samples (**Table 4.3**). Instead, it may be explained instead by a deformation-induced shape preferred orientation (SPO) or CPO in torsion tests, at least in the highly strained (outer) portion of the sample (**Figure 4.3**), provided that the diffusion properties are anisotropic in the carbonate system. In addition, the associated high strain rate may impede the diffusion rate if the rate-controlling species for deformation is different from that of the reaction (e.g., oxygen vs. calcium diffusion). In this case, the deformation rate may control the Dol production rate. However, we observed a flat reaction rim profile with constant thickness across the inner (low strain) to outer (high strain) portion of samples (**Figure 4.5**), which argues against this explanation.

4.5.3 Influence of water on reaction

In experiment Ca_Mg_Dia-01, dehydration of diaspore increases the water content of the starting materials by about 0.3 wt.%, if all released water is incorporated into the single crystal reactants. Measured average thicknesses of Dol and Mg-Cal layers in this experiment are in good agreement with values measured between single crystals containing about 0.2 wt.% water (HELPA ET AL. 2014; **Figure 4.1; Table 4.2**). Therefore, excess water appears to have no effect on the diffusion-controlled growth kinetics of Dol and Mg-Cal, at least between 0.2 wt.% and ≈0.5 wt.% H_2O. This agrees with deformation experiments on Carrara marble, which are hardly affected the presence of water in the dislocation creep regime (DE BRESSER, URAI, AND OLGAARD 2005). To our knowledge, the influence of water on Ca or Mg self- or grain boundary diffusion in Cal or Dol has not been investigated so far. Self-diffusion experiments of C and O in Cal at T = 650–850 °C under dry conditions showed diffusion coefficients in the same order of magnitude (ANDERSON 1969). In the presence of water, carbon self-diffusion coefficients remained similar, while self-diffusion of oxygen was accelerated about 2 orders of magnitude at 750 °C (KRONENBERG, YUND, AND GILETTI 1984). This indicates that O-diffusion is not rate-limiting in our experiments, since we observed no influence of water (-fugacity) in our rim growth experiments.

In contrast, in the silicate systems MgO-SiO_2 and Mg_2SiO_4-SiO_2 enhanced reaction rim growth kinetics were observed in the presence of water with a factor of 5 to 30 times faster grain boundary diffusion compared to nominally dry conditions (YUND 1997; GARDÉS ET AL. 2012; MILKE ET AL. 2013). Here, only trace amounts of water (tens of ppm) are necessary to enhance the reaction rates (GARDÉS ET AL. 2012; MILKE ET AL. 2013). Thus it seems to be

likely that the silicate system is much more sensitive to the presence of water than the carbonate system.

4.5.4 Aggregate strength, microstructure and CPO development

In this study we observed grain growth in all polycrystalline starting materials and nucleation and growth of reaction products, independent of deformation conditions (**Table 4.2; Table 4.3**). Assuming an exponent of $n = 3$ for the grain growth law (e.g., OLGAARD AND EVANS 1986), the growth rate constant of Soln is in between 5-8·10^{-3} µm³/s and 1-2·10^{-2} µm³/s for poly-Mgs, i.e. faster grain growth rate of poly-Mgs than of Soln (**4.1**). For comparison, DAVIS ET AL. (2011) determined grain growth rates of fine-grained, high purity Ca-Mg carbonates at $T = 800$ °C, $P = 300$ MPa, of $K \approx 5 \cdot 10^{-1}$ µm³/s for calcite, $K \approx 3 \cdot 10^{-4}$ µm³/s for magnesite and $K \approx 5 \cdot 10^{-5}$ µm³/s for Dol. The difference of ≈2 orders of magnitude lower rate for Soln and ≈2 orders of magnitude higher rate for poly-Mgs observed in our experiments is possibly attributed to the difference in temperature, the purity of starting materials and porosity. Assessment of results reported by DAVIS ET AL. (2011), suggests only a minor effect of the temperature difference. However, the porosity was 4% in our samples and 0.04% for samples used by DAVIS ET AL. (2011), and for magnesite 6% (this study) and 28% (DAVIS ET AL. 2011), revealing a strongly reduced growth rate at high porosity.

Mg-Cal layers between Cal and Mgs show an increase in grain size from the Dol boundary towards pure Cal, combined with a successive decrease in Mg-component (e.g., **Figure 4.3 e-f; Figure 4.6 a;** HELPA ET AL. 2014). Reduced grain growth related to Mg-content in poly-Cal was observed by several authors (HERWEGH AND BERGER 2003; XU ET AL. 2009; DAVIS ET AL. 2011). Using Soln, Mg-Cal grains show a more homogenous grain size distribution (**Figure 4.3 b; Figure 4.5 b**), probably related to a high nucleation rate. It is also possible that Mg-Cal grain boundaries are pinned by pores in experiments with Soln, whereas Mg impurities pinned grains in tests with Cal.

Interestingly, the final average grain size of Mg-Cal is ≈18 µm, about 2 times larger compared to polycrystalline calcite with ≈9 µm (**Table 4.2; Table 4.3**), which may be related to pores that hinder grain growth. For example, in sample stack pCa_pMg-01 polycrystalline calcite revealed a porosity of 2.8% with an average pore size of ~1.0 µm. Porosity of the Mg-Cal layer is about 3.1% with an average size of ~1.6 µm, estimated from 2D-section using an open source image analysis program (ImageJ; http://imagej.nih.gov/ij/). Applying models for

grain growth constrained by a second phase, the effect of pore size (d) and volume fraction (f) on the maximum grain size (D_{max}) can be estimated. Using the model of HERWEGH ET AL. (2011):

$$D_{max} = c\left(\frac{d}{f}\right)^{m} \quad \textbf{(4.2)}$$

with m = 0.44 and c being a constant, yields a factor of ~1.06 between grain sizes of Mg-Cal and Soln, which is much smaller than the observed factor of ~2. Applying the model of OLGAARD AND EVANS (1986)

$$D_{max} = c' d^{q} \quad \textbf{(4.3)}$$

for a constant volume fraction of pores of f = 0.03 and c' being a constant, results in 1.5-2.3 times larger grain size of Mg-Cal compared to Soln, depending on the exponent q = 1-2. This is in very good agreement with our measurements.

In the triaxially compressed sample stack Ca_pMg_pCa_Mg-01, both poly-Mgs and Soln deformed, whereas strain is equally distributed. Also, both polycrystalline reactants show grain coarsening from 4 to 11 µm for magnesite grains and 6 to 9 µm for Soln, associated with minor changes of porosities (**Table 4.3**).

For grain sizes between 6–9 µm strain rates in the order of $5.2 \cdot 10^{-4}$ - $1.4 \cdot 10^{-5}$ s^{-1} are predicted for diffusion creep of Soln at our imposed experimental conditions (SCHMID, BOLAND, AND PATERSON 1977), which agrees with the measured strain rate of $\approx 1 \cdot 10^{-4}$ s^{-1} during triaxial deformation. In contrast, predicted strain rates for grain boundary diffusion creep of poly-Mgs with grain sizes of 4 to 11 µm are much slower, ranging between $1.1 \cdot 10^{-6}$ and $5.5 \cdot 10^{-8}$ s^{-1} (HOLYOKE ET AL. 2014). A similar discrepancy is observed for the twisted samples, again predicting much stronger polycrystalline Dol than Soln. This may be related to the chemical composition of the starting materials. HOLYOKE ET AL. (2014) used for their deformation tests natural material, which contained less Ca (4 wt.%) than our samples (8 wt.%).

The CPO development of Dol in between polycrystalline reactants during deformation is independent of the starting materials' CPO, and assumed to be controlled by the kinematic framework (**Figure 4.3 c**). In torsion experiments, **c**-axes of Dol form girdles lying inclined by 45° with respect to the direction of shear (center of the pole figure). This corresponds to the direction of minimum or maximum principle stresses. HELPA ET AL. (2015) reported on a

similar rotation of Dol and Mg-Cal CPO's towards the compression or rotation axes (parallel GD) during triaxial compression and twisting of Cal and Mgs.

4.6 Implications

Our study shows that the Dol and Mg-Cal reaction kinetics in carbonate systems are strongly affected by the grain size of the reactant phases if grain boundary diffusion is rate-controlling. In that case, dolomite formation is enhanced by small grain size of magnesite, whereas Mg-Cal formation is slightly enhanced by the small grain size of calcite. Simultaneous deformation increases the Mg-Cal reaction rate, but reduces the Dol reaction rate.

Magnesite is mainly formed as an alteration product of magnesium-rich metamorphic and igneous rocks, e.g. carbonation of serpentine, but is also found in carbonate hosted sedimentary basins on continental platforms (DEER, HOWIE, AND ZUSSMAN 1992; SIMANDL AND SCHULTES 2004). Calcite and dolomite are occurring very frequently in the Earth crust, especially in sedimentary rocks. Dol is seldom formed by initial nucleation, but rather developed by the replacement of biogenic and abiogenic calcite and aragonite (calcite paramorphism) reacting with magnesium-rich fluids (DEER, HOWIE, AND ZUSSMAN 1992; JONAS, MÜLLER, DOHMEN, BAUMGARTNER, ET AL. 2015; JONAS, MÜLLER, DOHMEN, IMMENHAUSER, ET AL. 2015). Moreover, carbonates are often undergoing deformation in various forms like diagenetic compaction, shearing in fault zones or deformation at collisional plate boundaries (e.g., NEWMAN AND MITRA 1994; BESTMANN, KUNZE, AND MATTHEWS 2000; MOLLI ET AL. 2000 and reference therein), but up to now nothing is reported on the coincident occurrence of all three carbonate types in such tectonic active environments. Indeed, evidence exists that carbonates also enter subduction zones up to 150-280 km in depth (ISHIKAWA ET AL. 2000; ZHANG ET AL. 2003), where a reaction of calcium carbonates with magnesian silicates is expected to produce magnesian carbonates and magnesite (SETO ET AL. 2008). The occurrence of phase transformation in these materials may alter their rheological behavior considerably.

HOLYOKE ET AL. (2014) proposed that magnesite is stronger than dolomite and pure calcite at all geological conditions, expect when differential stress are less than <10 MPa promoting diffusion creep. In addition, XU ET AL. (2009) showed that diffusion creep of calcite is independent of the magnesium content, while in the dislocation creep regime an increased strength of calcite with increasing magnesium is reported. Certainly, the authors showed a reduced grain growth of calcite grains with increasing Mg-content influencing dif-

fusion creep indirectly by keeping grain sizes small.

Consequently, our results might be important in environments of low stresses and high strains, where grain sizes of calcite and magnesite are relatively small allowing diffusion creep and fast mass transport. If such low stresses prevail and grain sizes are small we would expect a relatively fast growth of Mg-Cal and Dol, possibly accommodating most deformation. Indeed, deformation partioning within the Mg-Cal precursor strongly depends on the grain size. Pores and/or second-phase particles may hinder grain growth and therefore prohibit a switch in deformation mechanism to dislocation creep. In shear zones associated with high strains but low stress, the formation of Dol and Mg-Cal may facilitate strain localization in these reaction zones.

4.7 Acknowledgements

We are grateful to P. Jeřábek and J. Till for discussions, S. Gehrmann for sample preparation, M. Naumann for technical support with the Paterson apparatus, H.-P. Nabein for XRD analyzes and D. Rhede for help with the microprobe. This work was funded by the Deutsche Forschungsgemeinschaft within the framework of FOR 741, project RY 103/1-1, which is gratefully acknowledged.

5 General conclusion

This thesis addresses the experimentally studied mineral reaction between calcite and magnesite under isostatic and non-isostatic stress-strain conditions. The main goal was to gain information about the interplay between deformation and the ongoing mineral reaction. Additionally, the influence of water on the reaction kinetics was evaluated. Experimental conditions included isostatic annealing, triaxial compression and torsion conditions. In every experiment the reaction between calcite and magnesite formed a coarse-grained magnesio-calcite precursor layer and a fine-grained dolomite reaction rim. Reaction product widths increased with temperature, run duration and smaller grain size of reactants. All investigations of experiments contain detailed microstructural, chemical and textural analyses allowing a comparison of reaction product formation at different conditions.

Dolomite and magnesio-calcite reaction kinetics were strongly affected by the grain size of reactants. If grain sizes were small, grain boundary diffusion was efficient forming larger dolomite rims and magnesio-calcite layers, whereby CaO diffusion along grain boundaries in magnesite was rate-limiting. Simultaneous deformation increased the magnesio-calcite growth rate, while the dolomite reaction remained unaffected or slowed down. In high strain torsion experiments grain boundary diffusion in the polycrystalline calcite was promoted, supporting magnesio-calcite production. In contrast, retarded dolomite formation was evoked by grain coarsening of magnesite slowing down mass transport along grain boundaries. The experiments directly reflect the grain size sensitivity of the dolomite reaction on the reactant grain size.

Microstructures of the reaction products mainly depend on the microfabric of reactant phases. In all experiments dolomite reaction rims were composed of two distinct microstructural domains. The microstructural boundary between these domains directly reflected the initial contact interface of the reactant phases. Dolomite growing from the initial contact into magnesite always formed palisade-shaped grains. Calcite-grown dolomite was either composed of equiaxed grains in tests with a calcite single crystal or elongated dolomite grains if the reactant was polycrystalline. Also, the magnesio-calcite microstructure was controlled by the microfabric of the calcite reactant. Magnesio-calcite grains growing into a calcite single crystal showed an increase in grain size from the dolomite boundary towards the pure calcite going along with a decrease in Mg content. If the calcite reactant was polycrystalline, grain sizes of the magnesio-calcite were evenly distributed. In the presence of excess water micro-

structures of the reaction products were quite similar, but grain boundaries were more irregular. Triaxial deformation did not affect the microstructure of reaction products noticeably, while grain flattening in the calcite-grown dolomite layer indicated strain partioning in torsion tests.

Chemical compositions of reaction products yielded the same trend in isostatic annealed and deformed samples independent of stress and strain. In all experiments, palisade-shaped dolomite grains revealed a stoichiometric chemical composition with minor amounts of dislocations. Chemical gradients within the granular dolomite domain were associated with higher dislocation densities, which likely helped to accommodate lattice distortion. The main difference between isostatic annealed and deformed samples with respect to the chemical composition was the increased amount of Mg component incorporated into the magnesio-calcite in contact to dolomite. This was observed for samples deformed in axial compression but in particular during shearing. Moreover, abundant dislocations at grain boundaries were observed in the granular dolomite and magnesio-calcite grains in triaxial compression and high strain torsion. At high strains we observed the activation of additional slip systems in the calcite single crystal. This suggests that elevated dislocation mobility enhances growth rates of the magnesio-calcite by providing fast diffusion pathways.

For calcite single crystal reactants, crystallographic orientations of all reaction products were controlled by the initial crystallographic orientation. The relationship was most pronounced in experiments using calcite and magnesite single crystals, where all reaction products at least showed an axiotactic or even a topotactic relation with respect to the calcite reactant. The relationship weakened if a polycrystalline magnesite was used and was totally lost if both reactants were polycrystalline. Texture development of reaction products during deformation was characterized by a reorientation of the crystallographic axes with respect to the external framework. The textural change did not affect the growth behavior of the reaction products.

This study shows that dolomite rim growth is mainly affected by the grain size of the reactants but is not significantly enhanced by triaxial deformation, textural changes or by the presence of water, which is in contrast to silicate systems. However, magnesio-calcite growth rates increased for twisted samples if grain boundary diffusion is efficient. Therefore, the results emphasize the fact that laboratory experiments in different systems are essential to quantify the effect of non-isostatic stress and strain conditions on mineral reactions.

6 Outlook

This thesis yields a lot of new insights to the mineral reaction between carbonates under non-isostatic conditions but also points out aspects, which need further investigation.

- What is the contribution of grain boundary and volume diffusion?
- How does the reaction at the reaction fronts occur?
- What is the reason for a gradual decrease in rim/layer width at a critical strain?
- Is there an influence of water on the reaction between polycrystalline materials?

In our experiments, it was not possible to separate the contributions of grain boundary and volume diffusion to the effective diffusion coefficients. Doping experiments would help to get more information about the mass transfer across the reaction products. A second import point to work on is an extended model for the dolomite rim growth. Chemical composition profiles revealed a half open system with further mass transfer of MgO forming magnesio-calcite. In our model we treated the dolomite rim growth as a closed system. To account for the magnesio-calcite layer, we calculated the theoretical dolomite layer width produced by further diffusion across the dolomite rim. A more complex model would be needed to consider for example the chemical gradient within the magnesio-calcite layer.

The exact mechanisms occurring at the reaction fronts remained unknown. In the presence of fluids, several studies reported on dolomite formation via dissolution precipitation of calcite and/or magnesite. Short time experiments with a detailed investigation of the reaction fronts by TEM could be used to address this question.

In torsion experiments on single crystal reactants we observed a gradual decrease in dolomite rim and magnesio-calcite layer thickness above a critical strain (-rate). In the corresponding paper it is assumed that volume diffusion is hindered by the concurrent deformation of minerals at high strain (-rates). Interestingly, no change in rim/layer thickness was observed in torsion experiments using a polycrystalline magnesite in contact with a calcite single crystal or polycrystalline calcite. Therefore a torsion experiment series is proposed using magnesite aggregates of different grain sizes as starting materials at the same torsion conditions. Thus it is possible to check for a correlation between the microfabrics of the magnesite reactants and the dolomite rim formation with strain (-rate).

Here we investigated the effect of water on the reaction kinetics between calcite and

magnesite single crystals, which was not significant. It would also be interesting to examine the influence of water on the dolomite reaction between polycrystalline reactants.

7 References

Abart, R., and E. Petrishcheva. 2011. “Thermodynamic Model for Reaction Rim Growth: Interface Reaction and Diffusion Control.” *American Journal of Science* 311: 517–27. doi:10.2475/06.2011.02.

Abart, R., E. Petrishcheva, F. D. Fischer, and J. Svoboda. 2009. “Thermodynamic Model for Diffusion Controlled Reaction Rim Growth in a Binary System: Application to the Forsterite-Enstatite-Quartz System.” *American Journal of Science* 309 (2): 114–31. doi:10.2475/02.2009.02.

Abart, R., and R. Sperb. 2001. “Metasomatic Coronas around Hornblendite Xenoliths in Granulite Facies Marble, Ivrea Zone, N Italy. II: Oxygen Isotope Patterns.” *Contributions to Mineralogy and Petrology* 141 (4): 494–504. doi:10.1007/s004100100256.

Adams, B. L., S. I. Wright, and K. Kunze. 1993. “Orientation Imaging: The Emergence of a New Microscopy.” *Metallurgical Transactions A* 24A (4): 819–31. doi:10.1007/BF02656503.

Althoff, P. L. 1977. “Structural Refinements of Dolomite and a Magnesian Calcite and Implications for Dolomite Formation in the Marine Environment.” *American Mineralogist* 62: 772–83.

Anderson, T. F. 1969. “Self-Diffusion of Carbon and Oxygen in Calcite by Isotope Exchange with Carbon Dioxide.” *Journal of Geophysical Research* 74 (15): 3918–32. doi:10.1029/JB074i015p03918.

———. 1972. “Self-Diffusion of Carbon and Oxygen in Dolomite.” *Journal of Geophysical Research* 77 (5): 857–61. doi:10.1029/JB077i005p00857.

Ashworth, J. R., and J. J. Birdi. 1990. “Diffusion Modelling of Coronas around Olivine in an Open System.” *Geochimica et Cosmochimica Acta* 54 (9): 2389–2401. doi:10.1016/0016-7037(90)90227-C.

Ashworth, J. R., and V. S. Sheplev. 1997. “Diffusion Modelling of Metamorphic Layered Coronas with Stability Criterion and Consideration of Affinity.” *Science* 61 (17): 3671–89.

Ashworth, J. R., V. S. Sheplev, N. A. Bryxina, V. Y. Kolobov, and V. V. Reverdatto. 1998. “Diffusion-Controlled Corona Reaction and Overstepping of Equilibrium in a Garnet Granulite , Yenisey Ridge , Siberia.” *Journal of Metamorphic Geology* 16: 231–46.

Barber, D. J., and H. R. Wenk. 2001. “Slip and Dislocation Behaviour in Dolomite.” *European Journal of Mineralogy* 13 (2): 221–43. doi:10.1127/0935-1221/01/0013-0221.

Bestmann, M., K. Kunze, and A. Matthews. 2000. “Evolution of a Calcite Marble Shear Zone Complex on Thassos Island , Greece: Microstructural and Textural Fabrics and Their Kinematic Significance.” *Journal of Structural Geology* 22: 1789–1807.

Brady, J. B. 1977. “Metasomatic Zones in Metamorphic Rocks.” *Geochimica et Cosmochimica Acta* 41: 113–25.

———. 1983. “Intergranular Diffusion in Metamorphic Rocks.” *American Journal of Science* 283-A: 181–200.

Brodie, K. H., and E. H. Rutter. 1985. “On the Relationship between Deformation and Metamorphism, with Special Reference to the Behavior of Basic Rocks.” In *Metamorphic Reactions: Kinetics, Textures and Deformations*, edited by A. B. Thompson and D. C. Rubie, 138–79. New York: Springer.

Burlini, L., and D. Bruhn. 2005. “High-Strain Zones: Laboratory Perspectives on Strain Softening during Ductile Deformation.” *Geological Society, London, Special Publications* 245 (1): 1–24. doi:10.1144/GSL.SP.2005.245.01.01.

Butler, T. W. 1969. “On the Determination of Dislocation Densities.” Annapolis, Maryland.

Covey-Crump, S. J. 1997. “The Normal Grain Growth Behaviour of Nominally Pure Calcitic Aggregates.” *Contributions to Mineralogy and Petrology* 129: 239–54.

Davis, N. E., A. K. Kronenberg, and J. Newman. 2008. “Plasticity and Diffusion Creep of Dolomite.” *Tectonophysics* 456 (August): 127–46. doi:10.1016/j.tecto.2008.02.002.

Davis, N. E., J. Newman, P. B. Wheelock, and A. K. Kronenberg. 2011. “Grain Growth Kinetics of Dolomite, Magnesite and Calcite: A Comparative Study.” *Physics and Chemistry of Minerals* 38 (August): 123–38.

doi:10.1007/s00269-010-0389-9.

de Bresser, J. H. P. 1991. *Intracrystalline Deformation of Calcite*. 79th ed. Utrecht: Geologica Ultraiectina.

de Bresser, J. H. P., J. L. Urai, and D. L. Olgaard. 2005. "Effect of Water on the Strength and Microstructure of Carrara Marble Axially Compressed at High Temperature." *Journal of Structural Geology* 27 (2): 265–81. doi:10.1016/j.jsg.2004.10.002.

de Ronde, A. A., R. Heilbronner, H. Stünitz, and J. Tullis. 2004. "Spatial Correlation of Deformation and Mineral Reaction in Experimentally Deformed Plagioclase–olivine Aggregates." *Tectonophysics* 389 (1-2): 93–109. doi:10.1016/j.tecto.2004.07.054.

de Ronde, A. A., and H Stünitz. 2007. "Deformation-Enhanced Reaction in Experimentally Deformed Plagioclase-Olivine Aggregates." *Contributions to Mineralogy and Petrology* 153 (6): 699–717. doi:10.1007/s00410-006-0171-7.

de Ronde, A. A., H. Stünitz, J. Tullis, and R. Heilbronner. 2005. "Reaction-Induced Weakening of Plagioclase–olivine Composites." *Tectonophysics* 409 (November): 85–106. doi:10.1016/j.tecto.2005.08.008.

Deer, W. A., R. A. Howie, and J. Zussman. 1992. *An Introduction to Rock-Forming Mineral*. 2ND ed. Essex: Addison Wesley Longman Limited.

Delle Piane, C., L. Burlini, and B. Grobety. 2007. "Reaction-Induced Strain Localization: Torsion Experiments on Dolomite." *Earth and Planetary Science Letters* 256 (1-2): 36–46. doi:10.1016/j.epsl.2007.01.012.

Delle Piane, C., L. Burlini, and K. Kunze. 2009. "The Influence of Dolomite on the Plastic Flow of Calcite." *Tectonophysics* 467 (March): 145–66. doi:10.1016/j.tecto.2008.12.022.

Delle Piane, C., L. Burlini, K. Kunze, P. Brack, and J. P. Burg. 2008. "Rheology of Dolomite: Large Strain Torsion Experiments and Natural Examples." *Journal of Structural Geology* 30: 767–76. doi:10.1016/j.jsg.2008.02.018.

Dimanov, A., and G. Dresen. 2005. "Rheology of Synthetic Anorthite-Diopside Aggregates: Implications for Ductile Shear Zones." *Journal of Geophysical Research* 110 (B7): B07203. doi:10.1029/2004JB003431.

Dohmen, R., and R. Milke. 2010. "Diffusion in Polycrystalline Materials: Grain Boundaries, Mathematical Models, and Experimental Data." *Reviews in Mineralogy and Geochemistry* 72 (21): 921–70. doi:10.2138/rmg.2010.72.21.

Etschmann, B., J. Brugger, M. A. Pearce, C. Ta, D. Brautigan, M. Jung, and A. Pring. 2014. "Grain Boundaries as Microreactors during Reactive Fluid Flow: Experimental Dolomitization of a Calcite Marble." *Contributions to Mineralogy and Petrology* 168 (2): 12. doi:10.1007/s00410-014-1045-z.

Evans, B., R. S. Hay, and N. Shimizu. 1986. "Diffusion-Induced Grain-Boundary Migration in Calcite." *Geology* 14 (1): 60–63.

Farver, J. R., and R. A. Yund. 1996. "Volume and Grain Boundary Diffusion of Calcium in Natural and Hot-Pressed Calcite Aggregates." *Contributions to Mineralogy and Petrology* 123: 77–91.

Ferry, J. M. 1983. "Regional Metamorphism of the Vassalboro Formation, South-Central Maine, USA: A Case Study of Th Role of Fluid in Metamorphic Petrogenesis." *Journal of Geological Society, London* 140: 551–76.

Fisher, G. W. 1973. "Nonequilibrium Thermodynamics as a Model for Diffsuion-Controlled Metamorphic Processes." *American Journal of Science* 273: 987–924.

———. 1978. "Rate Laws in Metamorphism." *Geochimica et Cosmochimica Acta* 42: 1035–50.

Fisler, D. K., and R. T. Cygan. 1999. "Diffusion of Ca and Mg in Calcite." *American Mineralogist* 84: 1392–99.

Fisler, D. K., and S. J. Mackwell. 1994. "Kinetics of Diffusion-Controlled Growth of Fayalite." *Physics and Chemistry of Minerals* 21 (July): 156–65. doi:10.1007/BF00203146.

Fitz Gerald, J. D., and H. Stünitz. 1993. "Deformation of Granitoids at Low Metamorphic Grade. I: Reactions and Grain Size Reduction." *Tectonophysics* 221: 269–97. doi:10.1016/0040-1951(93)90164-F.

Fletcher, R. C., and A. W. Hofmann. 1973. "Simple Models of Diffusion and Combined Diffusion-Infiltration Metasomatism." In *Geochemical Transport and Kinetics*, edited by A. W. Hofmann, B. J. Giletti, H. S.

Yoder Jr., and R.A. Yund, 243–59. Carnegie Institution of Washington.

Furusho, M., and K. Kanagawa. 1999. "Transformation-Induced Strain Localization in a Lherzolite Mylonite from the Hidaka Metamorphic Belt of Central Hokkaido, Japan." *Tectonophysics* 313 (4): 411–32. doi:10.1016/S0040-1951(99)00215-2.

Gardés, E., and W. Heinrich. 2011. "Growth of Multilayered Polycrystalline Reaction Rims in the MgO–SiO_2 System, Part II: Modelling." *Contributions to Mineralogy and Petrology* 162 (October): 37–49. doi:10.1007/s00410-010-0581-4.

Gardés, E., B. Wunder, K. Marquardt, and W. Heinrich. 2012. "The Effect of Water on Intergranular Mass Transport: New Insights from Diffusion-Controlled Reaction Rims in the MgO–SiO_2 System." *Contributions to Mineralogy and Petrology* 164 (1): 1–16. doi:10.1007/s00410-012-0721-0.

Gardés, E., B. Wunder, R. Wirth, and W. Heinrich. 2011. "Growth of Multilayered Polycrystalline Reaction Rims in the MgO–SiO2 System, Part I: Experiments." *Contributions to Mineralogy and Petrology* 161 (April): 1–12. doi:10.1007/s00410-010-0517-z.

Gebrande, H. 1982. "Elastic Wave Velocities and Constants of Elasticity of Rocks at Room Temperature and Pressures up to 1 GPa." In *Landolt-Börnstein: Numerical Data and Functional Relationships in Science and Technology*, edited by G. Angenheister, New Series, 238. Berlin, Heidelberg: Springer Berlin Heidelberg.

Gifkins, R. C. 1976. "Grain-Boundary Sliding and Its Accommodation During Creep and Superplasticity." *Metallurgical Transactions A* 7A (August): 1225–32.

Goldsmith, J. R., and H. Heard. 1961. "Subsolidus Phase Relations in the System $CaCO_3$-$MgCO_3$." *Journal of Geology* 69: 45–74.

Goncalves, P., E. Oliot, D. Marquer, and J. A. D. Connolly. 2012. "Role of Chemical Processes on Shear Zone Formation: An Example from the Grimsel Metagranodiorite (Aar Massif, Central Alps)." *Journal of Metamorphic Geology* 30 (7): 703–22. doi:10.1111/j.1525-1314.2012.00991.x.

Gottschalk, M., and P. Metz. 1992. "The System Calcite-Dolomite: A Model to Calculate the Gibbs Free Energy of Mixing on the Basis of Existing Experimental Data." *Neues Jahrbuch Der Mineralogie - Abhandlungen* 164 (1): 29–55.

Götze, L. C. 2015. "Growth of Magnesio-Aluminate Spinel in Thin Film Geometry: In-Situ Monitoring Using Synchrotron X-Ray Diffraction." Freie Universität Berlin.

Götze, L. C., R. Abart, E. Rybacki, L. M. Keller, E. Petrishcheva, and G. Dresen. 2010. "Reaction Rim Growth in the System MgO-Al_2O_3-SiO_2 under Uniaxial Stress." *Mineralogy and Petrology* 99 (October): 263–77. doi:10.1007/s00710-009-0080-3.

Haas, H. 1972. "Diaspore-Corundum Equilibrium Determined by Epitaxis of Diaspore on Corundum." *American Mineralogist* 57: 1375–85.

Hansen, L. N., M. E. Zimmerman, and D. L. Kohlstedt. 2011. "Grain Boundary Sliding in San Carlos Olivine: Flow Law Parameters and Crystallographic-Preferred Orientation." *Journal of Geophysical Research* 116 (B8): B08201. doi:10.1029/2011JB008220.

Heidelbach, F., M. P. Terry, M. Bystricky, C. Holzapfel, and C. McCammon. 2009. "A Simultaneous Deformation and Diffusion Experiment: Quantifying the Role of Deformation in Enhancing Metamorphic Reactions." *Earth and Planetary Science Letters* 278 (3-4): 386–94. doi:10.1016/j.epsl.2008.12.026.

Helpa, V., E. Rybacki, R. Abart, L. F. G. Morales, D. Rhede, P. Jeřábek, and G. Dresen. 2014. "Reaction Kinetics of Dolomite Rim Growth." *Contributions to Mineralogy and Petrology* 167 (4): 1001. doi:10.1007/s00410-014-1001-y.

Helpa, V., E. Rybacki, L. F. G. Morales, and G. Dresen. 2015. "Influence of Stress and Strain on Dolomite Rim Growth: A Comparative Study." *Contributions to Mineralogy and Petrology* 170 (2): 16. doi:10.1007/s00410-015-1172-1.

Herwegh, M., and A. Berger. 2003. "Differences in Grain Growth of Calcite: A Field-Based Modeling Approach." *Contributions to Mineralogy and Petrology* 145 (5): 600–611. doi:10.1007/s00410-003-0473-y.

Herwegh, M., J. Linckens, A. Ebert, A. Berger, and S. H. Brodhag. 2011. "The Role of Second Phases for Controlling Microstructural Evolution in Polymineralic Rocks: A Review." *Journal of Structural Geology* 33 (12): 1728–50. doi:10.1016/j.jsg.2011.08.011.

Herwegh, M., X. Xiao, and B. Evans. 2003. "The Effect of Dissolved Magnesium on Diffusion Creep in Calcite." *Earth and Planetary Science Letters* 212 (3-4): 457–70. doi:10.1016/S0012-821X(03)00284-X.

Hier-Majumder, S., S. Mei, and D. L. Kohlstedt. 2005. "Water Weakening of Clinopyroxenite in Diffusion Creep." *Journal of Geophysical Research* 110 (B7): B07406. doi:10.1029/2004JB003414.

Higgs, D. V., and J. Handin. 1959. "Experimental Deformation of Dolomite Single Crystals." *Bulletin of the Geological Society of America* 70: 245–78.

Hirth, G., and D. L. Kohlstedt. 2003. "Rheology of the Upper Mantle and the Mantle Wedge: A View from the Experimentalists." In *Inside the Subduction Factory*, edited by J. Eiler, Geophysica, 83–105. Washington, D. C. doi:10.1029/138GM06.

Hirth, G., C. Teyssier, and J. Dunlap. 2001. "An Evaluation of Quartzite Flow Laws Based on Comparisons between Experimentally and Naturally Deformed Rocks." *International Journal of Earth Sciences* 90 (1): 77–87. doi:10.1007/s005310000152.

Hobbs, B. E., A. Ord, and K. Regenauer-Lieb. 2011. "The Thermodynamics of Deformed Metamorphic Rocks: A Review." *Journal of Structural Geology* 33 (5): 758–818. doi:10.1016/j.jsg.2011.01.013.

Holland, T. J. B., and R. Powell. 1998. "An Internally Consistent Thermodynamic Data Set for Phases of Petrological Interest." *Journal of Metamorphic Geology* 16: 309–43. doi:10.1111/j.1525-1314.1998.00140.x.

Holyoke, C. W., A. K. Kronenberg, and J. Newman. 2013. "Dislocation Creep of Polycrystalline Dolomite." *Tectonophysics* 590 (April): 72–82. doi:10.1016/j.tecto.2013.01.011.

Holyoke, C. W., A. K. Kronenberg, J. Newman, and C. Ulrich. 2014. "Rheology of Magnesite." *Journal of Geophysical Research Solid Earth* 119: 6534–57. doi:10.1002/2013JB010541.

Holyoke, C. W., and J. Tullis. 2006. "The Interaction between Reaction and Deformation: An Experimental Study Using a Biotite + Plagioclase + Quartz Gneiss." *Journal of Metamorphic Geology* 24 (8): 743–62. doi:10.1111/j.1525-1314.2006.00666.x.

Ishikawa, M., Y. Kaneko, R. Anma, and H. Yamamoto. 2000. "Thematic Article Subhorizontal Boundary between Ultrahigh-Pressure and Low-Pressure Metamorphic Units in the Sulu–Tjube Area of the Kokchetav Massif , Kazakhstan." *The Island Arc* 9: 317–27.

Ji, S., E. Rybacki, R. Wirth, Z. Jiang, and B. Xia. 2005. "Mechanical and Microstructural Characterization of Calcium Aluminosilicate (CAS) and SiO2/CAS Composites Deformed at High Temperature and High Pressure." *Journal of the European Ceramic Society* 25: 301–11. doi:10.1016/j.jeurceramsoc.2004.02.018.

Ji, S., R. Wirth, E. Rybacki, and Z. Jiang. 2000. "High-Temperature Plastic Deformation of Quartz-Plagioclase Multilayers by Layer-Normal Compression." *Journal of Geophysical Research* 105 (B7): 16651. doi:10.1029/2000JB900130.

Joachim, B., E. Garde, R. Abart, and W. Heinrich. 2010. "Experimental Growth of Akermanite Reaction Rims between Wollastonite and Monticellite : Evidence for Volume Diffusion Control." *Contributions to Mineralogy and Petrology* 161: 389–99. doi:10.1007/s00410-010-0538-7.

Joachim, B., E. Gardes, W. Heinrich, and R. Abart. 2009. "Diffusion-Controlled Growth of Bimineralic Merwinite - Diopside Reaction Rims between Wollastonite - Monticellite Interfaces." *Assembly* 11: 8346.

Joesten, R. 1977. "Evolution of Mineral Assemblage Zoning in Diffusion Metasomatism." *Geochimica et Cosmochimica Acta* 41: 649–70.

Jonas, L., T. Müller, R. Dohmen, L. Baumgartner, and B. Putlitz. 2015. "Transport-Controlled Hydrothermal Replacement of Calcite by Mg-Carbonates." *Geology* 43 (9): 779–82. doi:10.1130/G36934.1.

Jonas, L., T. Müller, R. Dohmen, A. Immenhauser, and B. Putlitz. 2015. "Hydrothermal Replacement of Biogenic and Abiogenic Aragonite by Mg-Carbonates: Relation between Textural Control on Effective Element Fluxus and Resulting Carbonate Phase." *Geochimica et Cosmochimica Acta*, submitted.

Karato, S. I., and H. Jung. 2003. “Effects of Pressure on High-Temperature Dislocation Creep in Olivine.” *Philosophical Magazine* 83 (3): 401–14. doi:10.1080/0141861021000025829.

Keller, L. M., R. Abart, H. Stünitz, and C. De Capitani. 2004. “Deformation, Mass Transfer and Mineral Reactions in an Eclogite Facies Shear Zone in a Polymetamorphic Metapelite (Monte Rosa Nappe, Western Alps).” *Journal of Metamorphic Geology* 22 (2): 97–118. doi:10.1111/j.1525-1314.2004.00500.x.

Keller, L. M., R. Abart, R. Wirth, D. Schmid, and K. Kunze. 2006. “Enhanced Mass Transfer through Short-Circuit Diffusion: Growth of Garnet Reaction Rims at Eclogite Facies Conditions.” *American Mineralogist* 91 (7): 1024–38. doi:10.2138/am.2006.2068.

Keller, L. M., L. C. Götze, E. Rybacki, G. Dresen, and R. Abart. 2010. “Enhancement of Solid-State Reaction Rates by Non-Hydrostatic Stress Effects on Polycrystalline Diffusion Kinetics.” *American Mineralogist* 95 (September): 1399–1407. doi:10.2138/am.2010.3372.

Keller, L. M., R. Wirth, D. Rhede, K. Kunze, and R. Abart. 2008. “Asymmetrically Zoned Reaction Rims: Assessment of Grain Boundary Diffusivities and Growth Rates Related to Natural Diffusion-Controlled Mineral Reactions.” *Journal of Metamorphic Geology* 26 (January): 99–120. doi:10.1111/j.1525-1314.2007.00747.x.

Keller, L. M., B. Wunder, D. Rhede, and R. Wirth. 2008. “Component Mobility at 900°C and 18 Kbar from Experimentally Grown Coronas in a Natural Gabbro.” *Geochimica et Cosmochimica Acta* 72 (September): 4307–22. doi:10.1016/j.gca.2008.05.054.

Kenkmann, T., and G. Dresen. 2002. “Dislocation Microstructure and Phase Distribution in a Lower Crustal Shear Zone - An Example from the Ivrea-Zone, Italy.” *International Journal of Earth Sciences* 91 (3): 445–58. doi:10.1007/s00531-001-0236-9.

Kent, A. J. R., I. D. Hutcheon, F. J. Ryerson, and D. L. Phinney. 2001. “The Temperature of Formation of Carbonates in Martian Meteorite ALH84001: Constraints from Cation Diffusion.” *Geochimica et Cosmochimica Acta* 65 (2): 311–21. doi:10.1016/S0016-7037(00)00528-7.

Kerrich, R., I. Allison, R. L. Barnett, S. Moss, and J. Starkey. 1980. “Microstructural and Chemical Transformations Accompanying Deformation of Granite in a Shear Zone at Miéville, Switzerland; with Implications for Stress Corrosion Cracking and Superplastic Flow.” *Contributions to Mineralogy and Petrology* 73 (3): 221–42. doi:10.1007/BF00381442.

Kronenberg, A. K., R. A. Yund, and B. J. Giletti. 1984. “Carbon and Oxygen Diffusion in Calcite: Effects of Mn Content and PH2o.” *Physics and Chemistry of Minerals* 11: 101–12.

Kruse, R., and H. Stünitz. 1999. “Deformation Mechanisms and Phase Distribution in Mafic High-Temperature Mylonites from the Jotun Nappe, Southern Norway.” *Tectonophysics* 303 (1-4): 223–49. doi:10.1016/S0040-1951(98)00255-8.

Lasaga, A. C. 1983. “Geospeedometry: An Extension of Geothermometry.” In *Kinetics and Equilibrium in Mineral Reactions*, edited by S. K. Saxena, 81–114. New York: Springer.

Llana-Funez, S., and E. H. Rutter. 2014. “Effect of Strain Geometry on the Petrophysical Properties of Plastically Deformed Aggregates: Experiments on Solnhofen Limestone.” In *Deformation Structures and Processes within the Continental Crust*, edited by S. Llana-Funez, A. Marcos, and F. Bastida, 394:167–87. London: Geological Society, London, Special Publication. doi:10.1144/SP394.12.

Malone, M. J., P. A. Baker, and S. J. Burns. 1996. “Recrystallization of Dolomite : An Experimental Study from 50-200 °C” 60 (12): 2189–2207.

Mei, S., and D. L. Kohlstedt. 2000a. “Influence of Water on Plastic Deformation of Olivine Aggregates 1. Diffusion Creep Regime.” *Journal of Geophysical Research* 105 (B9): 21457–69.

———. 2000b. “Influence of Water on Plastic Deformation of Olivine Aggregates 2. Dislocation Creep Regime.” *Journal of Geophysical Research* 105 (B9): 21471–81.

Milke, R., R. Abart, K. Kunze, M. Koch-Müller, D. Schmid, and P. Ulmer. 2009. “Matrix Rheology Effects on Reaction Rim Growth I: Evidence from Orthopyroxene Rim Growth Experiments.” *Journal of Metamorphic Geology* 27 (1): 71–82. doi:10.1111/j.1525-1314.2008.00804.x.

Milke, R., and W. Heinrich. 2002. “Diffusion-Controlled Growth of Wollastonite Rims between Quartz and

Calcite : Comparison between Nature and Experiment." *Journal of Metamorphic Geology* 20 (5): 467–80.

Milke, R., G. Neusser, K. Kolzer, and B. Wunder. 2013. "Very Little Water Is Necessary to Make a Dry Solid Silicate System Wet." *Geology* 41 (2): 247–50. doi:10.1130/G33674.1.

Milke, R., M. Wiedenbeck, and W. Heinrich. 2001. "Grain Boundary Diffusion of Si, Mg, and O in Enstatite Reaction Rims: A SIMS Study Using Isotopically Doped Reactants." *Contributions to Mineralogy and Petrology* 142 (1): 15–26. doi:10.1007/s004100100277.

Milke, R., and R. Wirth. 2003. "The Formation of Columnar Fiber Texture in Wollastonite Rims by Induced Stress and Implications for Diffusion-Controlled Corona Growth." *Physics and Chemistry of Minerals* 30 (4): 230–42. doi:10.1007/s00269-003-0304-8.

Molli, G., P. Conti, G. Giorgetti, M. Meccheri, and N. Oesterling. 2000. "Microfabric Study on the Deformational and Thermal History of the Alpi Apuane Marbles (Carrara Marbles), Italy." *Journal of Structural Geology* 22 (11-12): 1809–25. doi:10.1016/S0191-8141(00)00086-9.

Mrowec, S. 1980. *Defects and Diffusion in Solids: An Introduction*. Warsaw, Poland: PWN Polish scientific publishers.

Müller, T., D. Cherniak, and E. B. Watson. 2012. "Interdiffusion of Divalent Cations in Carbonates: Experimental Measurements and Implications for Timescales of Equilibration and Retention of Compositional Signatures." *Geochimica et Cosmochimica Acta* 84 (May): 90–103. doi:10.1016/j.gca.2012.01.011.

Newman, J., and M. R. Drury. 2010. "Control of Shear Zone Location and Thickness by Initial Grain Size Variations in Upper Mantle Peridotites." *Journal of Structural Geology* 32 (6): 832–42. doi:10.1016/j.jsg.2010.06.001.

Newman, J., W. M. Lamb, M. R. Drury, and R. L. M. Vissers. 1999. "Deformation Processes in a Peridotite Shear Zone : Reaction-Softening by an H_2O-Deficient ,continuous Net Transfer Reaction." *Tectonophysics* 303: 193–222.

Newman, J., and G. Mitra. 1994. "Fluid-Influenced Deformation and Recrystallization of Dolomite at Low Temperatures along a Natural Fault Zone, Mountain City Window, Tennessee." *Geological Society of America Bulletin* 106 (10): 1267–80.

Olgaard, D. L., and B. Evans. 1986. "Effect of Second-Phase Particles on Grain Growth in Calcite." *Journal of American Ceramic Society* 69 (11): C – 272 – C – 277. doi:10.1111/j.1151-2916.1986.tb07374.x.

———. 1988. "Grain Growth in Synthetic Marbles with Added Mica and Water." *Contributions to Mineralogy and Petrology* 100: 246–60.

Paterson, M. S. 1970. "A High-Pressure, High-Temperature Apparatus for Rock Deformation." *International Journal of Rock Mechanics and Mining Sciences & Geomechanics Abstracts* 7 (5): 517–26. doi:10.1016/0148-9062(70)90004-5.

Paterson, M. S., and D. L. Olgaard. 2000. "Rock Deformation Tests to Large Shear Strains in Torsion." *Journal of Structural Geology* 22 (September): 1341–58. doi:10.1016/S0191-8141(00)00042-0.

Post, A. D., J. Tullis, and R. A. Yund. 1996. "Effects of Chemical Environment on Dislocation Creep of Quartzite." *Journal of Geophysical Research* 101 (B10): 22143. doi:10.1029/96JB01926.

Putnis, A., and J. D. C. McConnoll. 1980. *Priniciples of Mineral Behaviour*. Edited by A. Hallam. Geoscience. New York: Elsevier.

Raj, R., and F. Ashby. 1971. "On Grain Boundary Sliding and Diffusional Creep." *Metallurgical Transactions A* 2 (April): 1113–27.

Rubie, D. C. 1983. "Reaction-Enhanced Ductility: The Role of Solid-Solid Univatiant Reactions in Deformation of the Crust and Mantle." *Tectonophysics* 96: 331–52.

———. 1986. "The Catalysis of Mineral Reactions by Water and Restrictions on the Presence of Aqueous Fluid During Metamorphism." *Mineralogical Magazine* 50 (357): 399–415. doi:10.1180/minmag.1986.050.357.05.

Rutter, E. H., and K. H Brodie. 2004. "Experimental Intracrystalline Plastic Flow in Hot-Pressed Synthetic

Quartzite Prepared from Brazilian Quartz Crystals." *Journal of Structural Geology* 26 (2): 259–70. doi:10.1016/S0191-8141(03)00096-8.

Rutter, E. H., and K. H. Brodie. 1988. "Experimental 'syntectonic' dehydration of Serpentinite under Conditions of Controlled Pore Water Pressure." *Journal of Geophysical Research* 93 (B5): 4907–32.

Rybacki, E., and G. Dresen. 2000. "Dislocation and Diffusion Creep of Synthetic Anorthite Aggregates." *Journal of Geophysical Research* 105 (B11): 26017. doi:10.1029/2000JB900223.

———. 2004. "Deformation Mechanism Maps for Feldspar Rocks." *Tectonophysics* 382 (3-4): 173–87. doi:10.1016/j.tecto.2004.01.006.

Rybacki, E., B. Evans, C. Janssen, R. Wirth, and G. Dresen. 2013. "Influence of Stress, Temperature, and Strain on Calcite Twins Constrained by Deformation Experiments." *Tectonophysics* 601 (August): 20–36. doi:10.1016/j.tecto.2013.04.021.

Rybacki, E., M. Gottschalk, R. Wirth, and G. Dresen. 2006. "Influence of Water Fugacity and Activation Volume on the Flow Properties of Fine-Grained Anorthite Aggregates." *Journal of Geophysical Research* 111 (B03203): 16. doi:10.1029/2005JB003663.

Rybacki, E., R. Wirth, and G. Dresen. 2010. "Superplasticity and Ductile Fracture of Synthetic Feldspar Deformed to Large Strain." *Journal of Geophysical Research: Solid Earth* 115. doi:10.1029/2009JB007203.

Schmalzried, H. 1978. "Reactivity and Point Defects of Double Oxides with Emphasis on Simple Silicates." *Physics and Chemistry of Minerals* 2: 279–94.

Schmid, S. M., J. N. Boland, and M. S. Paterson. 1977. "Superplastic Flow in Finegrained Limestone." *Tectonophysics* 43: 257–91.

Schmid, S. M., M. S. Paterson, and J. N. Boland. 1980. "High Temperature Flow and Dynamic Recrystallization in Carrara Marble." *Tectonophysics* 65: 245–80.

Seto, Y., D. Hamane, T. Nagai, and K. Fujino. 2008. "Fate of Carbonates within Oceanic Plates Subducted to the Lower Mantle, and a Possible Mechanism of Diamond Formation." *Physics and Chemistry of Minerals* 35 (4): 223–29. doi:10.1007/s00269-008-0215-9.

Sieber, H., P. Werner, and D. Hesse. 1997. "The Atomic Structure of the Reaction Front as a Function of the Kinetic Regime of a Spinel-Forming Solid-State Reaction." *Philosophical Magazine A* 75 (4): 909–24. doi:10.1080/01418619708214001.

Simandl, G. J., and H. Schultes. 2004. "Classification of Magnesite Deposits with Emphasis on the Mount Brussilof and Kunwarara Types." In *37th Annual Forum on Industrial Minerals Proceedings, Industrial Minerals with Emphasis on Western North America*, edited by G. J. Simandl, W. J. McMillan, and N. D. Robinson, 83–85. Victoria, Canada: British Columbia, Ministry of Energy and Mines, Geological Survey Branch.

Stünitz, H. 1998. "Syndeformational Recrystallization - Dynamic or Compositionally Induced?" *Contributions to Mineralogy and Petrology* 131 (2-3): 219–36. doi:10.1007/s004100050390.

Terry, M. P., and F. Heidelbach. 2006. "Deformation-Enhanced Metamorphic Reactions and the Rheology of High-Pressure Shear Zones, Western Gneiss Region, Norway." *Journal of Metamorphic Geology* 24 (1): 3–18. doi:10.1111/j.1525-1314.2005.00618.x.

Tsurumi, J., H. Hosonuma, and K. Kanagawa. 2003. "Strain Localization due to a Positive Feedback of Deformation and Myrmekite-Forming Reaction in Granite and Aplite Mylonites along the Hatagawa Shear Zone of NE Japan." *Journal of Structural Geology* 25 (4): 557–74. doi:10.1016/S0191-8141(02)00048-2.

Turner, F. J., D. T. Griggs, and H. Heard. 1954. "Experimental Deformation of Calcite Crystals." *Bulletin of the Geological Society of America* 66: 883–934.

Watson, E. B., and E. F. Baxter. 2007. "Diffusion in Solid-Earth Systems." *Earth and Planetary Science Letters* 253 (3-4): 307–27. doi:10.1016/j.epsl.2006.11.015.

Watson, E. B., and J. D. Price. 2002. "Kinetics of the Reaction Reaction $MgO + Al_2O_3 \rightarrow MgAl_2O_4$ and Al-Mg Interdiffusion in Spinel at 1200 to 2000 °C and 1.0 to 4.0 GPa." *Geochimica et Cosmochimica Acta* 66 (12): 2123–38. doi:10.1016/S0016-7037(02)00827-X.

Wenk, H. R. 1985. “Carbonates.” In *Preferred Orientation in Deformed Metals and Rocks: An Introduction to Modern Texture Analysis*, edited by H. R. Wenk, 361–84. Orlando: Academic Press.

Wenk, H. R., D. J. Barber, and R. J. Reeder. 1983. “Microstuctures in Carbonates.” In *Reviews in Mineralogy*, edited by R J Reeder, 11: Carbon, 301–67. Chelsea: BookCrafters, Inc.

Whitmeyer, S. J., and R. P. Wintsch. 2005. “Reaction Localization and Softening of Texturally Hardened Mylonites in a Reactivated Fault Zone, Central Argentina.” *Journal of Metamorphic Geology* 23 (6): 411–24. doi:10.1111/j.1525-1314.2005.00588.x.

Xu, L., J. Renner, M. Herwegh, and B. Evans. 2009. “The Effect of Dissolved Magnesium on Creep of Calcite II: Transition from Diffusion Creep to Dislocation Creep.” *Contributions to Mineralogy and Petrology* 157 (3): 339–58. doi:10.1007/s00410-008-0338-5.

Yund, R. A. 1997. “Rates of Grain Boundary Diffusion through Enstatite and Forsterite Reaction Rims.” *Contributions to Mineralogy and Petrology* 126 (3): 224–36. doi:10.1007/s004100050246.

Zhang, L., D. J. Ellis, R. J. Arculus, W. Jiang, and C. Wei. 2003. “‘Forbidden Zone’ Subduction of Sediments to 150 km Depth - The Reaction of Dolomite to Magnesite + Aragonite in the UHPM Metapelites from Western Tianshan, China.” *Journal of Metamorphic Geology* 21 (6): 523–29. doi:10.1046/j.1525-1314.2003.00460.x.